

NUMERICAL SIMULATIONS OF GAS DISCHARGES FOR FLOW CONTROL  
APPLICATIONS

A Dissertation

Submitted to the Faculty

of

Purdue University

by

Tugba Piskin

In Partial Fulfillment of the

Requirements for the Degree

of

Doctor of Philosophy

December 2019

Purdue University

West Lafayette, Indiana

**THE PURDUE UNIVERSITY GRADUATE SCHOOL  
STATEMENT OF DISSERTATION APPROVAL**

Dr. Jonathan Poggie, Chair

School of Aeronautics and Astronautics

Dr. Sergey O. Macheret

School of Aeronautics and Astronautics

Dr. Alina Alexeenko

School of Aeronautics and Astronautics

Dr. Alexey Shashurin

School of Aeronautics and Astronautics

**Approved by:**

Dr. Weinong Chen

Head of the School Graduate Program

To Memus,  
To all women breaking boundaries drawn by societies.

## ACKNOWLEDGMENTS

First and foremost acknowledgment goes to my advisor Prof. Jonathan Poggie, for his support and guidance throughout my studies. He taught me to work independently and helped me whenever I need guidance. He has patiently steered my work towards being substantial. I cannot express my gratitude for him because I believe that the things I learned from him will improve my experiences in both academia and industry.

Prof. Sergey Macheret deserves special thanks for spreading his enthusiasm on plasma science and for supporting me from the college application to the end. It was an insightful and challenging experience to work with Prof. Poggie and Macheret together. It was incredibly helpful for me to learn the fundamentals of plasma experiments by attending all experimental courses given by Prof. Alexey Shashurin. I am thankful to him for his guidance and helps throughout my study on the plasma. I also would like to thank my other committee member, Prof. Alina Alexeenko, for her time and comments on my thesis.

I want to thank Purdue University and School of Aeronautics and Astronautics for funding and computational sources. I would like to thank my friends in Prof. Poggie's research group; Sashank Srinivasan, Geoffrey Andrews, Ian Hall, and especially Akshay Deshpande for tolerating my jokes. I am grateful to Vladlen Podolsky for his collaboration on my studies and his friendship. I would like to thank my officemate, Praveen Srikanth, for sharing ideas and discussions about teaching and graduate life. Leela Madhuri and Yuchen Leng deserve special thanks for making Lafayette much more pleasurable. I am indebted to Senem and Urcan Guler for their mentorship and support during my study.

I could not complete my degree without the support and love of my friends from Turkey. I am so glad that I have an amazing friend, Gulay Senol, for the last eleven years. I hope that everyone has a friendship like us where you feel like you are

supported and loved whatever the conditions are. I am indebted to Koray Kaymazlar for being there for me and challenging me. I would like to shout out the residents of room 101 - especially Deniz Secilmis and Nur Yildirim. Although we have not been sharing the same dormitory room anymore, they always stand beside me. I am sincerely thankful to have a friend like Ali Yildirim; he is always open for any kind of discussion, and as always, I learned a lot from him. I am thankful to Ugur Karban, a fantastic friend with continuous support and motivation to make me move forward.

I owe my deepest and warmhearted thanks to my family, who gives me their un-failing support and love. I grew up in a small town in Turkey; it is always challenging for girls to achieve something not accepted by society. I am grateful to my parents; Seher and Durali Piskin for their supports and their fights to open their kids' way to pursue their degrees. Life would not be colorful without my sisters and my brother; Bilge, Kubra, and Faruk Piskin.

## TABLE OF CONTENTS

	Page
LIST OF TABLES . . . . .	viii
LIST OF FIGURES . . . . .	ix
SYMBOLS . . . . .	xiii
ABBREVIATIONS . . . . .	xv
ABSTRACT . . . . .	xvi
1 Introduction . . . . .	1
1.1 Introduction to Gas Discharges . . . . .	3
1.2 Applications in Aerospace Engineering . . . . .	8
1.2.1 Reentry plasma . . . . .	8
1.2.2 Flow control applications . . . . .	9
1.2.3 Computational Flow Control Studies . . . . .	12
1.2.4 Plasma assisted combustion . . . . .	14
1.3 Challenges of Gas Discharge Simulations . . . . .	15
1.4 This Dissertation: Motivation, Objective, Organization . . . . .	19
2 Methods . . . . .	23
2.1 Physical Modeling . . . . .	23
2.1.1 Particle Approach . . . . .	24
2.1.2 Continuum Approach . . . . .	25
2.1.3 Hybrid Approach . . . . .	28
2.2 Numerical Modeling . . . . .	28
2.2.1 Time and Space Resolution Requirements . . . . .	31
2.2.2 Discretization of Equations . . . . .	31
2.2.3 Semi-Implicit Implementation of Poisson Equation . . . . .	33
2.2.4 Electron Energy Equation Discretization . . . . .	34

	Page
2.2.5	Boundary Conditions . . . . . 35
2.2.6	Cubic Spline Method . . . . . 37
2.3	1 D Glow Discharge Calculations . . . . . 38
2.4	Summary . . . . . 44
3	The Local Field Approximation . . . . . 45
3.1	The LFA . . . . . 45
3.2	Calculations with Bolsig+ . . . . . 47
3.3	Zero Dimensional Electron Temperature Solver . . . . . 55
3.4	Summary . . . . . 58
4	Simulations with the LFA and improvements on the LFA . . . . . 59
4.1	Nanosecond Pulsed Discharges . . . . . 59
4.2	Simulations of 1-D NS Pulse Discharges . . . . . 61
4.2.1	Resolution . . . . . 69
4.2.2	Physical Models . . . . . 74
4.2.3	Summary . . . . . 78
5	Simulations with Non- Local Effects . . . . . 79
5.0.1	Electron Energy Relaxation Length . . . . . 79
5.1	Thermal Electron Energy Equation . . . . . 80
5.1.1	Boundary Conditions . . . . . 82
5.2	Results with Electron Thermal Energy Equation Solver . . . . . 85
5.3	Summary . . . . . 90
6	Conclusions . . . . . 92
6.1	Summary and Conclusions . . . . . 92
6.2	Recommendations for Future Work . . . . . 94
	REFERENCES . . . . . 96
A	Coefficients and Constants for the Simulations . . . . . 105
B	Discussion about Reaction Rates . . . . . 106
VITA	. . . . . 110

## LIST OF TABLES

Table	Page
1.1 Time scales in seconds for different mechanisms. . . . .	17
1.2 Classification of simulation cases. . . . .	18
2.1 The summary of different moments of Boltzmann equation used in this study.	27
4.1 Mobility and Diffusion Coefficients . . . . .	64
4.2 Reaction Rates for pure Argon . . . . .	65
4.3 Reaction Rates for Ar- $H_2O$ mixture . . . . .	66
4.4 Classification of simulation cases. . . . .	69
4.5 Varying initial conditions, number densities in $m^{-3}$ . . . . .	72
5.1 Species in the simulations and their heat of formation referenced to the room temperature. . . . .	83
5.2 Heat of reaction for each reactions. . . . .	84
A.1 Townsend, recombination rate, and the secondary emission coefficient for different simulations with specified case numbers. . . . .	105
A.2 Transport —mobility, $\mu$ and diffusion, $D$ — coefficients for ions and elec- trons in different gases for various simulations. ER means Einstein Relation.	105
B.1 Examples of Different Reaction Rates for the Same Processes. . . . .	106

## LIST OF FIGURES

Figure	Page
1.1 Electron temperatures and number densities for various plasma across universe, redrawn from following works: [3,4]. Photographs by the author.	1
1.2 Current- Voltage characteristics of DC discharges, redrawn based on figures in Refs. [5,6] . . . . .	3
1.3 The schematic representation of the multiplications of electrons. . . . .	4
1.4 Column organization in glow discharges and distinct regions [5,6]. . . . .	6
1.5 The schematic representation of the DBD plasma actuator. . . . .	11
1.6 The discharge simulation for $N_2$ at 5 Torr with an external circuit consisting only resistance, $R = 300\text{ k}\Omega$ and $V_e = 1000\text{V}$ . . . . .	16
2.1 Schematic diagram of electric circuit and discharge chamber. . . . .	29
2.2 The comparison of $\Delta\phi$ and $\frac{2k_bT_e}{q}$ from simulations of $H_2$ at 3 Torr pressure with 2 cm gap distance for constant $T_e$ . . . . .	33
2.3 The flow chart of the code. . . . .	35
2.4 Resolution study for $H_2$ at $t = 5 \times 10^{-3}\text{ s}$ , $V = 1\text{ kV}$ , $P = 3\text{ Torr}$ , $\gamma = 0.33$ , $R = 300\text{ k}\Omega$ . . . . .	38
2.5 Comparisons of 1D simulations with Surzhikov and Shang's 2D simulation results [59] for $H_2$ , $R = 300\text{ k}\Omega$ , $P = 3\text{ Torr}$ , $\gamma = 0.33$ , $V = 1\text{ kV}$ . . . . .	39
2.6 Similarity verification (the same voltage fall and the same cathode sheath thickness) with the same $pd$ for $H_2$ , $t = 5 \times 10^{-3}\text{ s}$ , $P = 3\text{ Torr}$ , $\gamma = 0.33$ , $R = 300\text{ k}\Omega$ , $V = 1\text{ kV}$ . . . . .	40
2.7 Glow discharge simulation of various pressure for $H_2$ , $t = 5 \times 10^{-3}\text{ s}$ , $\gamma = 0.33$ , $R = 300\text{ k}\Omega$ , $d = 2\text{ cm}$ , $V = 1\text{ kV}$ . . . . .	41
2.8 Glow discharge simulation of various distance for $H_2$ , $t = 5 \times 10^{-3}\text{ s}$ , $\gamma = 0.33$ , $R = 300\text{ k}\Omega$ , $P = 3\text{ Torr}$ , $V = 1\text{ kV}$ . . . . .	41
2.9 Computed number density, electric field, and potential across the domain for various conditions for $H_2$ , $t = 5 \times 10^{-3}\text{ s}$ , $P = 3\text{ Torr}$ , $\gamma = 0.33$ , $R = 300\text{ k}\Omega$ , $V = 1\text{ kV}$ . . . . .	42

Figure	Page
2.10 Glow discharge simulation results for $H_2$ , $R = 300\text{ k}\Omega$ , $P = 3\text{ Torr}$ , $\gamma = 0.1$ , $V = 1\text{ kV}$ . . . . .	43
3.1 Cross sections for four reactions of argon gas from LxCat website and Trinita database [65]. . . . .	48
3.2 Ratio of electron diffusion coefficients $D_e$ to electron mobility $\mu_e$ vs reduced electric field in Argon from the studies of Wagner et.al. [68],Eletskaa [66], and Kucukarpaci & Lucas [67] with the mean electron temperature values from Bolsig+ [40]. . . . .	49
3.3 Comparison of reaction rates derived from different solutions of Boltzmann equation for electrons. Literature 1 [70] and Literature 2 [72] are compared with BOLSIG+ results [40,65]. . . . .	50
3.4 Comparisons of Maxwellian and non-Maxwellian EEDF on reaction rates calculated by using Bolsig+ and Trinita database [40,65]. . . . .	51
3.5 Comparisons of the effects of Maxwellian and non- Maxwellian distribution of EEDF for pure argon [40,65]. . . . .	52
3.6 Effects of the ionization degree and e-e collisions on the E/N vs $T_e$ for pure argon. Cross-sections are from Trinita database [65]. . . . .	52
3.7 Electron mobility and diffusion coefficients from Bolsig+ [40] and Trinita database [65] for 3 Torr pressure. . . . .	53
3.8 The effects of the water percentage on the $T_e$ variations with respect to the local $E/N$ , calculated from BOLSIG+ [40] by using Trinita database for argon [65], and Itikawa database for water [74]. . . . .	54
3.9 The effects of water amount on the transport properties calculated by using Bolsig+ [40], Trinita database for argon [65], and Itikawa database for water [74]. . . . .	55
3.10 Collision frequencies for different processes of argon and water vapor at 3 Torr. Trinita database [65] is used for cross-sections of each process. . . . .	56
3.11 0-D solver check with BOLSIG+ [40] for E/N vs $T_e$ . . . . .	57
4.1 Various time scales for short nanosecond pulse discharges in argon. . . . .	60
4.2 Measured properties of circuit as a function of time. An experimental uncertainty of one standard deviation (STD) is indicated [83]. . . . .	62
4.3 Measurements of spatially-averaged electron number density $n_e(t)$ . An experimental uncertainty of one standard deviation (STD) is indicated [83].	62
4.4 Comparison of raw and smoothed time trace of input voltage. . . . .	63

Figure	Page	
4.5	Effects of quenching reaction of Ar* with H <sub>2</sub> O ( $\hat{t} = 10 \mu\text{s}$ ). . . . .	66
4.6	The test case for decay of the pure uniform argon plasma under the LFA. . . . .	67
4.7	The relaxation length for pure argon simulations at the peak voltage of pulse. . . . .	68
4.8	Temporal and spatial resolution study for Case 2 from uniform state through one pulse. . . . .	70
4.9	Comparison of variable and constant time stepping for Case 2. . . . .	71
4.10	Number density profiles at $\hat{t} = 20 \mu\text{s}$ for different pulse numbers, Case 1a. . . . .	71
4.11	Periodic states of simulations carried out for the initial number densities listed in Table 4.5. Total current $I(t)$ at cathode, Case 1a. . . . .	72
4.12	Potential distribution $\phi(x)$ , Case 1a. . . . .	73
4.13	Effect of uncertainty in input voltage profile on solution for Case 1a. . . . .	74
4.14	Decay profiles for pure argon with LFA (Case 1a), pure argon with energy equation (Case 1b), and argon-water mixture with energy equation (Case 2). . . . .	75
4.15	Decay profiles for argon-water simulations with different water percentages (variations of Case 2 model). . . . .	76
4.16	Number densities for two different chemistry models at the end of the decay period ( $\hat{t} = 33 \mu\text{s}$ ). . . . .	76
4.17	Comparison of the total current and the normalized $n_e$ profiles for different models. Results shown for one repetition period ( $33 \mu\text{s}$ ) in the periodic state. . . . .	77
5.1	The electron energy relaxation length calculated by using elastic and excitation collision frequencies of argon from Bolsig+ and LxCAT [40, 101] with respect to mean electron energy for various pressures. . . . .	81
5.2	Temporal and spatial resolution study for the simulations with $T_e$ equations. . . . .	85
5.3	Variables' spatial variation at the pulse peak. . . . .	86
5.4	The variation of the electron temperature spatially for various times at the 5th pulse. . . . .	87
5.5	Temporal variation of variables during the 5th pulse computations. . . . .	88
5.6	Normalized electron number densities and average electron temperature for local and non-local approximations. . . . .	88

Figure	Page
5.7 Decay profile comparisons with the experimental data [83] for pure argon with LFA, pure argon with energy equation (0-D), and argon-water mixture with energy equation (0-D), and argon-water mixture with energy equation(1-D). . . . .	89
5.8 Comparison of the total current with the experimental data [83] at the cathode for pure argon with LFA, pure argon with energy equation (0-D), and argon-water mixture with energy equation (0-D) ,and argon-water mixture with energy equation(1-D). . . . .	91
B.1 Comparisons of the different reaction rates from various studies for the excitation and ionization of argon from the ground level. . . . .	107
B.2 Comparisons of the different reaction rates from various studies for the de-excitation and step wise ionization of argon from the excited level. . .	108
B.3 Mean electron temperature variation with respect to reduced electric fields from different databases: Triniti [65], Hayashi [73], Itikawa [74], Morgan [75] for <i>Argon + 0.1% H<sub>2</sub>O</i> mixture . . . . .	109

## SYMBOLS

$n_{i,e}$	number density of ions or electrons [ $\text{m}^{-3}$ ]
$\phi$	potential [V]
$E$	electric field [V/m]
$\Gamma$	species flux [ $\text{m}^{-2}\text{s}^{-1}$ ]
$\mu$	mobility coefficient [ $\text{m}^2/(\text{V}\cdot\text{s})$ ]
$D$	diffusion coefficient [ $\text{m}^2/\text{s}$ ]
$\epsilon_0$	permittivity of free space [ $\text{C}^2/(\text{N}\cdot\text{m}^2)$ ]
$P$	pressure [Torr] or [Pa]
$T_{n,i,e}$	temperature of neutrals, ions or electrons [K ] or [eV]
$q$	elementary charge [C]
$\rho$	space charge density [ $\text{C}\cdot\text{m}^{-3}$ ]
$\tau$	time scale [s]
$s$	sign operator, + for ions and – for electrons
$Q_{beam}$	beam power [ $\text{W}/\text{m}^3$ ]
$k_b$	Boltzmann constant [J/K]
$\alpha$	ionization coefficient [1/cm]
$P_d$	dissipated power [ $\text{W}/\text{m}^3$ ]
$F_b$	body force [ $\text{N}/\text{m}^3$ ]
$\gamma$	secondary ionization coefficient
$I$	current [A]
$\nu$	frequency [ $\text{s}^{-1}$ ]
$\sigma_0$	momentum cross section [ $\text{m}^2$ ]
$F_{i,v}$	inviscid and viscous fluxes in x - direction [ $\text{m}^2$ ]
$G_{i,v}$	inviscid and viscous fluxes in y - direction [ $\text{m}^2$ ]

$F_b(x, y, t)$	body force
$Q(x, y, t)$	plasma heating on the flow [W/m <sup>3</sup> ]
$E_{abs}(X)$	absolute error, in the unit of X
$E_{rel}(X)$	relative error, dimensionless

## ABBREVIATIONS

DBD	Dielectric Barrier Discharge
DSMC	Direct Simulation Monte Carlo
EEDF	Electron Energy Distribution Function
HPEM	Hybrid Plasma Equipment Model
LFA	Local Field Approximations
LMEA	Local Mean Energy Approximation
LTP	Low Temperature Plasma
MCC	Monte Carlo Collisions
PIC	Particle in Cell
RF	Radio Frequency

## ABSTRACT

Piskin, Tugba Ph.D., Purdue University, December 2019. Numerical Simulations of Gas Discharges for Flow Control Applications. Major Professor: Jonathan Poggie.

In the aerospace industry, gas discharges have gained importance with the exploration of their performance and capabilities for flow control and combustion. Tunable properties of plasma make gas discharges efficient tools for various purposes. Since the scales of plasma and the available technology limit the knowledge gained from experimental studies, computational studies are essential to understand the results of experimental studies. The temporal and spatial scales of plasma also restrict the numerical studies. It is a necessity to use an idealized model, in which enough physics is captured, while the computational costs are acceptable.

In this work, numerical simulations of different low-pressure gas discharges are presented with a detailed analysis of the numerical approach. A one moment model is employed for DC glow discharges and nanosecond-pulse discharges. The cheapest method regarding the modeling and simulation costs is chosen by checking the requirements of the fundamental processes of gas discharges. The verification of one-moment 1-D glow discharges with constant electron temperature variation is achieved by comparing other computational results.

The one moment model for pulse discharge simulation aims to capture the information from the experimental data for low-pressure argon discharges. Since the constant temperature assumption is crude, the local field approximation is investigated to obtain the data for electron temperature. It was observed that experimental data and computational data do not match because of the stagnant decay of electron number densities and temperatures. At the suggestion of the experimental group, water vapor was added as an impurity to the plasma chemistry. Although there was

an improvement with the addition of water vapor, the results were still not in good agreement with experiment.

The applicability of the local field approximation was investigated, and non-local effects were included in the context of an averaged energy equation. A 0-D electron temperature equation was employed with the collision frequencies obtained from the local field approximation. It was observed that the shape of the decay profiles matched with the experimental data. The number densities; however, are less almost an order of magnitude.

As a final step, the two-moment model, one-moment model plus thermal electron energy equation, was solved to involve non-local effects. The two-moment model allows capturing of non-local effects and improves agreement with the experimental data. Overall, it was observed that non-local regions dominate low-pressure pulsed discharges. The local field approximation is not adequate to solve these types of discharges.

## 1. INTRODUCTION

Plasma is known as the fourth state of matter, where charged particles and unstable and stable neutral particles influenced by the electromagnetic forces are mixed together. Since interstellar and intergalactic space is penetrated by magnetic fields and carries a current [1, 2], it is believed that the plasma is the most common state of matter in the universe. In science and engineering, a broad range of plasmas exist from natural to created plasmas, Fig. 1.1. Plasmas are categorized according to their characteristics; the degree of ionization ( $n_i/N$  -weakly,  $10^{-6} - 10^{-4}$ , and fully,  $\approx 1$ ), thermal properties, neutrality, pressure (low  $< 7.6 \times 10^{-3}$  Torr, medium  $\approx 0.76$  Torr, and high  $\approx 760$  Torr), frequency (DC, AC, RF, microwave, and nanosecond discharges), and magnetization [3].

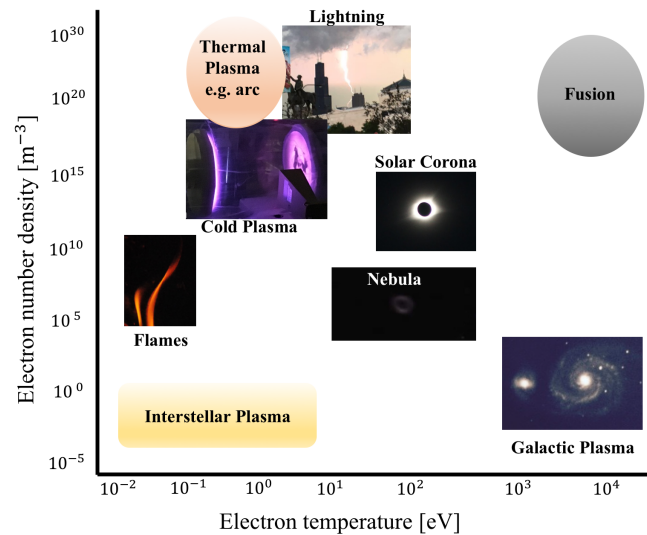


Fig. 1.1. Electron temperatures and number densities for various plasma across universe, redrawn from following works: [3, 4]. Photographs by the author.

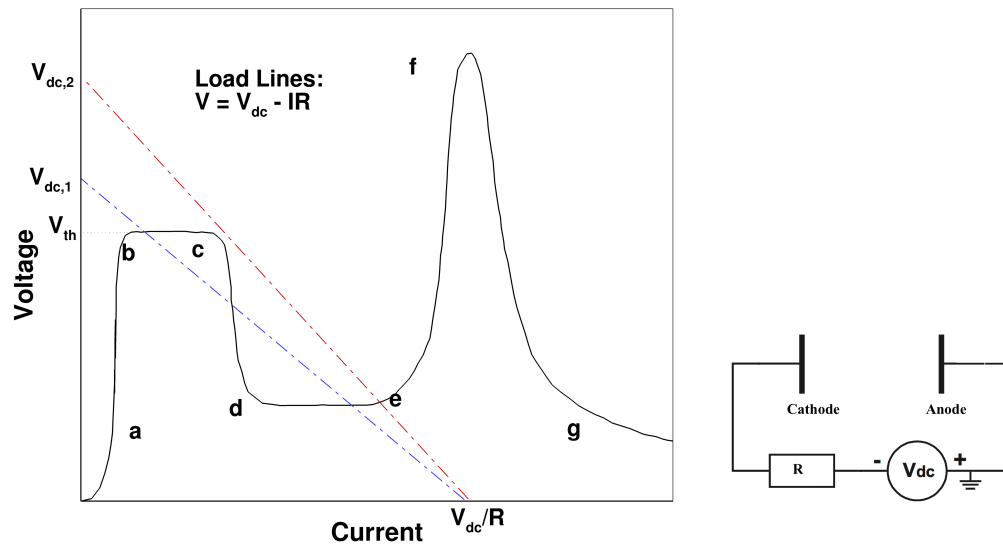
Plasma can be created by adding thermal energy or electrical energy. For the former case, heating of the gas will create ionization when the temperature is on the order of thousands of Kelvins. Because of the high temperatures of the neutrals and ions, this kind of plasma is considered as a hot plasma, as in hypersonic re-entry plasmas. It is possible; however, to achieve a plasma with low ion and neutral temperature by applying a strong electric field. This plasma is known as cold plasma, or low-temperature plasma, LTP since high heating of gas is not required.

Most of the created plasmas can be categorized according to their thermal properties as non-equilibrium and equilibrium. In the non-equilibrium plasmas, the bulk gas and ions temperatures are in the order of the room temperature  $\sim 10^2 K$ , whereas electron temperature is in the order of eV,  $\sim 10^4 K$ , such as glow, corona, dielectric barrier, and RF discharges. Equilibrium plasmas have charged particles and neutrals at temperatures with the same order of magnitudes, for instance lightning, arc discharge, and thermonuclear fusion [5]. Electron temperatures and number densities of these plasmas can be seen in Fig. 1.1.

The utility of plasma has been increasing in aerospace engineering through applications in aerodynamic flow control and combustion enhancement. Since the main interest of this study is low-temperature gas discharges; the discussion will cover gas discharges. Gas discharges have been studied to manage a desirable flow state. In this chapter, different discharge behaviors are described. Studies on the applications of plasma actuators for flow control are briefly summarized with the computational approaches. The challenges of discharge simulations are discussed with the simple example simulation of a glow discharge at low pressure. Finally, the motivation, objective, and the outline of the thesis are given.

## 1.1 Introduction to Gas Discharges

Gas discharges are the most common plasma application in various engineering fields. In this section, an overview of gas discharges is presented for DC discharges. It is assumed that there are free electrons in the domain to start to discharge processes.



(a) Voltage vs. Current plot

(b) Representation of the circuit.

Fig. 1.2. Current- Voltage characteristics of DC discharges, redrawn based on figures in Refs. [5,6]

Beyond the threshold voltage, the voltage differences will be enough to accelerate electrons and ionize neutrals with electron impact reactions; this process increases the number densities of charged particles. However, the number densities are still small; therefore, the electric field stays almost linear, unperturbed by space charge effects in the domain. This regime is called a dark discharge or Townsend discharge.

Townsend explained the electron avalanche mechanism and introduced the ionization coefficient,  $\alpha$ , which is the average number of electrons produced through the motion of one electron in a unit length. The schematic representation of the avalanche process is shown in Fig. 1.3(a), where electrons will create electron-ion pair with col-

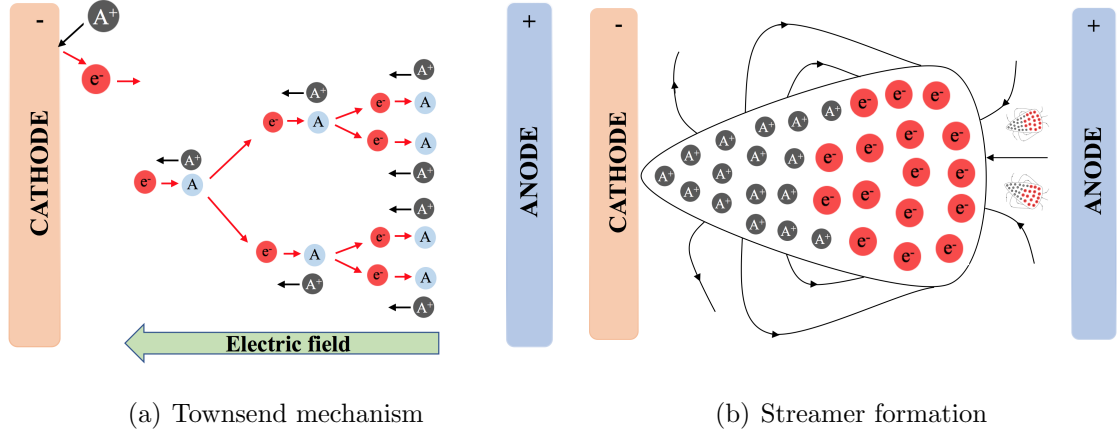


Fig. 1.3. The schematic representation of the multiplications of electrons.

liding neutral particles; two electrons will collide to create two additional electrons and an ion pair and so on. The growth of electrons is exponential in the avalanche process. This domain is represented in Fig. 1.2 as Region b-c. It can be seen that the b-c line is almost horizontal. With a small voltage increment, additional electrons and ions will be created with the avalanche mechanism or secondary emission at the cathode [6]. The increment of the current from the current at point b,  $I_b$  in Fig. 1.2 can be written as [6, 7]:

$$I = I_b \frac{e^{(\alpha d)}}{1 - \gamma(e^{(\alpha d)} - 1)} \quad (1.1)$$

where  $d$  is the distance between electrodes. Eqn. 1.1 includes the effects of electrons emitted by the electrodes by ion bombardment. It is clear that the breakdown voltage is dependent on the distance. However, it also depends on the pressure because the mean free path of collisions will decrease proportionally when pressure increases. For low pressures, electrons require longer distances to achieve ionization reactions. Pressure times distance,  $pd$  is the first similarity variable. Paschen conducted the experiment to show that breakdown voltage is the function of the  $pd$  and the type of gas [8]. The scaling with the same  $pd$  value should give the same cathode voltage fall if the all other conditions remain constant.

The transition from a dark discharge to a glow discharge can be seen in Region c-d. Further development of charged particles will increase the plasma density, and the electric field will be altered. The positive and negative sheaths will begin to appear because of the difference in the mobilities of charged particles. Since the collection of positive ions near the cathode sheath will alter the electric field, it will cause a voltage drop. This transition is known as an unstable process and can cause pattern formation [6].

The glow discharge regime is obtained in Region d-e when voltage drop reaches steady and stable values. The current increases at a constant voltage. If a normal glow discharge is obtained, a current is transferred from only a portion of the cathode surface, and current density is approximately constant. An increase in the current will correspond to an increase in the cathode area that transfers current. If the full cathode surface is involved in transferring current, the glow discharge is known as an abnormal glow discharge. In this regime, current growth will require higher voltage. This regime is shown as Region e-f in Fig. 1.2.

This high voltage and high current values will yield more gas heating and thermionic electron emission. Those effects will reduce the necessary voltage value to sustain a plasma. This usually happens in the transition from glow to arc discharge. The transition zone can be considered as Region f-g; also, the region after g point is known as arc discharge.

Other discharge types, corona and streamer discharges, are not shown in Fig.1.2 in which profiles are described for low-pressure values. Pressures near atmospheric pressure might have different profiles than the one plotted in Fig.1.2. High-pressure discharges require higher breakdown voltage or threshold voltage. Also, Townsend—avalanche breakdown might lead to the streamer breakdown processes. Streamers occur when the electrons start to collect on the front of the avalanche. Polarized avalanche will cause a higher electric field on the local regions; the high local field will promote the growth of a streamer. Therefore, a head (negatively charged) and tail (positively charged) of a streamer will appear, Fig. 1.3(b). Since the number

of electrons is large on the head of the avalanche, they will be able to shield the applied field. There will be secondary streamers on the head of the primary streamer because of the local high electric field. Large streamers can cause a transition to an arc. In order to prevent the transition to arc discharge, dielectric barriers are used to eliminate spark formation. Corona discharges are also atmospheric pressure discharges, in which one electrode achieves extremely high electric field and photo-ionization in the vicinity.

Load lines represent the effects of the external circuit and determine the solution for a given voltage and resistance. In Fig.1.2, the red load line crosses the current-voltage characteristic line in the glow discharge regime. In contrast, the blue load line in Fig. 1.2 crosses the current-voltage characteristic line in the dark discharge, transition, and glow discharge regimes. For a given external circuit, there may be multiple solutions, each of which may be stable or unstable.

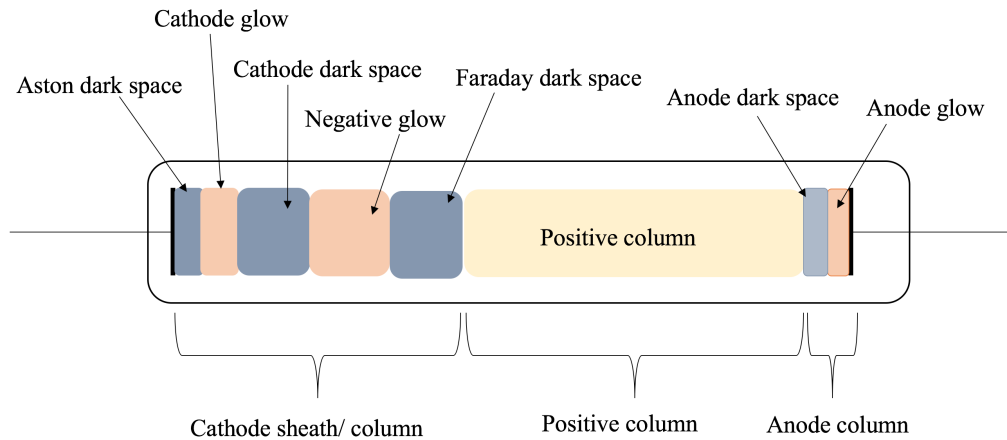


Fig. 1.4. Column organization in glow discharges and distinct regions [5,6].

The column organization in the glow discharges will be discussed here to clarify the discussion as well as the language used in the following chapters. There are eight distinct regions, as represented in Fig. 1.4. Electrons emitted from ion-electronic emission have lower energy; thus, they will not have enough energy to react and to

produce photon emission; this region is known as Aston dark space. In the electric field near the cathode, electrons gain enough energy to create a small bright area as known as cathode glow. At the cathode dark space, an electron avalanche process starts because electrons have enough energy to cause impact ionization. The high electron number density after cathode dark space reduces the electric field, and the only light will appear at the negative glow. Electrons lose their energy through reactions; lower energy and high numbers of electrons create the Faraday dark space. Electrons gain kinetic energy again to achieve a quasi-neutral region, which is known as the positive column. Low electric field, but the high number densities of the electrons cause excitation and luminance in the positive column. The anode repels ions and removes electrons from the positive column. The decrement in the electron number densities creates a dark space near the anode. The charge separation will cause a higher electric field than the positive column; electrons gain energy towards the anode, and they will create photon emission. Two distinct regions can be observed at the vicinity of anode [5, 6].

Although the energy gain and loss of electrons can create eight distinct regions, the distinctions between these regions are not always clear because of the dimensions of regions – they can diffuse into each other. Numerical simulation of these eight distinct regions is restricted by the computational model and cost. Fluid models have employed Townsends first ionization coefficient in regions where the electrons reach equilibrium with the electric field. However, the electric field in the cathode vicinity varies rapidly with the distance, so equilibrium cannot be reached. Therefore, an equilibrium assumption should not be used in the analysis of this region. A kinetic approach is well suited to such problems. So, it is considered here that there are three distinct regions as cathode column/sheath, positive column and anode column for future investigations.

## 1.2 Applications in Aerospace Engineering

Optimization in the aerospace industry is focused on the reduction of fuel consumption, improvements in flight safety, and reduction of pollution. Applications of plasmas to these problems have been growing rapidly because of the tunable properties of plasmas. The properties of plasma can help to achieve industry goals. In this section, the utilization of plasma in the aerospace industry will be discussed, including plasma propulsion and plasma aerodynamics.

One of the eminent usages of plasma in the aerospace industry is plasma propulsion for space flight. Although plasma propulsion is not useful for the launch because of low thrust production, it is preferable for space flight due to high specific impulse and high exhaust velocity. There are three types of plasma thruster; electrothermal (resistojet, arcjet), electrostatic (ion thruster, gridded ion thruster), and electromagnetic (Hall thruster, pulsed plasma thruster, magneto plasma dynamic thruster - MPD, the variable specific impulse magnetoplasma rocket -VASIMR) thrusters [9]. Plasma thrusters have been studied experimentally to analyze and to understand fundamental principles and parameters. While the overall understanding of a plasma thruster's operations is almost complete, there are a couple of outstanding scientific questions requiring further detailed analysis and measurements. Computational studies may help to improve the understanding of these points: plasma-wall interactions, fluctuations in the electron number densities, instabilities, and trajectories of charged particles [10,11].

### 1.2.1 Reentry plasma

The first interest of the interactions of plasma sciences and aerospace engineering goes back to the times of the first space flight [12], and this is the only natural plasma discussed in this section. During atmospheric re-entry, the extreme kinetic energy because of gravitational acceleration causes a great amount of heating; thus, gas temperatures around the body will be large enough to create dissociation, exci-

tation, and ionization reactions, and finally plasma. A challenging result of re-entry plasmas is the communication blackout; when plasma has a higher frequency than the communication bands [13]. There are several methods which have been proposed to overcome the communication blackout: remote antenna configurations- antennas out of the plasma layer, quenchant injection to cool the plasma layer, and a magnetic window to open communication by decreasing the electron number densities [14].

### 1.2.2 Flow control applications

Flow control is considered as any attempt to change flow characteristics to have more desirable flow parameters, such as delay in a stall, drag reduction, mitigation of noise, and lift improvement. There are two basic types of flow control devices: passive and active. Passive control devices do not require any additional energy to work. Because they change the geometry of the surface, the influence of these devices is continuous through the flow at all times. Example of passive flow control devices includes finite height roughness [15], Gurney flaps [16], and fixed vortex generators [17]. The main reason to change in the surface of a body is to alter the pressure gradients favorably. The passive control devices are useful in specific flow conditions; however, they might reduce performance outside of these conditions.

The second type, active control devices, need energy input to work. They can also be used at the right moments with feedback from flow sensors. There are various types of active flow control mechanisms, which can be classified according to their interaction with the flow: change in the geometry, and adding/removing of mass, momentum, and energy. By changing the effective camber, geometrical devices are used to control stall to help in high angle attack and in low airspeed flight situations [18]. Mass and momentum can be added and removed from the system by using fluidic actuators [19]. Plasma actuators alter the boundary layer characteristics by adding force and heat to the system.

The time scales in the plasma is almost zero compared to the outer flow; thus, plasma actuators have a broad range of applications for flow control, including the control of laminar flow, transition, turbulent flow, separation, shock wave pattern, shock-boundary layer interactions, and so on [20]. The effects of plasma actuators can be categorized as gas heating and momentum transfer through electrostatic and magneto-hydrodynamic effects. Gas heating is mainly caused by the interactions of flow and energy relaxation in the plasma. The reactions are the fundamental mechanism to transfer heat from the plasma through the relaxation of vibrational relaxation, quenching, and recombination reactions. Momentum transfer through the electric field happens because of charge separation, interacting with the flow as a body force.

It has been shown that heating of the boundary layer using a plasma actuator can weaken an oblique shock in supersonic flow ( $M = 2.5$ ) over a wedge [21]. The excitation of bulk flow species by electrons, attachment of electrons to bulk gases, and quenching of bulk flow with excited species of plasma change the physicochemical process in bulk flow by introducing non-equilibrium in internal degrees of bulk gases. A relation between shock wave propagation and pulse repetition frequency is observed due to thermalization of plasma in between pulses which alters the thermodynamics of flow [22]. Alternative approaches have developed to promote the heating and spatial non-uniformity by plasma such as plasma injection [23].

One of the main uses of actuators is to eliminate a separation during flight. Separation happens when streamlines become detached from the surface of a flying object because of adverse pressure gradients; separation causes a stall and an increment in the drag. Plasma can create a body force aligned in the flow direction, and heating from plasma can increase momentum at the separated region. These two effects will help to reduce separation region [24, 25]. The electrostatic body force is non-zero when plasma is not quasi-neutral, as in cathode sheaths. Dielectric barrier discharges are obtained by covering one or both of electrodes with a dielectric material to eliminate the transition from glow to arc regime. Since most flow control is needed for

conditions near atmospheric pressure, a transition to the arc is likely. Therefore, a dielectric layer — glass, Teflon, Kapton, and so on — is used to eliminate the transition to spark by reducing the electric field through charge accumulation.

The schematic of a single dielectric barrier discharge - DBD is shown in Fig.1.5. Induced flow from plasma helps to add momentum to the bulk flow. Induced velocity,  $v_{ind}$  can be obtained from plasma by using Poisson's equation and volumetric force as [20, 26]:

$$v_{ind} = E \left( \frac{\epsilon_0}{\rho} \right)^{1/2} \quad \text{or} \quad v_{ind} = k_g \sqrt{\frac{I}{\rho \mu_{ion}}} \quad (1.2)$$

where  $\epsilon_0$  is the permittivity of free space,  $k_g$  [ $\text{m}^{-1/2}$ ] is the geometric factor,  $\mu_{ion}$  is ion mobility,  $I$  is current, and  $\rho$  is the gas density.

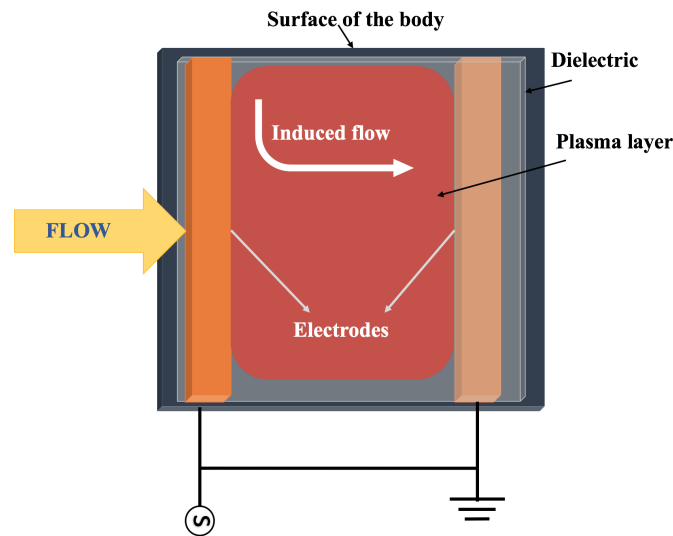


Fig. 1.5. The schematic representation of the DBD plasma actuator.

The MHD effects of plasma actuators can also be used for flow control purposes. As mentioned earlier, MHD effects can be used to open a communication window during re-entry. The reduction in the shock-induced separation zone is observed by using the MHD effects. By applying a magnetic field ( order of  $\sim 10^0 - 10^1$  Tesla)

and arranging the Lorentz force aligned with the separation zone will help to decrease the separation zone [27].

Three processes are described to understand the interaction of plasma and bulk flow: gas heating, momentum transfer through electrostatics or MHD effects. Discharges have distinct properties depending on the conditions under which they are obtained. Finding the cheapest and the most efficient discharge model strictly depends on the understanding of plasma and its thermodynamics and chemistry.

The effectiveness of an active flow control mechanism can be described by a few parameters. It is essential for these systems to have a fast response to changes in the flow field. They should withstand rough environments; moreover, they should be easy to replace with the consideration of the expense and the simplicity [28]. A plasma actuator is one of the devices which can satisfy almost all these requirements except the need for external voltage supply. Thus, plasma actuators can be more attractive compared to conventional flow control devices because of having no mechanical parts, fast response time, availability to use any kind of body/flow, and resistance to higher forces (such as  $g$ ). As discussed in the following section, physical processes in plasma occur very quickly, and thus a fast response time is achieved.

Experimental studies [29] have shown that plasma actuators are viable. Further developments of actuators depend on the full understanding of the processes and interactions. Therefore, numerical and analytical —if possible— calculations are essential to address those problems which cannot be resolved experimentally and to prove the existing results from the experiments. The following section is devoted to the numerical studies for couplings of plasma actuator and flow solvers.

### 1.2.3 Computational Flow Control Studies

The physical model for an aerodynamic flow solver is the Navier-Stokes -NS- equations, Eqn. (1.3) & (1.4), and various forms of it with simplifications and correlations. It is mentioned in the following section that the temporal and spatial scales in plas-

mas are extremely small; the scales in plasmas are several orders smaller than that in air flow. The coupling between NS and discharge equations is extremely expensive in terms of computational requirements. Therefore, most of the computational efforts are focused on implementing the overall effects of an actuator on the flow as a body force, heating, or both. A reduction in the computational efforts can be achieved by considering the change in the momentum and energy of the local flow due to interactions with plasma actuators. The following equations, Eqn. (1.3) & (1.4), show the implementation of the effects on the governing equations. These equations are the vector form of conservation of mass, momentum, and energy in 2-D. One of the most important benefits of using of empirical source terms to model the actuators is that simulations with multiple actuators in the flow field are computationally possible. The conservation form of the NS equation is:

$$\frac{\partial U}{\partial t} + \frac{\partial F_i}{\partial x} - \frac{\partial F_v}{\partial x} + \frac{\partial G_i}{\partial y} - \frac{\partial G_v}{\partial y} = S \quad (1.3)$$

where U is the conservative flow variable vector, F and G are the flux vectors and S is the source term vector. The flux vectors are divided into two parts viscous( $F_v$  and  $G_v$ ) and inviscid ( $F_i$  and  $G_i$ ) components of the flow. The definitions of these terms are:

$$U = \begin{pmatrix} \rho \\ \rho u \\ \rho v \\ \rho E \end{pmatrix}, \quad F_i = \begin{pmatrix} \rho u \\ \rho u^2 + P \\ \rho uv \\ (\rho E + P)u \end{pmatrix}, \quad G_i = \begin{pmatrix} \rho v \\ \rho uv \\ \rho v^2 + P \\ (\rho E + P)v \end{pmatrix} \quad (1.4)$$

$$F_v = \begin{pmatrix} 0 \\ \tau_{xx} \\ \tau_{xy} \\ u\tau_{xx} + v\tau_{xy} + \kappa \frac{\partial T}{\partial x} \end{pmatrix}, \quad G_v = \begin{pmatrix} 0 \\ \tau_{xy} \\ \tau_{yy} \\ u\tau_{xy} + v\tau_{yy} + \kappa \frac{\partial T}{\partial y} \end{pmatrix}, \quad S = \begin{pmatrix} 0 \\ F_{b,x} \\ F_{b,y} \\ Q(x, y) \end{pmatrix}$$

where  $\tau_{ij} = \mu \left( \frac{\partial x_i}{\partial x_j} + \frac{\partial x_j}{\partial x_i} \right) + \lambda \delta_{ij} \nabla \cdot \mathbf{V}$  is the representation of viscous stresses. The variables  $\mu$  and  $\lambda$  are the coefficients of viscosity and bulk viscosity respectively. The viscous energy flux is  $E_{vi} = u\tau_{x,i} + v\tau_{i,y} + \kappa \frac{\partial T}{\partial x_i} + \sum_{n=1}^N \rho D_n h_n \frac{\partial Y_n}{\partial x_i}$ ; in which  $\kappa$  is the thermal conductivity,  $D$  is the diffusion coefficient,  $Y$  is the mole fraction of each species for total of  $N$  species. The diffusive energy flux is not shown in Eqn. 1.4. The terms  $F_b$  and  $Q$  are the body force and heating from plasma actuator which are implemented into the NS equations without solving conservation of charged particles and Poisson's equation.

With this empirical correlation between plasma and flow solvers, flow solvers can be operated time scales of the flow. Information about excited species cannot be obtained from this approach; however, because chemistry is missing. A more detailed model can include the mass conservation equation for each species, and including the actual body force and heating derived from the Maxwell equations [30]. However, the cost of modeling and computations will increase considerably.

#### 1.2.4 Plasma assisted combustion

Another field in aerospace engineering where applications of plasma technology can increase efficiency is combustion. It has been shown that plasma assisted combustion can improve mixing, flame stability, and chemical reactions due to heating [12,31]. In a review paper, Leonov and Yarantsev [32] listed four possible mechanisms of these improvements as ohmic heating of fuel and oxidizer, momentum transfer, production of excited and dissociated fuel and oxidizer particles, and instabilities from plasma. The local ohmic heating intensifies the reactions on these regions with increasing the air-fuel mixing [33]. The production of excited particles or radicals will help to improve reaction rates while reducing the power requirements. Leonov and Yarantsev [32] pointed out that longitudinal transverse instability of plasma filament causes the microscopic scale of mixing in the combustion zone.

### 1.3 Challenges of Gas Discharge Simulations

Experimental studies on plasma aerodynamics show that plasma actuators are feasible, and these studies are supported by simplified numerical studies. However, detailed calculations and explanations of plasma aerodynamics are not complete, and not easy to carry out. In this section, the challenges of numerical simulations will be described and presented for a simple discharge case.

The rule of thumb is that a detailed plasma model may cause a large numerical uncertainty and cost, whereas a highly simplified model will not be able to capture enough physics of the problem. Optimum simplifications to the physical model are required. However, there are strict numerical and physical restrictions on the computations because of the scales of processes in plasma. The magnitude of spatial and temporal scales, non-linear terms, and high gradients make plasma governing equations stiff. Numerical stiffness is usually mitigated by implicit methods; however, the stiffness of plasma equations cannot be completely eliminated with an implicit formulation.

The challenges of gas discharge simulation mostly arise from the discrepancy between the time scales of different processes. The fundamental mechanisms of gas discharges—ionization, drift, diffusion, and recombination—have considerably different time scales. Moreover, the time scale of each process will change with position in the domain because the electric field and gas state are distinct in different regions of plasma. Moreover, electrons and ions have different orders of magnitude for each process because of the disparity in their mass.

In order to illustrate the differences in time scales, a nitrogen gas simulation at 5 Torr with 2 cm gap is used. One dimensional drift-diffusion equations with the source term from Townsend ionization and recombination coefficients are solved in a loosely coupled manner with Poisson's equation. These coefficients and transport coefficients are listed in Table A.1 and A.2 with the case C1. Detailed descriptions of the governing equations are presented in the following chapter. The discharge con-

figuration is represented in Fig.1.2(b) with the external circuit containing a resistor. The electric field and the number densities from this simulation are shown in Fig. 1.6.

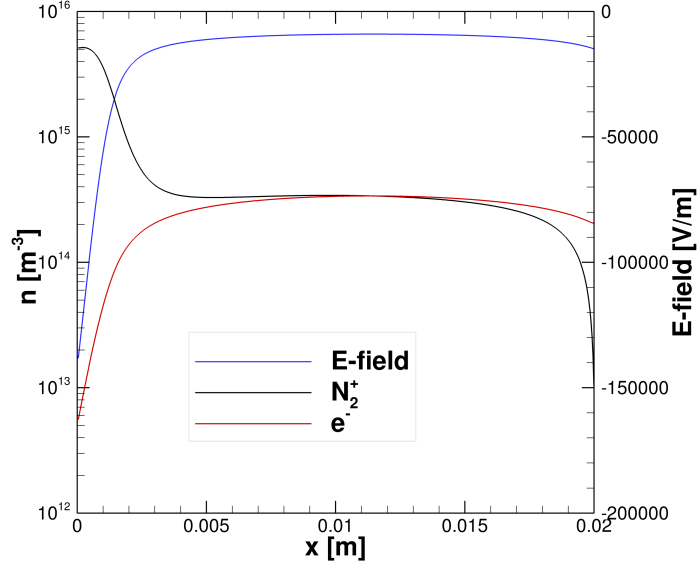


Fig. 1.6. The discharge simulation for  $N_2$  at 5 Torr with an external circuit consisting only resistance,  $R = 300 \text{ k}\Omega$  and  $V_e = 1000\text{V}$ .

The drift velocity of charged particles can be defined as  $v_{dr,s} = \mu_s \mathbf{E}$ . The required time for drift is simply  $\tau_{dr,s} = x/|v_{dr,s}|$  for each species. From Fig. 1.6, the spatial scales for the cathode sheath and the positive column are  $x_{cs} \approx 0.002 \text{ m}$  and  $x_{pc} \approx 0.018 \text{ m}$ . The absolute value of the largest E-field at the cathode sheath is approximately  $150000 \text{ V/m}$ , and it is  $10000 \text{ V/m}$  for the positive column.

The diffusion coefficient is obtained from the Einstein relation for this calculation, and the corresponding diffusion frequency is  $\tau_{dif} = 2D/\Lambda^2$ , where  $\Lambda$  is the characteristic diffusion length. Here  $\Lambda$  is assumed as the thickness of the sheath or positive column in this calculation.

As mentioned earlier, the Townsend coefficient,  $\alpha$ , is used to model the ionization process and the production of the charged particles. The Townsend coefficient has a non-linear dependence on the electric field; time scales for ionization will vary signifi-

cantly from the cathode sheath to the positive column. The decay of charged particles is governed by recombination coefficients. The ionization frequency is obtained from  $\tau_{ion} = 1/\alpha v_{dr,e}$  and the recombination frequencies are computed as  $\tau_r = \beta n_i$ .

Table 1.1 includes the values of the mentioned time scales for ions and electrons at the cathode sheath and positive columns. It can be seen that each mechanism has different time scales for each charged species at different locations. Without including magnetic fields, energy relaxations, high frequencies, and so on, a one-dimensional glow discharge at relatively low pressure already has significant differences between the smallest time scale, ionization in the cathode sheath ( $\Delta\tau = 1.6 \times 10^{-10}$  s), and the largest time scale, recombination at positive column ( $\Delta\tau = 5.0 \times 10^{-2}$  s).

Table 1.1.  
Time scales in seconds for different mechanisms.

	<b>Electron</b>		<b>Ion</b>	
	Positive Column	Cathode sheath	Positive Column	Cathode sheath
Drift	$1.2 \times 10^{-7}$	$9.5 \times 10^{-10}$	$2.3 \times 10^{-5}$	$1.7 \times 10^{-7}$
Diffusion	$1.3 \times 10^{-5}$	$1.6 \times 10^{-7}$	$8.2 \times 10^{-2}$	$1.0 \times 10^{-3}$
Ionization	$5.6 \times 10^{-5}$	<b><math>1.6 \times 10^{-10}</math></b>		
Recombination			<b><math>5.0 \times 10^{-2}</math></b>	$5.0 \times 10^{-3}$

The comparison of plasma and aerodynamic solutions is important in the context of the numerical coupling of plasma and flow solvers for flow control purposes. In Table 1.2, the plasma solution is compared with the data obtained from the simulations [34] of the experiment [35] for flow control studies. It should be noted that these numbers are obtained and calculated for specific cases; however, the scales are usually close to these orders for different studies. The scales of plasma and flow differ by a couple of orders of magnitude. The time scale is one of the challenges in combining these two solutions. As mentioned in the previous section, there are various studies on coupling these two solutions, but the detailed simulations and complete

understanding of the processes are still incomplete. Another important point is that gas discharges are usually not in thermal equilibrium, unlike the outer flow. Different temperature modes — electronic, vibrational, rotational, and translational — should be included in the flow solver to capture heating from the plasma correctly.

Table 1.2.  
Classification of simulation cases.

	Plasma Simulations	Aerodynamics Simulations
Time Scale	$\sim 10^{-10} s$	$\sim 10^{-4} s$
Domain Length	$\sim 10^{-2} m$	$\sim 10 m$
Maximum velocity	$\sim 10^7 m/s$	$\sim 10^3 m/s$
Thermal Equilibrium	mostly no	mostly yes

In addition to time scales and large gradients, there is one more source of stiffness caused by the quasi-neutral regions. To achieve the self-consistent solutions, the coupling between charged particle's conservation equations and Maxwell equations should be carried out. In the absence of magnetic fields, coupling is done through Gauss's law,  $\partial^2\phi/\partial x^2 = q(n_i - n_e)/\epsilon_0$ . The relative error of this equation will be magnified on the quasi- neutral regions where  $n_i \approx n_e$ . Relative error,  $E_{rel}$  indicates the quality of calculations relative to the actual value whereas absolute error,  $E_{abs}$  is the amount of physical error through the calculations. These are related as:

$$E_{rel}(x) = \frac{E_{abs}(x)}{x} = \frac{x_0 - x}{x} \quad (1.5)$$

where  $x$  is the actual value and  $x_0$  is the computational value. The relative error for Poisson equation can be written for the right hand side as:

$$E_{rel}(n_i - n_e) = \frac{n_i E_{rel}(n_i) + n_e E_{rel}(n_e)}{|n_i - n_e|} \quad (1.6)$$

It can be seen from Eqn.(1.6) that the relative error of Poisson's equation will increase rapidly through the quasi-neutrality. The number of iterations for solvers to converge will be larger in a quasi-neutral region. To overcome this stiffness, Parent et al. [36]

suggest a different approach based on charge conservation, to couple the governing equations with the Maxwell equations. In this version of the equations, the boundary conditions need to be reformulated to assure that Gauss's law is satisfied on the overall domain.

Four processes are chosen to show the discrepancy in the time scales. However, there are more restrictive time scales limiting the simulations to lower time scales; the CFL and dielectric relaxation scales. These time scales will be discussed in the following chapter with the progress toward overcoming these limits. The thicknesses of the various discharge regions (Fig. 1.4) show the changes in the spatial scales; large gradients in the electric field will promote the growth of non-linearities. The cathode sheath is a small region with large gradients, whereas the positive column is a region of almost zero gradients. These two regions create numerical difficulties and limitations, and the handling mechanism for this study will be described in the following chapter.

## 1.4 This Dissertation: Motivation, Objective, Organization

### Motivation

The application fields of low-temperature plasma have been growing extensively over the last couple of decades with the support of the experimental and numerical studies. Although the interest in the experimental studies has continued to increase, the number of computational studies has decreased [37]. As discussed in *The 2017 Plasma Roadmap: Low-Temperature Plasma Science and Technology* [37], the understanding of the fundamental processes in plasma physics is still not complete, and the future of low-temperature plasma science depends on the development of theoretical and computational studies along with experimental studies.

As mentioned earlier, the temporal and spatial scales in electric discharges can be extremely small; detailed computations require further development of the current

technological abilities. Some questions are beyond our experimental skills and must be answered theoretically and computationally.

In addition to the contribution to computational studies, another motivation of this study is to explore plasma chemistry. The complete understanding of interactions between plasma chemistry and operation conditions might help to resolve severe problems in terms of engineering, environment, health, and so on. For instance, fluorescent lamps are dominating the illumination industry because of their energy efficiency; however, they present landfills with toxic substances - mercury, arsenic, copper, and lead [38]. It has been shown that adding impurities, such as water to Argon, helps to improve plasma light efficacy compared to conventional fluorescent lamps [39]. Although the main interest is to develop computational tools for flow control purposes; the outcome of plasma studies can be used interchangeably across the different fields.

## **Objective**

The objective of this study is to address the numerical and physical problems in detail by analyzing the requirements of the discharge. Therefore, an optimum model can be investigated for different discharge simulations. Another purpose is to show the effects of the use of different simplifications, such as the Local Field Approximation (LFA), on different discharge problems. The limitations and the variations in between models are investigated to comment about the numerical and physical approaches. Since a simplified model is required to achieve coupling with a flow solver, the simplest possible model is chosen to observe how much physics can be captured. To quantify the discrepancy between models, the comparisons with an experimental study is carried out.

Lower dimensional solutions in plasma are useful to get a quick idea about the plasma behaviors and characteristics. Since the computational efforts and cost grow with multi-dimensional simulations, 1-D and 0-D solutions are employed to observe

the number densities, current, and electron temperatures. Their capability of gathering information about plasma is discussed, and alternatives are investigated. The aim is to define and analyze the essential physics of different discharge problems to optimize computational cost. The local field approximations are great simplifications, and their capability is investigated for low-pressure nanosecond pulse discharges.

Another aim is the validation of the computations with experimental data. It is important to have a consistent result experimentally and numerically. It is; however, challenging to simulate the experiments because of the length of the operation time, noise in the input data, and the uncertainty of measured data. Improvements in the physical model are achieved in stages to capture the correct physics.

## Outline

In Chapter 2, Methods; different physical models are presented with the derivation of the current model. A short background on the different physical models is given. Numerical approaches are presented with the modifications and improvements. The fundamentals discussed in the Introduction, Chapter 1, are expanded in this chapter to show the characteristics of 1-D DC discharges.

In Chapter 3, The Local Field Approximation, the definition and the description of the local field approximation are presented. The usage of the LFA solver is demonstrated, and it is shown that the solver, Bolsig+ [40], produces acceptable results by comparing with the other solvers and swarm data. In this chapter, information from Bolsig+ used in the solver is presented.

In Chapter 4, Simulations with the LFA and improvements on the LFA, the simple drift-diffusion model is improved with the addition of electron temperatures obtained from the local field. Comparisons and discussions of mismatches are provided with the improvement of the numerical and physical models.

In Chapter 5, Simulations with the Non Local Effects, the limitations of the LFA are explained and quantified for different pressures. The results with the electron

thermal energy equation are presented and compared with the experimental data. The final comparisons between physical models are given in this chapter.

In Chapter 6, Conclusions, conclusions, and recommendations for future work are presented.

In Appendix A and B, Coefficients and Constants for the Simulations, and Discussion about Reaction Rates; the detailed list and comparisons of coefficients from literature are investigated.

## 2. METHODS

In the previous chapter, the fundamentals of gas discharges were discussed and applications in the aerospace industry were surveyed along with the challenges for numerical simulations. In this chapter, physical and numerical models are discussed for different types of discharges. Each electric discharge has its own properties depending on the applied voltage, pressure, gap distance, and gas type. Sudden variations of temporal and spatial scales in plasma cause numerical stiffness. Disparities in plasma scales are one of the important factor altering modeling strategies.

In the first part of this chapter, the fundamental equations for discharge physics are described for kinetic, fluid, and hybrid approaches, and a literature review is presented for these physical approaches. The limits for usage of three different models will be discussed. In the second half of this chapter, the numerical approaches, boundary conditions, simplification, resolution studies, and acceleration mechanisms are described. The simplified model is explored in the context of 1D low-pressure glow discharges, and different phenomena are checked and observed.

### 2.1 Physical Modeling

Since the origin of different approaches for gas discharge simulations is the microscopic description, the Boltzmann equation and its moments will be described, and approaches for solving them will be investigated. The Boltzmann equation is:

$$\frac{\partial f_i}{\partial t} + \vec{v}_i \cdot \nabla f_i + \frac{\vec{F}_i}{m_i} \cdot \nabla_v f_i = R(f_i) \quad (2.1)$$

where  $f = f(x, y, z, v_x, v_y, v_z, t)$  is the distribution function for the corresponding species,  $i$ ,  $\vec{F}$  is the long-range force acting on the species, and  $R(f_i)$  represents the rate of change of the distribution function because of reactions and radiations. The

symbols  $\nabla$  and  $\nabla_v$  are the gradient operator in physical space and velocity space, respectively.

The coupling between Maxwell's equations and plasma solver to enable a self-consistent solution is the main principle of numerical approaches trying to simulate discharges. The simulation of even one species will be extremely difficult considering the number of dimensions. State of the art computational methods have been developed to overcome the numerical complexity and costs. The categorization of these methods is necessary to understand the differences, simplifications, and the applicability of these methods. These numerical models can be classified into three categories:

- particle approaches
- continuum approaches
- hybrid approaches.

In this section, brief descriptions of different numerical models and the simplifications for the Boltzmann equation of each model are presented.

### 2.1.1 Particle Approach

The particle, or kinetic, approach aims to obtain the distribution functions of species in time and space. Different models have been developed to capture detailed information: Particle in Cell- PIC, Direct Simulation Monte Carlo- DSMC, direct integration of the Boltzmann equation, and combinations of these models.

Monte Carlo, MC models track representative particles in space and time, and elastic and inelastic collisions are modeled stochastically. MC captures a particle's trajectory under the influence of electromagnetic forces, and its trajectory is disturbed randomly by collisions [41]. A large number of particles must be tracked to capture the behaviors of particles accurately.

Particle in Cell, PIC, is another statistical approach to capture distribution functions in which non-linear, space charge, and collective behaviors of plasma are modeled without having significant simplifications. PIC methods consider particles on weighted distributions on the space (in a cell), and fields are calculated over discrete cells. PIC models have struggled to resolve the tail of the distribution function where the population is less statistically resolved [42]. PIC-MC models have also developed as a computational technique for discharge problems at low pressure [43].

The direct integration of the Boltzmann equation is another particle method. The convective nature of the equation creates the stiffness in the model; flux correction or convective schemes are required [25, 44].

Despite the fact that particle approaches produce the most detailed description of a plasma, computational requirements are enormous. With the current technological infrastructure, kinetic models are not appropriate for most discharge problems. However, their accuracy in the discharge simulation, especially in low pressures, makes kinetic approaches a must-have for the future of discharge simulations.

### 2.1.2 Continuum Approach

Continuum, or fluid, approaches are obtained by describing the plasma characteristic more collectively than the particle approaches in terms of variables such as density, mean energy, etc. Mass, momentum, and energy conservation of particles are obtained from the moments of the Boltzmann equation. Fluid models capture the physics accurately if the collision frequency is high; that is, when the mean free path of collisions is smaller than the characteristic plasma size. There are parameters to check the applicability of the fluid equations, such as pressure and Knudsen number, the ratio of the mean free path to the discharge scales. By comparing the discharge results for various pressures, it has been observed that pressures lower than 100 mTorr require a kinetic approach [45]. Plasma thrusters and plasma propul-

sion simulations are dependent on the kinetic approach because of the vacuum or near-vacuum conditions.

The governing equations for plasma fluids can be listed as following for each species from the study of Colella and et al. [46]:

Mass equation:

$$\frac{\partial m_i n_i}{\partial t} + \nabla \cdot (m_i n_i u_i) = \sum_j S_{ij} \quad (2.2)$$

Momentum equation:

$$\begin{aligned} & \frac{\partial m_i n_i u_i}{\partial t} + \nabla \cdot (m_i n_i u_i u_i) = \\ & \nabla \cdot (n_i k T_i) + q_i n_i E - \sum_j \frac{m_i m_j}{m_i + m_j} n_i \nu_{ij} (u_i - u_j) + \sum_j m_i u_i S_{ij} \end{aligned} \quad (2.3)$$

Energy equation:

$$\begin{aligned} & \frac{\partial}{\partial t} \left[ n_i \left( \frac{m_i}{2} u_i \cdot u_i + \varepsilon_i \right) \right] + \nabla \cdot \left[ n_i \left( \frac{m_i}{2} u_i \cdot u_i + \varepsilon_i \right) u_i \right] = \\ & \nabla \cdot (n_i k_b T_i u_i) + q_i n_i u_i \cdot E + \sum_{i,j} \left( \frac{m_i}{2} u_i \cdot u_i + \varepsilon_i \right) S_{ij} + \sum_j \epsilon_{ij} R_{ij} \\ & - \sum_j \frac{2m_i m_j}{(m_i + m_j)^2} n_i \nu_{ij} \left[ \frac{1}{2} (m_i u_i \cdot u_i - m_j u_j \cdot u_j + (m_j - m_i) u_i \cdot u_j) + \varepsilon_i - \varepsilon_j \right] \end{aligned} \quad (2.4)$$

where  $\varepsilon_i = \frac{k_B T_i}{\gamma_i - 1}$  is the internal energy of the particles.  $\gamma_i = 5/3$  is the ratio of specific heats.  $i$  is the index notation for the ions, electrons and neutrals.  $n_i$  is the number density of each particles with the velocities,  $u_i$  and mass,  $m_i$ . The corresponding charge of species is  $q_i$  and temperature is  $T_i$ .  $S$  and  $R$  are the rate of production and loss of number density of charged particles. The heat of reaction is  $\epsilon_{ij}$ .  $E$  is the electric field and  $\nu$  is the collision frequency.

The coupling with electrostatics is achieved through Poisson equation:

$$\nabla^2 \Phi = -\nabla \cdot E = \frac{q_c}{\epsilon_0} (N_e - \sum_i N_i) = -\frac{\rho}{\epsilon_0} \quad (2.5)$$

The simulations with solving Eqn. 2.2, 2.3 & 2.4 for each species with the chemistry can be done, but will be numerically dreadful as discussed by Poggie et al. [47]. The further simplifications on the physical model other than the averaging properties

are required to obtain a solution in a reasonable time.

One of the most common simplifications is neglecting the inertia of charged particles which eliminates the left-hand side of the momentum equations (the acceleration terms). However, studies have reported that ion inertia is important particularly at low pressure and non-equilibrium discharges [30, 47, 48]. The way to check the importance of the inertia is to check the magnitudes of the convective accelerations of species with respect to the elastic collision and the electric body force. To neglect the inertia terms, the convective acceleration should be smaller compared to other terms. Also, if the pressure is large ( $\lambda/L \ll 1$ ), Eqn. 2.3 can be simplified into the drift-diffusion form. Drift-diffusion equations are known as a one-moment model. The momentum equation is simplified and reduced to the velocity form including only drift and diffusion component. In Table 2.1, one-moment and two-moment equations are presented with the manner in which they handle the electron temperature.

Table 2.1.

The summary of different moments of Boltzmann equation used in this study.

One Moment Model	$T_e$ Treatment
Drift Diffusion Equation $\frac{\partial n_j}{\partial t} + \frac{\partial \Gamma_j}{\partial x} = S_j$ $\frac{\partial \mathbf{E}}{\partial x} = \rho / \epsilon_0$	Constant $T_e$ $T_e = f(E/N)$ $\frac{\partial}{\partial t} \left[ \frac{3}{2} n_e (T_e - T_n) \right]$
Two Moment Model	
$\frac{\partial n_j}{\partial t} + \frac{\partial \Gamma_j}{\partial x} = S_j$ $\frac{\partial}{\partial t} (m_e n_e \epsilon_e) + \nabla \cdot (m_e n_e \mathbf{v}_e \epsilon_e) = -\nabla \cdot \mathbf{Q}_e - p_e \nabla \cdot \mathbf{v}_e + M_e$ $\frac{\partial \mathbf{E}}{\partial x} = \rho / \epsilon_0$	

### 2.1.3 Hybrid Approach

Hybrid approaches combine different models to achieve distinct purposes. For example, the description of fast electrons can be modeled with a kinetic approach while other particles are calculated through a continuum approach [49]. In such a formulation, ionization terms are calculated with MC, and species are simulated with continuum approach [50].

Hybrid Plasma Equipment Model, HPEM is one of the best known hybrid codes for plasma simulations, which was developed to simulate low pressure and low-temperature plasma reactors by Kushner [51]. As a hybrid model, the HPEM has different structures in which different physical processes are examined in different modules. There are modules for magneto-statics, various external circuits, Monte Carlo simulations for ion/neutral and electron, Boltzmann equation, sputtering, Poisson-electrostatic, electron beam module, etc.

## 2.2 Numerical Modeling

Assumptions for the governing equations for this study can be listed as:

1. The number density of neutral gases are assumed as a constant through the computational domain. Bulk motion of neutrals is neglected.
2. Ions and neutrals species are considered in thermal equilibrium with a temporally and spatially uniform temperature.
3. Magnetohydrodynamic effects are excluded and magnetic fields are not applied to the system.
4. Low pressures are considered, but are assumed high enough to use continuum approaches.
5. Negative ion formation is not considered.

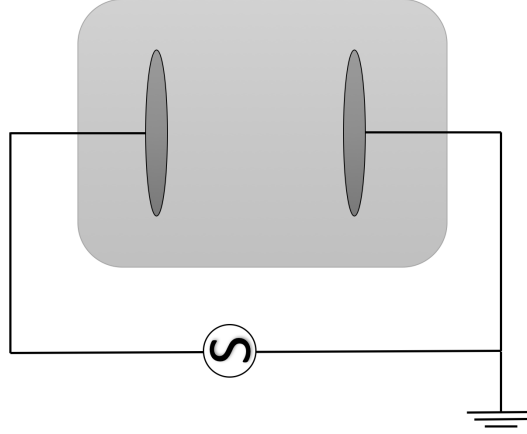


Fig. 2.1. Schematic diagram of electric circuit and discharge chamber.

The basic physics of the glow discharge in between parallel plates, as in Fig. 2.1, in the absence of a magnetic field, is captured with drift- diffusion equation coupled with Gauss's law:

$$\begin{aligned} \frac{\partial n_j}{\partial t} + \frac{\partial \Gamma_j}{\partial x} &= S_j \\ \frac{\partial \mathbf{E}}{\partial x} &= \rho / \epsilon_0 \end{aligned} \quad (2.6)$$

where  $\Gamma$  is the flux of the species considered. The flux includes a drift and diffusion component:

$$\mathbf{\Gamma}_j = s n_j \mu_j \mathbf{E} - D_j \nabla n_j \quad (2.7)$$

where  $s$  is the sign operator:  $+1$  for positively charged particles and  $-1$  for the negatively charged particles. The drift component is scaled with the mobility of the species,  $\mu_j = \frac{q}{m_j \nu_m}$  ( $q$  is the elementary charge,  $m$  is the mass of species, and  $\nu$  is the effective collision frequency for momentum transfer.), and the diffusion component is modeled with diffusion coefficients through the Einstein relation  $D_i = \frac{k_B T_j}{m_j \nu_m} = \frac{k_B T_j \mu_j}{q}$ . These coefficients are obtained with two ways: fitted con-

stants for experiments, as in Table 4.1 & A.2, or fitted values from local field calculations.

The source term calculations are formulated in two ways. In the first approach, constants are fit to data from the experiments to model the production and destruction of species:

$$S_j = \alpha|\Gamma_e| - \beta n_i n_e \quad (2.8)$$

where  $\alpha$  is the Townsend ionization coefficient and  $\beta$  is the recombination coefficient. As mentioned earlier, scaling properties with respect to the pressure, or the neutral number density, is a common and accurate approach. The ionization coefficients can be written as:

$$\alpha/P = A \exp\left(-\frac{B}{|E/P|}\right) \quad (2.9)$$

The constants — A, B and  $\beta$  — for various gases are given in Table A.1.

The second approach is based on finite-rate chemistry calculations. For a given reaction mechanism, the source terms are calculated as follows:

$$\sum_{i=1}^N \nu'_{ri} M_i \rightarrow \sum_{i=1}^N \nu''_{ri} M_i \quad (2.10)$$

$$S_i = \sum_{r=1}^M \left[ (\nu''_{ri} - \nu'_{ri}) k_r \prod_{j=1}^N n_j^{\nu'_{rj}} \right] \quad (2.11)$$

where  $\nu'_{ri}$  and  $\nu''_{ri}$  are the stoichiometric coefficients for species- $i$  in reaction- $r$ ,  $N$  is the total number of species, and  $M$  is the number of reactions. Here  $k_r$  is the reaction rate coefficient for each process. A detailed discussion is presented for reaction rates in the following chapter and in Appendix A.

### 2.2.1 Time and Space Resolution Requirements

Although the resolution studies for each case are provided throughout the study, the base discussion is provided here. Time scales in electric discharges vary enormously depending on discharge conditions: applied voltage, pressure, gas type, and gas temperature. In the first chapter, time scales of physical processes were given. Two additional time scales will be described here which must be resolved to achieve numerically stable solutions.

The dielectric relaxation time characterizes the time required for the electric field to adjust itself to a change in the space charge. It is usually the most restrictive of all the time step limitations for high number density plasma [52]. The dielectric relaxation time is:

$$\tau_d = \frac{\epsilon_0}{q(\mu_i n_i + \mu_e n_e)} \approx \frac{\epsilon_0}{q(\mu_e n_e)} \quad (2.12)$$

The last time limitation arises from the CFL condition. The CFL condition must be satisfied to have stable solutions for partial differential equations.

$$\tau_{CFL} = \frac{\Delta x}{v_e} = \frac{(\Delta x)^2}{2D_e + \mu_e E \Delta x} \quad (2.13)$$

The CFL conditions characterizes the time for an average electron to cross a computational cell.

### 2.2.2 Discretization of Equations

Central difference discretization of the drift-diffusion equation requires very small spacing to be stable; therefore, various more robust numerical discretization schemes have been proposed. Adding damping to a central difference scheme [53], higher order up-winding [54], and logarithmic interpolation of the number densities [55] are some of the methods that have been investigated. One of the most popular approaches is the Scharfetter-Gummel scheme, which is an exponential discretization method that

provides a robust way to discretize the drift-diffusion equation for particle transport [56].

As a numerical approach, finite difference discretization is used. The fluxes are evaluated at the cell interface using the Scharfetter-Gummel scheme. In this scheme, current density, mobility, electric field, and diffusion are considered constant in a computational cell, whereas number densities are not [57]. The overall discretization of Eqn. 2.6 is as follows:

$$\frac{n_{s,i}^{t+1} - n_{s,i}^t}{\Delta t} + \frac{\Gamma_{s,i+1/2}^{t+1} - \Gamma_{s,i-1/2}^{t+1}}{\Delta x} = S_{s,i}^t \quad (2.14)$$

The fluxes at a cell interface can be written as [53]:

$$\begin{aligned} \Gamma_{i+1/2} &= \frac{-s}{\Delta x} \mu_{i+1/2} (\phi_{i+1} - \phi_i) \left[ \frac{n_{i+1}}{1 - \exp(z_{i+1/2})} + \frac{n_i}{1 - \exp(-z_{i+1/2})} \right] \\ z_{i+1/2} &= -s \frac{\mu_{i+1/2}}{D_{i+1/2}} (\phi_{i+1} - \phi_i) \end{aligned} \quad (2.15)$$

It should be noticed that for the highly diffusive limit, this scheme becomes a central difference discretization; whereas, the scheme becomes a first-order upwind scheme for the large drift velocity limit.

The Scharfetter-Gummel scheme also avoids the limitation on the spatial discretization. The differences between voltages of two neighbor cells should not exceed the given limit [56]:

$$\Delta\phi = \frac{2k_b T_e}{q} \quad (2.16)$$

Fig. 2.2 shows the sample result for hydrogen simulation at 3 Torr. Since the simulation was completed with constant electron temperature,  $T_e = 1eV$ , the limit is uniform across the domain.  $\Delta\phi$  exceeds the limit at the cathode sheath; the Scharfetter- Gummel scheme helps to overcome this challenge.

Fig. 2.2 shows the voltage differences on two neighbor cells which are close to the limitation; Scharfetter- Gummel scheme is capable to overcome the limit when

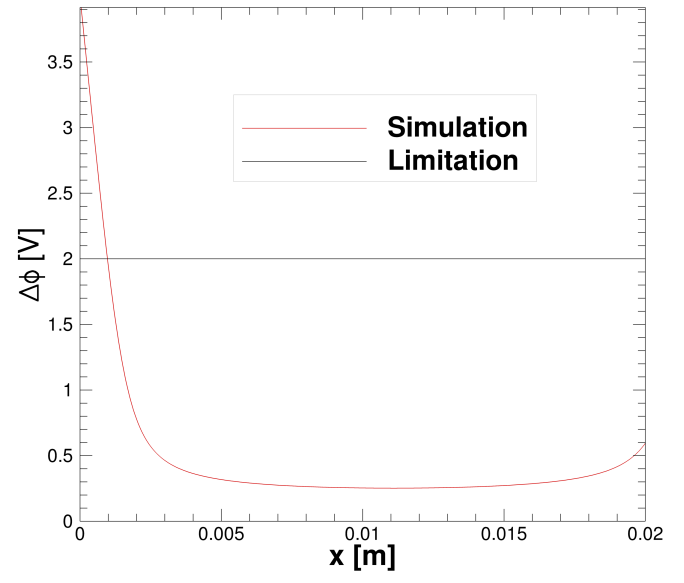


Fig. 2.2. The comparison of  $\Delta\phi$  and  $\frac{2k_b T_e}{q}$  from simulations of  $H_2$  at 3 Torr pressure with 2 cm gap distance for constant  $T_e$ .

$\Delta\phi \approx 700V$ . Central difference and up-winding schemes are subject to the limit given in Eqn. 2.16.

### 2.2.3 Semi-Implicit Implementation of Poisson Equation

As mentioned earlier, dielectric relaxation time scale is usually the most restrictive time scale. To overcome the imposed dielectric time scale limit, Poisson's equation can be arranged to estimate the space charge at the next time iteration by using the current time iteration and its derivatives. A first-order approximation in time is:

$$\frac{\partial^2 \phi^{n+1}}{\partial x^2} = -\frac{1}{\epsilon_0} \left[ \rho^n + \Delta t \frac{\partial \rho^n}{\partial t} \right] \quad (2.17)$$

From the drift- diffusion equations, the time derivative of the space charge density can be obtained by summing over the ion species, and including the result in the previous equation:

$$\frac{\partial \rho}{\partial t} = q \left[ \frac{\partial}{\partial x} \left[ - \sum_p \left( n_p \mu_p \frac{\partial \phi}{\partial x} - D_p \nabla n_p \right) \right] - \frac{\partial}{\partial x} \left[ n_e \mu_e \frac{\partial \phi}{\partial x} - D_e \nabla n_e \right] \right] \quad (2.18)$$

Computing the potential at the next time iteration will yield the final formulation as:

$$\begin{aligned} & \left[ 1 + \frac{q \Delta t}{\epsilon_0} (n_e \mu_e - n_i \mu_i) \right] \frac{\partial^2 \phi^{n+1}}{\partial x^2} + \left[ \frac{q \Delta t}{\epsilon_0} \left( \frac{\partial n_e}{\partial x} \mu_e - \frac{\partial n_i}{\partial x} \mu_i \right) \right] \frac{\partial \phi^{n+1}}{\partial x} \\ & = -\frac{\rho^n}{\epsilon_0} - \frac{q \Delta t}{\epsilon_0} \sum_j s \left[ \nabla D_j \nabla n_j + \nabla^2 n_j \right] \end{aligned} \quad (2.19)$$

The semi-implicit implementation of Poisson's equation will allow the dielectric time limitation to be exceeded by factors of  $10^2 - 10^3$  [52]. Ventzek et al. stated that  $\tau_d \leq \Delta t \leq \tau_{CFL}$  for high density and low pressure discharges [52].

#### 2.2.4 Electron Energy Equation Discretization

The discretization of the thermal electron energy equation is achieved term by term as follows:

Time discretization is a first-order Euler formulation:

$$\partial t(m_e n_e \epsilon_e) = \frac{(m_e n_e \epsilon_e)^{n+1} - (m_e n_e \epsilon_e)^n}{\Delta t}$$

The flux is discretized with a second order up-wind method:

$$\partial x(m_e n_e \mathbf{v}_e \epsilon_e) = \partial x(A m_e n_e \epsilon_e) = \partial x(AU) = \partial(F)$$

Here  $A$  is the flux Jacobian.

$$\partial x(AU) = \frac{(AU)_{i+1/2} - (AU)_{i-1/2}}{\Delta x} = \frac{(A_{i-1}^n + |A_{i-1}^n|)U_{i-1}^{n+1} - 2|A_i^n| + (A_{i+1}^n - |A_{i+1}^n|)U_{i+1}^{n+1}}{2\Delta x}$$

where  $A$  is the velocity of electrons. The heat flux and compression work terms are:

$$-\nabla \cdot \mathbf{Q}_e = -\nabla \cdot \left( -\frac{5}{2} n_e D_e \nabla (T_E) \right) = \partial x(2.5 n_e D_e \partial x(T_E))$$

$$-p_e \nabla \cdot \mathbf{v}_e = -n_e T_E \partial x(\mathbf{v}_n + \mu_e \partial x(\phi) - \frac{D_e}{n_e} \partial x(n_e))$$

Discretization of terms in the heat flux and pressure term is obtained as follows:

$$\partial x(K \partial x(M)) = \frac{(K_i + K_{i+1})(M_{i+1} - M_i) - (K_i + K_{i-1})(M_i - M_{i-1})}{2\Delta x^2}$$

The electron compression work term was neglected because of the issues on the stability of the solver. A flow chart of the code is given in Fig. 2.3.

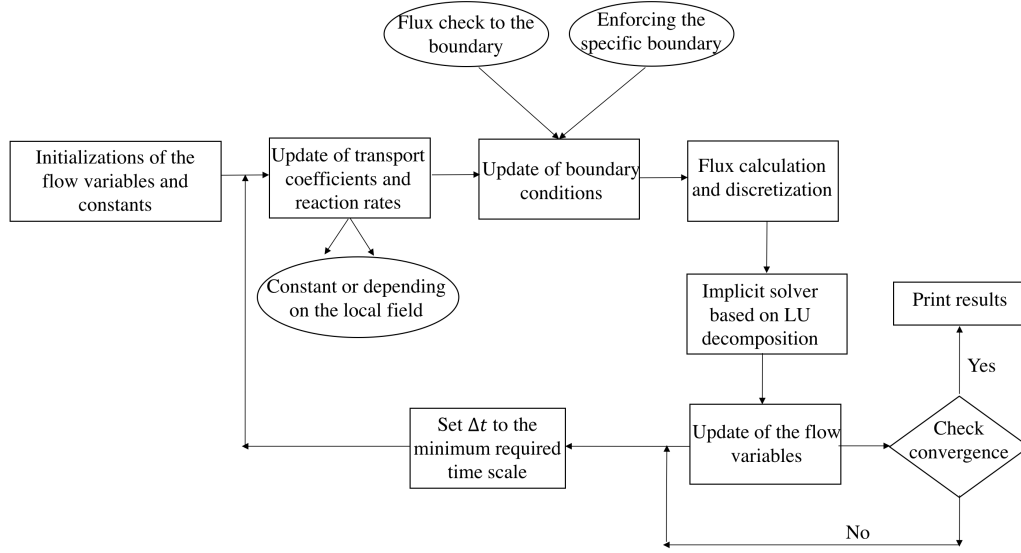


Fig. 2.3. The flow chart of the code.

## 2.2.5 Boundary Conditions

Fig. 2.1 presents a schematic diagram of the system under considerations; the anode is grounded while the cathode has a negative voltage value. The voltage drop at the cathode is calculated with the boundary conditions given in Eqn. (2.20). The positive ions are assumed to be absorbed in the cathode surface and fully reflected from the anode surface. The electron flux from the cathode is generated through secondary electron emission from the cathode as  $\Gamma_e = -\gamma \times \Gamma_i$  [6]. Electrons are assumed to be absorbed in the anode.

A summary of the boundary conditions is:

$$\begin{array}{ll}
 \text{Cathode :} & \text{Anode :} \\
 (V)^{n+1} = V_{dc} - I^n R & V^{n+1} = 0. \\
 (n_e)_i^{n+1} = \gamma \left( \frac{1}{\mu_e} \right)_{i+1}^n \times \sum_i (\mu_i n_i)_{i+1}^n & (n_e)_i^{n+1} = (n_e)_{i-1}^n \\
 (n_i)_i^{n+1} = (n_i)_{i+1}^n & (n_i)_i^{n+1} = 0.
 \end{array} \tag{2.20}$$

Eqn. 2.20 presents a set of simplified boundary conditions where electron diffusion is neglected. Although these simple models help to calculate the boundary conditions easily, the diffusion component of the fluxes and thermal fluxes can be important to capture the boundary properties correctly. In most studies, the boundary conditions are implemented with the drift component and the thermal fluxes [24]. Hagelaar and et al. [58] shows that neglecting diffusion component can cause the higher secondary emission of electrons.

The total current is calculated at the powered electrode, which is a cathode in the current study. With the inclusion of displacement and conduction current, total current can be written as:

$$I = - \int \int \vec{j} \cdot \hat{n} dA = - \int \int \left[ q_c \left( \sum \vec{\Gamma}^+ - \vec{\Gamma}^- \right) + \epsilon_0 \frac{\partial \vec{E}}{\partial t} \right] \cdot \hat{n} dA \tag{2.21}$$

where  $\vec{j}$  is the current density,  $\Gamma$  is the flux of species. The charge conservation equation is:

$$\nabla \cdot \vec{J}_{cond} + \frac{\partial \rho}{\partial t} = 0 \tag{2.22}$$

The displacement current is obtained from the rate of change of the electric field. For an unsteady problems, the displacement current is often the dominant component of the total current.

$$\vec{J}_{dis} = \epsilon_0 \frac{\partial \vec{E}}{\partial t} \tag{2.23}$$

The discretization of the displacement current is carried out with second-order accurate discretization in time by storing the values of the electric field from previous time steps.

### 2.2.6 Cubic Spline Method

The cubic spline method is a popular numerical approach to interpolate values in between data points for a given data set. The cubic spline method is used for two purposes in this study: to resolve in between the experimental data points and to obtain the transport coefficients from the tables for a given local E/N or  $T_e$ . A brief description of the spline used in this study is provided here and the discussions of the numerical results are presented in the next chapter. For tabulated data, such as time vs. experimental voltage, and E/N vs.  $\mu_e$ : the general representation is:

$$x_i \quad \text{and} \quad f(x_i) \quad \text{where} \quad i = 1, \dots, N \quad (2.24)$$

The functional form between each data points,  $x_i$  and  $x_{i+1}$  is assumed to follow a third order polynomial:

$$S_i(x_i) = C_1 + C_2 x_i + C_3 x_i^2 + C_4 x_i^3 \quad (2.25)$$

where  $C_{i=1-4}$  are the constants for the polynomial and  $S_i$  are pieces of the continuous function S:

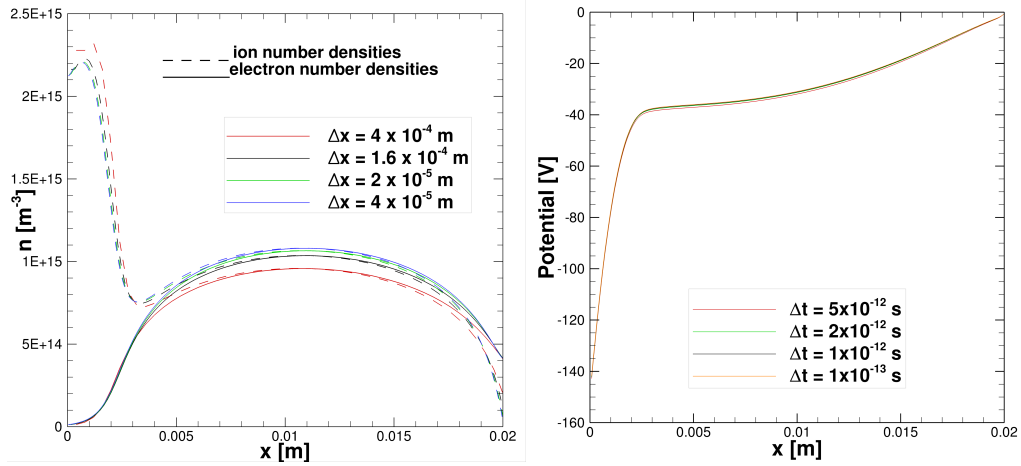
$$S(x) = \begin{cases} S_1, & x_0 \leq x \leq x_1 \\ \vdots & \vdots \\ S_i, & x_{i-1} \leq x \leq x_i \\ \vdots & \vdots \\ S_N, & x_{N-1} \leq x \leq x_N \end{cases} \quad (2.26)$$

The goal is to obtain the coefficients for each spline and the value of the functions for a desired x value which is in between two given data points. Derivatives of splines are calculated to solve for the coefficients. Since there are N points and the N-2 boundaries in the whole interval, additional boundary conditions are required. Spline methods can be distinguished based on the definition of the last two boundary

conditions. In this study, the natural cubic spline method is used, in which two additional boundary conditions are determined by setting  $f_1'' = 0$  and  $f_N'' = 0$

### 2.3 1 D Glow Discharge Calculations

Fig. 2.4 shows the results of the mesh refinement and temporal resolution study. Stable solutions are obtained for 50-500 points across the domain. The reason for having an acceptable solution for a relatively coarse grid is the use of the Scharfetter-Gummel scheme [30]. However, a coarse grid tends to cause the solution to over predict the number densities at the cathode sheath and to under predict at the positive column, Fig. 2.4(a). The temporal convergence was checked with various time steps, and it was observed that high temporal resolution ( $\Delta t < 5 \times 10^{-12}$ ) provides convergence for 500 points across the domain. It should be noted that higher time steps cannot be used because of the CFL limitations, Eqn. 2.13.



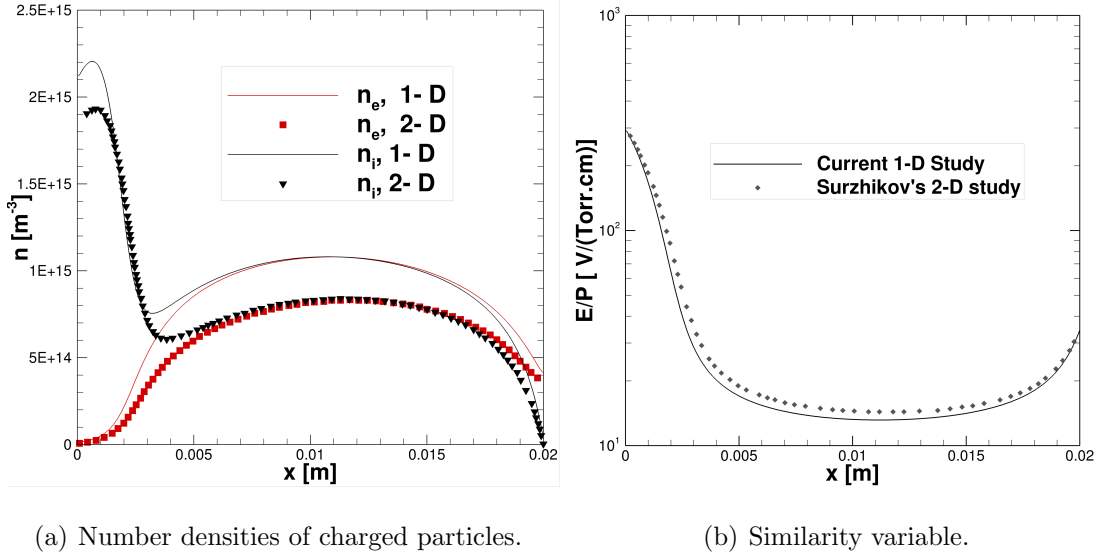
(a) Spatial resolution.

(b) Temporal resolution.

Fig. 2.4. Resolution study for  $H_2$  at  $t = 5 \times 10^{-3}$  s,  $V = 1$  kV,  $P = 3$  Torr,  $\gamma = 0.33$ ,  $R = 300$  k $\Omega$ .

The numerical algorithm was checked against the study of Surzhikov and Shang [59] in which an upwind finite difference scheme was used. The basic differences

arise from the modifications of the conventional code to eliminate limitations on the spatial and time discretization, and the fact that Surzhikov's calculation was 2D. By having the same initial conditions and boundary conditions, simulations show good agreement as in Fig. 2.5. Slight differences are obtained because of different discretization schemes and the two-dimensionality of Surzhikov's model. The cross-sectional area was chosen as  $A = \pi \times (R/2)^2$  where  $R = 4 \text{ cm}$ .



(a) Number densities of charged particles.

(b) Similarity variable.

Fig. 2.5. Comparisons of 1D simulations with Surzhikov and Shang's 2D simulation results [59] for  $H_2$ ,  $R = 300 \text{ k}\Omega$ ,  $P = 3 \text{ Torr}$ ,  $\gamma = 0.33$ ,  $V = 1 \text{ kV}$ .

Paschen conducted experiments to show that breakdown voltage is a function of the parameter  $pd$  and the type of gas [8]. Simulations were completed for different pressure and distance values but with the same  $pd$  value to observe the scaling with the similarity variable. The scaling with the same  $pd$  value should give the same cathode voltage fall as in Fig. 2.6.

Fig. 2.7 shows the effect of the pressure on the cathode sheath. The voltage falls at the cathode are higher for higher pressure values, Fig. 2.7(a). The cathode sheath thickness decreases with increasing pressure, and number densities reach higher values

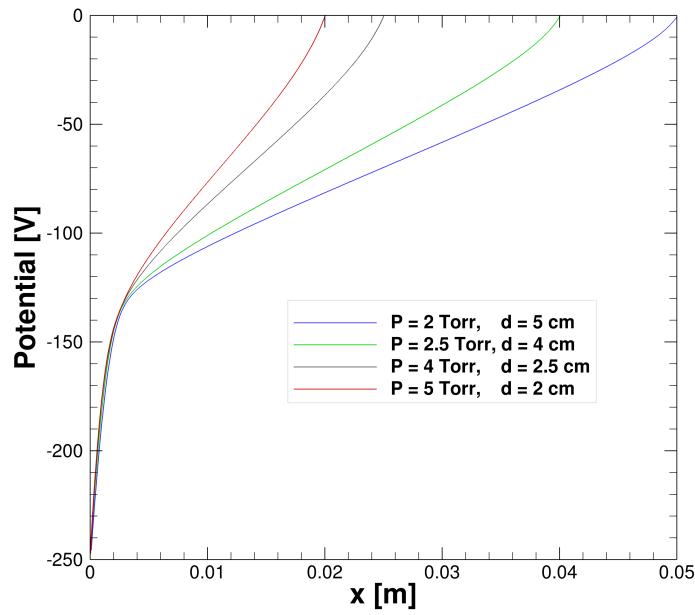
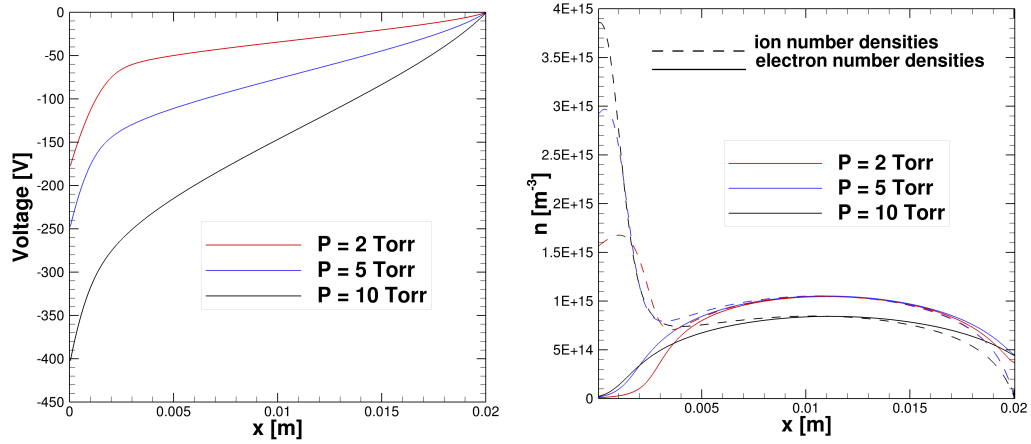


Fig. 2.6. Similarity verification (the same voltage fall and the same cathode sheath thickness) with the same  $pd$  for  $H_2$ ,  $t = 5 \times 10^{-3}s$ ,  $P = 3 Torr$ ,  $\gamma = 0.33$ ,  $R = 300 k\Omega$ ,  $V = 1 kV$

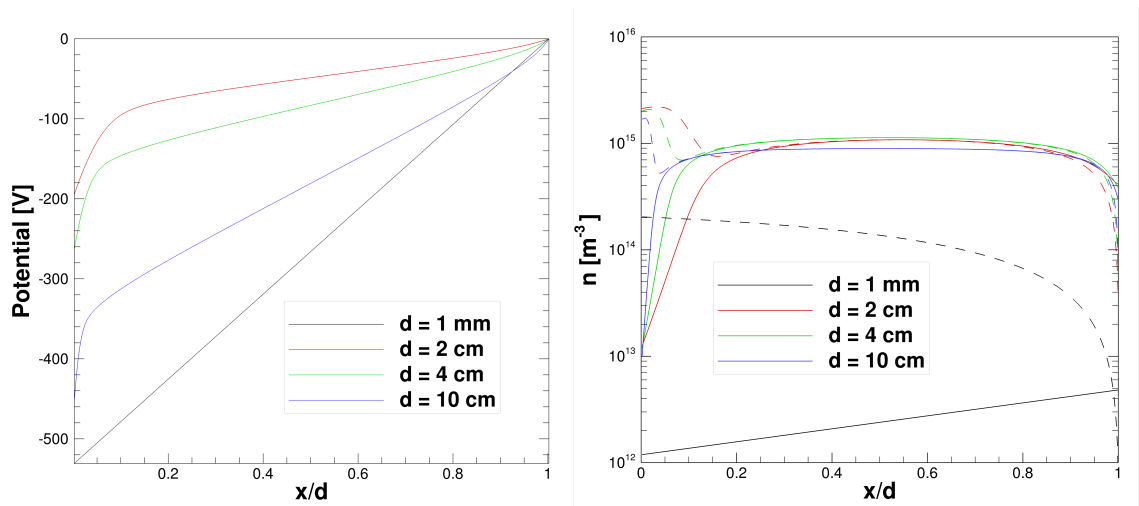
at the cathode sheath, Fig. 2.7(b), whereas number densities are lower in the positive column.

The effects of variation in distance with pressure held constant can be seen in Fig. 2.8. It is expected that the cathode structure remains the same while the positive column expands or shrinks [5]. The cathode sheath thickness is the same,  $d_{sheath} \approx 2$  mm for 2, 5, and 10 cm gap distances, Fig. 2.8(a). Moreover, the number densities are the same; however, they extend spatially with the increment with the distance, Fig. 2.8(b). The results for  $d = 1$  mm represent the dark discharge regime. Altering the distance has resulted in the adjustment in the positive column thickness. Since  $d = 1$  mm  $<$   $d_{sheath} \approx 2$  mm, electrons will not be able to produce enough electrons through the electron avalanche process (shown in Fig. 1.3(a) & 1.2). The transition from dark discharge to glow discharge does not occur; potential across the domain remains undistorted, Fig. 2.8(a).



(a) Effects of pressure on voltage profile. (b) Number density variations for different pressures.

Fig. 2.7. Glow discharge simulation of various pressure for  $H_2$ ,  $t = 5 \times 10^{-3} s$ ,  $\gamma = 0.33$ ,  $R = 300 k\Omega$ ,  $d = 2cm$ ,  $V = 1 kV$ .



(a) Voltage variation

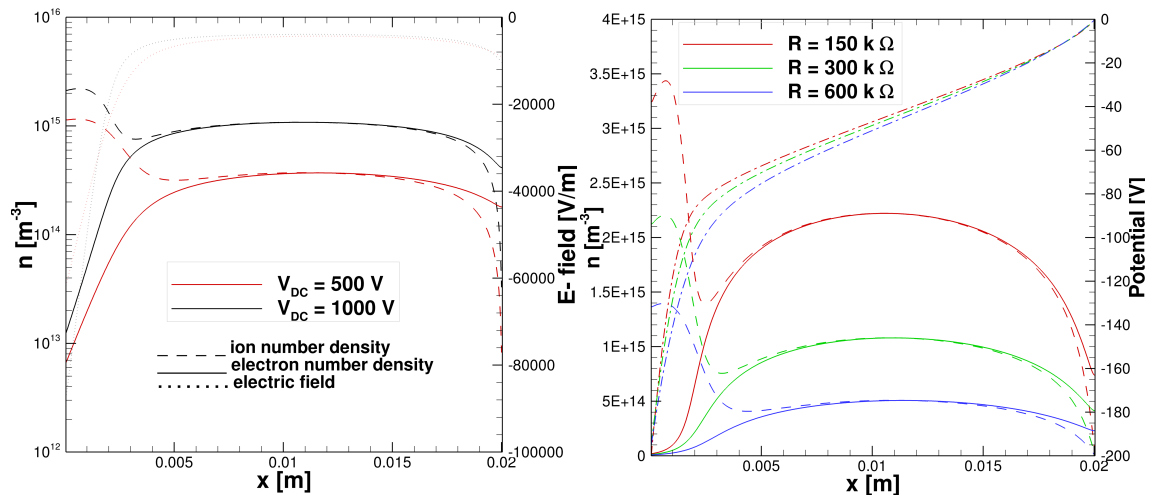
(b) Number densities

Fig. 2.8. Glow discharge simulation of various distance for  $H_2$ ,  $t = 5 \times 10^{-3} s$ ,  $\gamma = 0.33$ ,  $R = 300 k\Omega$ ,  $P = 3 Torr$ ,  $V = 1 kV$ .

Additional simulations are examined to show the robustness of the code. Fig. 2.9 shows the simulations with different applied voltages and different resistance values.

As in the previous chapter, glow discharge domain in the current-voltage graph, region d-e in Fig. 1.2, is a flat region in which current density is increasing with an almost constant voltage. If the applied voltage increased (without changing any other conditions), it is expected to have the same cathode fall if the load lines still cross the glow discharge region as represented in Fig. 1.2. Shifting voltage and resistance might cause a change in the corresponding solution in which load lines can cross the transition regimes, which are unstable.

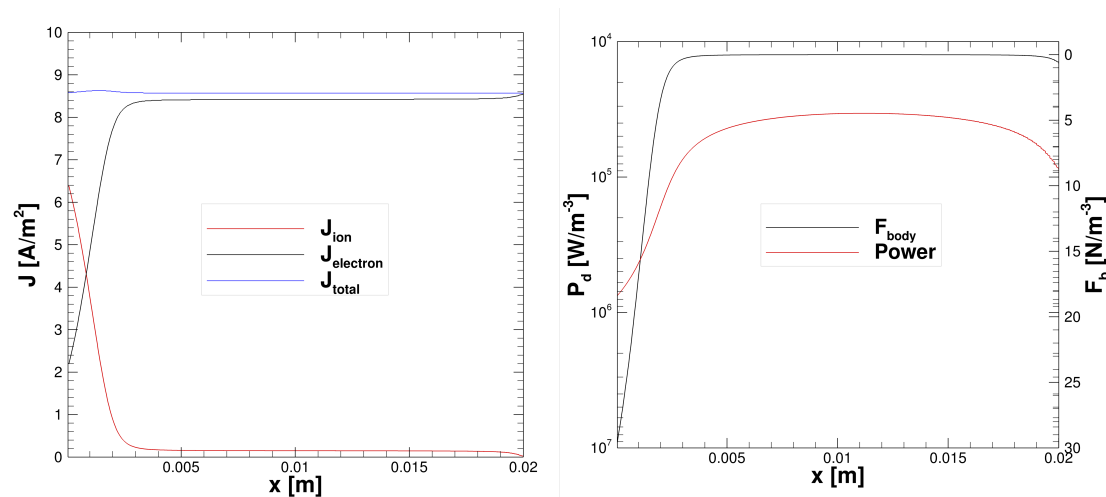
Fig. 2.9(a) shows that, when the applied voltage is doubled, the sheath becomes stronger and thinner, with higher number densities over the whole domain. The current in plasma is increased when the voltage is increased while resistance is kept constant. In a similar manner, lessening resistances at a constant voltage will cause an increase in the plasma current. Thus, similar effects are observed for the reduction of resistance, Fig. 2.9(b) as in the increase of voltage.



(a) Different applied voltage with the same resistance. (b) Different resistance with the same applied voltage where (— electrons, - - - ions and - . - . - potential).

Fig. 2.9. Computed number density, electric field, and potential across the domain for various conditions for  $H_2$ ,  $t = 5 \times 10^{-3}$  s,  $P = 3$  Torr,  $\gamma = 0.33$ ,  $R = 300$  k $\Omega$ ,  $V = 1$  kV.

The current density for electrons and ions are given in Fig. 2.10(a). The total current density is constant. To achieve constant current density, drift, diffusion, and displacement components should be considered together. However, the displacement current component should be negligible for a DC glow discharge problem since it has a steady nature. The body force and power dissipation variations are shown in Fig. 2.10(b). The number densities of an electron in the cathode sheath are considerably lower than the ion number density due to differences between mobilities. Therefore, conductivity will be low at the cathode sheath. Cathode voltage will drop to accommodate the current, and this will result in more heat dissipation in the cathode sheath. Fig. 2.10 is an important simulation result for flow control applications if plasma and flow solver are coupled loosely through the source terms. The body force and deposited power can be estimated from detailed plasma simulations to capture the effects of plasma actuators effects in fluid dynamic calculations.



(a) Current density.

(b) Power dissipation and body force.

Fig. 2.10. Glow discharge simulation results for  $H_2$ ,  $R = 300 \text{ k}\Omega$ ,  $P = 3 \text{ Torr}$ ,  $\gamma = 0.1$ ,  $V = 1 \text{ kV}$ .

## 2.4 Summary

An important question to ask is the feasibility of simulations for the dimensional properties of discharges such as normal current density, and pd scaling. Glow discharges are also at least 2-D because of the current coverage area on the cathode surface.

In this chapter, the fundamentals of physical models were described according to the requirement of capturing the relevant physics. In the discussion of numerical methods, the drift-diffusion equation was described and the discretization approaches were given.

The last part of the chapter was dedicated to showing the capability of the 1D solver. It is observed that 1D codes are able to simulate different discharge properties such as pd scaling, and effect of pressure, distance, and an external circuit. All the results obtained here describe discharges correctly in terms of physics. Also, the cross-sectional area is chosen as the area of the current column from two dimensional study. This cross-sectional area helps to capture the normal current density with one-dimensional solver. Although the number of simplifications is large compared to kinetic models and multi-dimensional calculations, simplified models can capture the required information with lower simulation cost.

### 3. THE LOCAL FIELD APPROXIMATION

In this chapter, a detailed approach is outlined for the use of the local field approximation, in terms of definition and reasons to choose the LFA. The calculations with Bolsig+ to tabulate the transport and rate coefficients with respect to local fields are described. The coefficients calculated from Bolsig+ are compared and validated with experimental data. The calculations are presented with Maxwellian and non-Maxwellian electron energy distribution functions, EEDF, and the differences in the calculations are pointed out. Bolsig+ has different input parameters, and these input parameters are investigated to observe their effects on the computed coefficients. The main discussion focuses on argon gas discharges. Different percentages of water gas are added to analyze the changes.

#### 3.1 The LFA

One-moment and two-moment models were described in the previous chapter, and example simulations were provided for a one-moment model with constant electron temperature. The next step from the one-moment model is to solve the electron energy equation. It is shown that even for 1-D and one-moment simulations, computational requirements are large. Solving the electron energy equation coupled with the drift-diffusion and Poisson equations is not a straightforward step, and there are different ways to integrate the electron temperature into the simulations with simplifications of the physics. One of the methods is to relate  $T_e$  with  $E/N$  or  $E/P$  experimentally [60, 61]. Modeling electron temperature with experimental data is a great simplification. It is, however, crude for most situations because of the specific conditions in which the experiment is conducted. This simplification is not common across the discharge simulation groups.

Significant additional simplification is achieved by using the local field approximation (LFA) instead of solving the full electron energy equation in a fluid model. Again, the electron temperature is dependent on the local fields in which electrons collide frequently. Electron energy diffusion and collisional effects become more important than the motion of the electrons because of the high frequency of collisions. For the local field approximations, the inhomogeneities across the spatial scales are neglected. Electron temperature and transport coefficients, tabulated with respect to the local electric field, are used in simulations to capture the electron temperature variation in the domain. In the absence of the electron energy equation in the physical model, the LFA is a useful approximation if non-local regions are not dominant. Since this chapter is devoted to the local field approximation, the description and explanations of non-local regions are presented in the following chapter. Even though the LFA provides adequate information on nanosecond-pulse discharges, non-local effects must be carefully examined, especially at low pressures [62–64].

Another approach is based on the same approximations with LFA is the local mean energy approximation, LMEA. The LMEA is used when electron energy conservation equation is solved coupled with the drift-diffusion equation. The LMEA is used to calculate the transport coefficients and reaction rates locally for electron energy conservation in which spatial variations of  $T_e$  are considered.

In this study, BOLSIG+ [40] is used to tabulate the data for electrons. The Boltzmann equation is solved for the electron distribution function. In most of the studies, electrons are assumed to be in thermal equilibrium with a Maxwellian distribution. However, ionization and excitation reactions are mostly involved with the tail of the distribution.

In a cold plasma, a non-thermal plasma, electrons are the primary source of energy transformation. Therefore, it is crucial to have accurate modeling of electron behavior. Therefore, a full LFA model is investigated with Bolsig+, and the improvement over the LFA model is presented step by step by checking with experimental data, in the

next chapter. In this chapter, a detailed analysis and a discussion of results from Bolsig+ solver are given.

### 3.2 Calculations with Bolsig+

Bolsig+ is a well-known tool for cold plasma simulations developed by Hagelaar and Pitchford [40]. It is an open source code [40] to calculate collision rates and electron transport coefficients by solving Boltzmann equation, Eqn. 2.1, for electrons in equilibrium with the local electric field. It assumes that neutral gas density is constant, the gas is in a steady state, and there are no gradients and boundaries. The formulation is based on a uniform electric field and no external magnetic field, with the two term approximation. In the two term approximation [40], the electron energy distribution function can be written as summation of isotropic,  $f_I$  and anisotropic,  $f_{II}$  perturbations:

$$f(\vec{r}', \vec{v}', t) = f_I(\vec{r}', \vec{v}', t) + f_{II}(\vec{r}', \vec{v}', t) \cos(\theta) \quad (3.1)$$

The isotropic part is related with the energy relaxation whereas the anisotropic part is related with the transport of electrons. It is based on the Fourier expansion in time and special harmonics in velocity space. The variables calculated from Bolsig+ for this study are mean electron energy ( $\epsilon_m$ ), electron diffusion coefficient ( $D_e$ ), electron mobility coefficient ( $\mu_e$ ), and reaction rates ( $k$ ).

$$\begin{aligned} \epsilon_m &= \int_0^\infty \epsilon^{3/2} f_0 d\epsilon \\ D_e N &= \frac{\gamma}{3} \int_0^\infty \frac{\epsilon}{\sigma_0} f_0 d\epsilon \\ \mu_e N &= -\frac{\gamma}{3} \int_0^\infty \frac{\epsilon}{\sigma_0} \frac{\partial f_0}{\partial \epsilon} d\epsilon \\ k &= \gamma \int_0^\infty \sigma \epsilon f_0 d\epsilon \end{aligned} \quad (3.2)$$

where  $\gamma = \sqrt{2/m}$  is a constant,  $\sigma_0$  is the momentum cross section, and  $\sigma$  is the cross sections for elastic and inelastic reactions. The elastic collision cross section accounts for the elastic collisions, whereas effective cross sections are the total momentum cross sections.

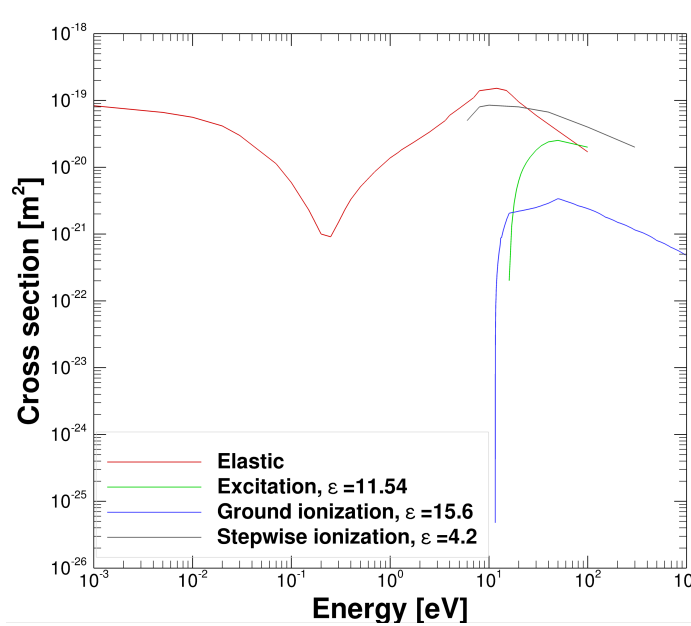


Fig. 3.1. Cross sections for four reactions of argon gas from LxCat website and Trinit database [65].

To run Bolsig+, the required cross sections are obtained from LxCat ([www.lxcatt.net](http://www.lxcatt.net)). LxCat is an open platform to share and to collect data on the cross section of different reactions for various gases. The cross sections for reactions, as in Fig. 3.1, are tabulated with respect to energy; these tabulated data will be the input for Bolsig+ solver. Different simulation parameters are checked before implementing Bolsig+ to make sure that enough information is included in the model.

As mentioned earlier, the LFA is used to calculate the electron temperature locally, instead of solving the electron energy equation with spatial and time derivatives to obtain transport and rate coefficients. Since Bolsig+ is used to tabulate the electron temperature and the local field, validation of Bolsig+ with experimental data is required. This can be seen in Fig.3.2 with respect to experimental studies [66–68].

They estimated electron temperature as  $D_e/\mu_e$  from experiments and the corresponding ratio from Bolsig+ has a good agreement with the experimental data for lower  $E/N$  range. However, there is an obvious discrepancy between two sets; it might be because of the lack of accuracy in the measurements for the high  $E/N$  range. Also, the two-term approach might not be accurate enough to capture the high  $E/N$  range [41, 69]. In this study, the electron temperature is obtained from the mean energy of the electron as  $T_e = 2\varepsilon_e/3$  because mean electron energy governs reaction rates.

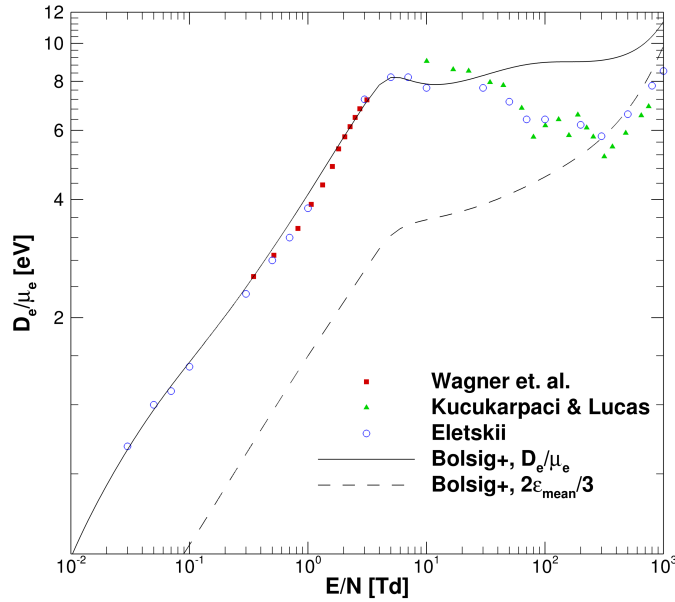


Fig. 3.2. Ratio of electron diffusion coefficients  $D_e$  to electron mobility  $\mu_e$  vs reduced electric field in Argon from the studies of Wagner et.al. [68], Eletsii [66], and Kucukarpaci & Lucas [67] with the mean electron temperature values from Bolsig+ [40].

A second check of the Bolsig+ solver is achieved by comparing reaction rates calculated from the EEDF in different studies, Fig. 3.3. Becker et al. [70] used the Hayashi's cross sections [71] to calculate the reaction rate, while there is no information about cross-section data in the study of Lymberopoulos et al. [72]. The cross-sections that are used for BOLSIG+ calculations are obtained from Trinitite database [65]. How-

ever, the cross-sections are almost the same for the excitation reactions for Trinitite and Hayashi [73] databases. Since there is not enough information about the details of the calculations, the rates are in the expected range except for the excitation reactions. Possible sources of error might include: reading from the graphs (log-log scale) and the possible use of different cross-sections (Hayashi's databases are from different studies and years).

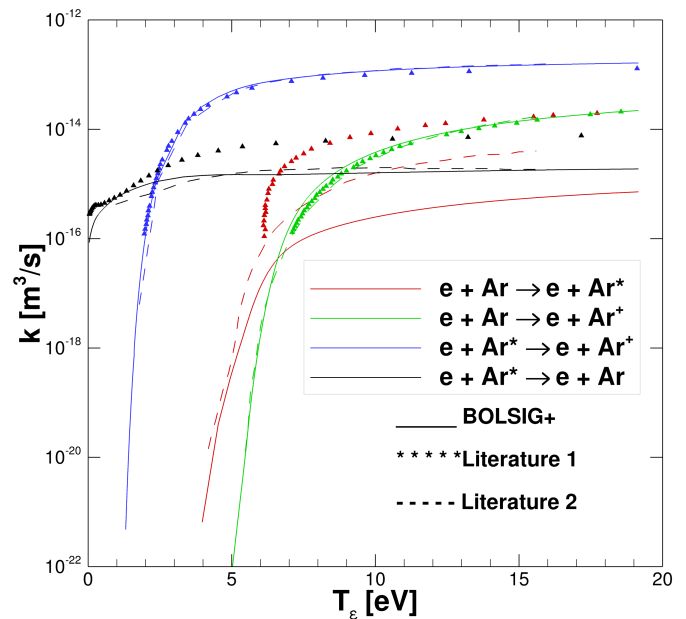
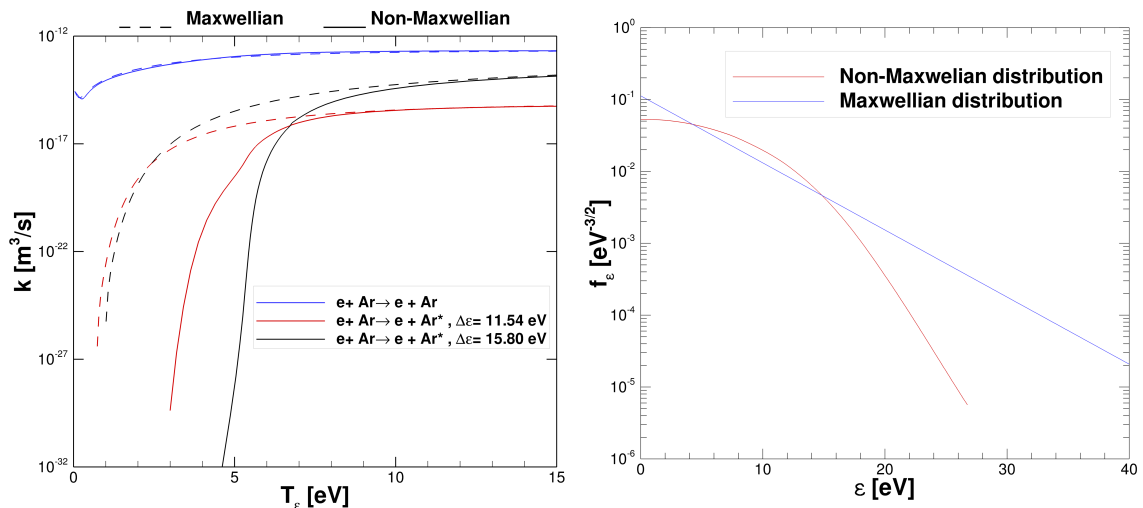


Fig. 3.3. Comparison of reaction rates derived from different solutions of Boltzmann equation for electrons. Literature 1 [70] and Literature 2 [72] are compared with BOLSIG+ results [40, 65].

Significant variations in results are observed for calculations employing the Maxwellian and non-Maxwellian distribution functions, as in Fig. 3.4(a). For lower energy range, the differences in order of magnitude are enormous, almost ten orders of magnitude difference. The electron energy distribution function is plotted for Maxwellian and non-Maxwellian distributions, Fig. 3.4(b).  $E/N$  is chosen as 100 Td to calculate the Maxwellian  $f_e$ , whereas  $T_e$  is around 7 eV for the non-Maxwellian  $f_e$  calculation because the mean electron energy at 100 Td is around 7 eV for the non-Maxwellian distribution. The Maxwellian electron energy distribution function has a linear vari-

ation with respect to the electron mean energy. The non-Maxwellian distribution is shifted from the linear variation and it has larger distribution for high mean energies.



(a) Mean electron temperature vs reduced electric field  
(b) EEDF for Maxwellian and non-Maxwellian distribution at  $E/N$  is 100 Td and  $T_e \sim 6.98$  eV.

Fig. 3.4. Comparisons of Maxwellian and non-Maxwellian EEDF on reaction rates calculated by using Bolsig+ and Trinit database [40, 65].

There are several parameters that can be changed in the input file of Bolsig+. Two of them are e-e collisions and ionization degrees, Fig. 3.6. These calculations are obtained with non-Maxwellian EEDF distributions. With the increment of the ionization degree, the electron mean energy starts to vary at low  $E/N$  ranges. The effects of e-e collisions are negligible if the ionization degree is small; however, slight variation is observed when the ionization degree is  $10^{-6}$ .

Transport coefficients for electrons can be obtained from Bolsig+ and they can be tabulated with respect to local  $E/N$  or electron mean energy. Fig. 3.7 shows the electron diffusion and mobility coefficients for 3 Torr. In accordance with the scaling for weakly ionized gas, Bolsig+ produces result as diffusion coefficient times neutral number densities  $DN$  [1/m.s] and mobility times neutrals' number density

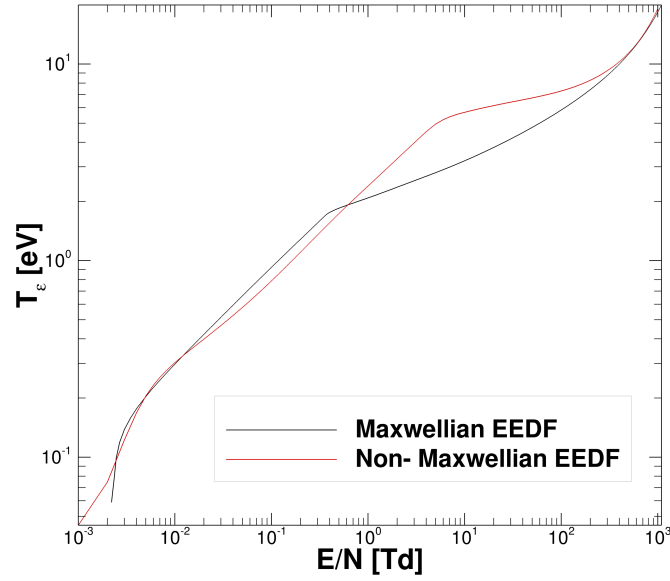


Fig. 3.5. Comparisons of the effects of Maxwellian and non-Maxwellian distribution of EEDF for pure argon [40, 65].

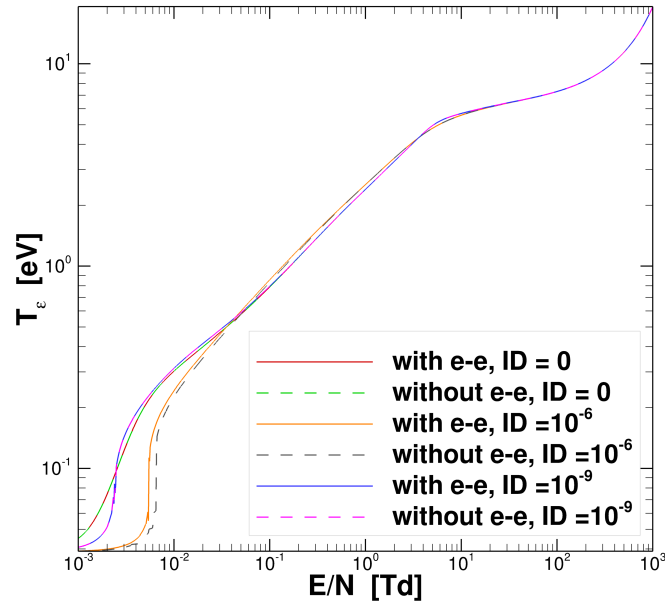


Fig. 3.6. Effects of the ionization degree and e-e collisions on the  $E/N$  vs  $T_e$  for pure argon. Cross-sections are from Trinit database [65].

$\mu N$  [1/m.V.s]. The tabulation of data or curve fitting thus needs to be done only once and the data can be used for different pressures.

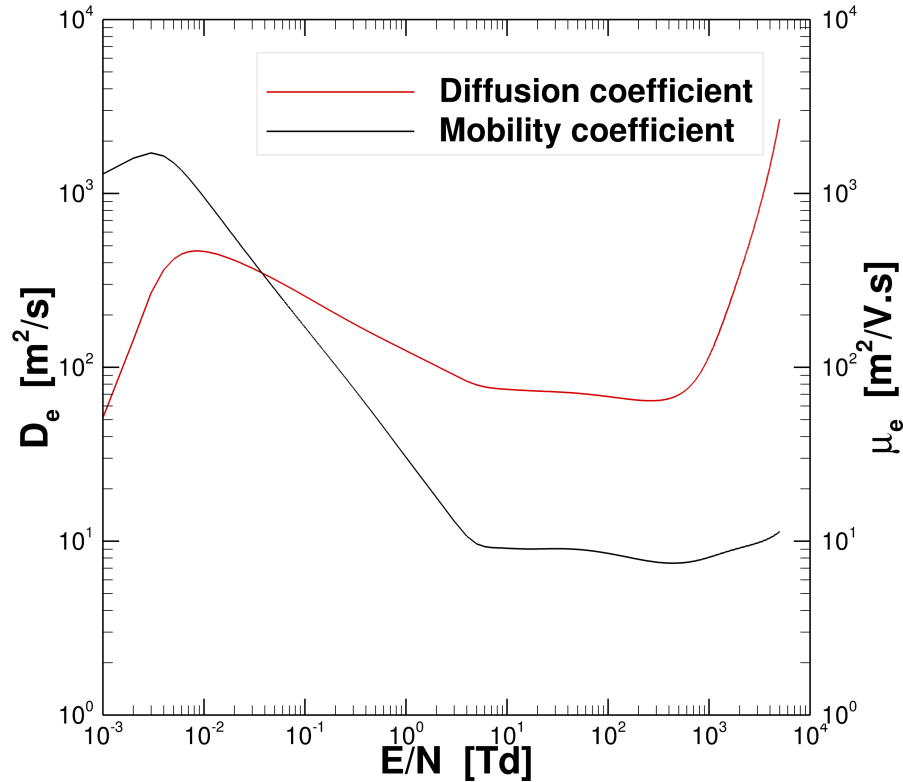


Fig. 3.7. Electron mobility and diffusion coefficients from Bolsig+ [40] and Trinitite database [65] for 3 Torr pressure.

Another important phenomenon that appears in the low  $E/N$  range is the Ramsauer effect, which is clear in the transport coefficient plots, Fig. 3.7. Although a decrease in the scattering cross-section is expected with a decrease in electron energy, quantum mechanical resonant scattering of electrons creates a certain electron energy where scattering is maximum. This effect is known as the Ramsauer effect. This effect [5] causes the increase in transport coefficients at low  $E/N$  values for pure argon calculations and all noble gases. The increment in the transport coefficients of an electron will affect the computational requirement by altering the CFL and dielectric relaxation time scales; the value of the electron mobility coefficient

is  $\sim 10$  [ $\text{m}^2/\text{V.s}$ ] for high  $E/N$  values. The mobility of electron at  $E/N \sim 0.01$  is, however,  $\sim 2000$  [ $\text{m}^2/\text{V.s}$ ].

Adding molecular gases to noble gases will alter the chemistry and the flow behavior. Here, water vapor is added to argon gas, and the differences in the transport coefficients are presented. The effects of water molecules are examined for low percentages of water vapor, Fig. 3.8. For argon, electron temperatures have considerably higher values for the low  $E/N$  range. With an increment of the amount of water vapor percentage, electron temperatures drop to room temperature quickly as electric fields drop,  $\sim 1$  Td.

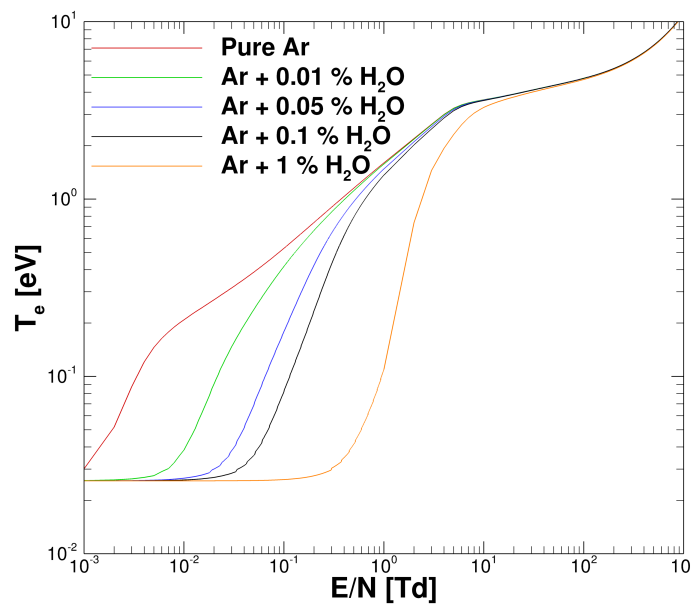


Fig. 3.8. The effects of the water percentage on the  $T_e$  variations with respect to the local  $E/N$ , calculated from BOLSIG+ [40] by using Trinitati database for argon [65], and Itikawa database for water [74].

Mobility and diffusion coefficients are also affected by the existence of water molecules. The peak from the Ramsauer effect diminishes with increase in the water percentage, Fig. 3.9. The values of the transport coefficients also decrease with an increment of water vapor percentage for the low  $E/N$  range.

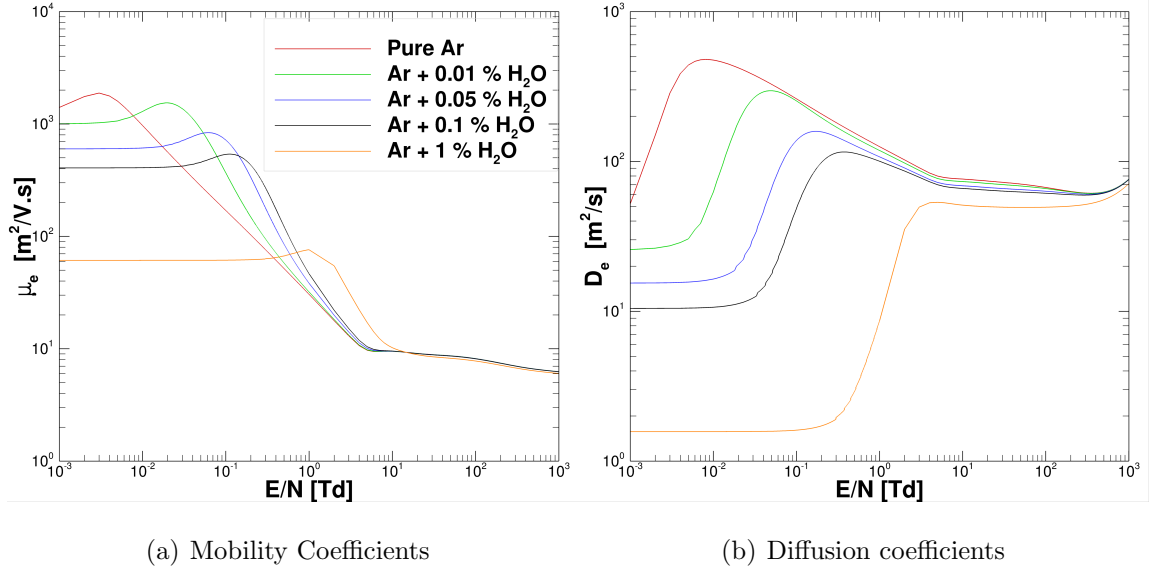


Fig. 3.9. The effects of water amount on the transport properties calculated by using Bolsig+ [40], Trinit database for argon [65], and Itikawa database for water [74].

Collision frequencies of argon for momentum transfer, excitation, and ionization are plotted in Fig. 3.10. Similarly, momentum transfer, rotational ( $\epsilon_{rot} = 0.0046eV$ ), vibrational bending ( $\epsilon_{vib,b} = 0.1977eV$ ), and vibrational stretching ( $\epsilon_{vib,s} = 0.4595eV$ ) collision frequencies are also shown in Fig. 3.10

### 3.3 Zero Dimensional Electron Temperature Solver

A 0-D electron temperature equation solver neglects the spatial and temporal variations in the total electron energy. Only  $\mathbf{j} \cdot \mathbf{E}$  heating and changes from elastic and inelastic processes are considered:

$$\sum_i R_i \Delta H_i + \frac{q n_e}{(m_e + m_N) \mu_e} \left[ -3k_B(T_e - T_N) + m_N(|v_e - v_N|^2) \right] = 0 \quad (3.3)$$

where  $R$  is the rate of production and loss of the electrons,  $\Delta H$  is the heat of reaction.  $m_{e,N}$ ,  $T_{e,N}$ , and  $v_{e,N}$  are mass, temperature, and velocity of electrons or neutrals,

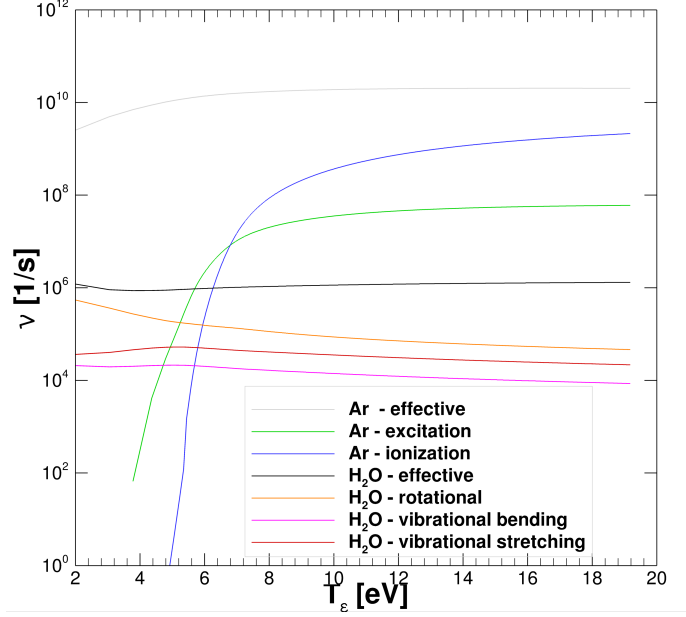


Fig. 3.10. Collision frequencies for different processes of argon and water vapor at 3 Torr. Trinitite database [65] is used for cross-sections of each process.

respectively. Also, it should be noted from the above equation, Eqn.(3.3):  $\frac{qn_e v_e^2}{\mu_e} = qn_e \mu_e E^2 = jE$ . Eqn.(3.3) can be written as:

$$T_e \left( \frac{E}{N} \right) = T_N + \frac{m_N}{3k_B m_e} \left[ \frac{q^2}{m_e k_m^2} \left( \frac{E}{N} \right)^2 - \frac{\sum_i R_i \Delta H_i}{k_m} \right] \quad (3.4)$$

where  $k_m$  is the rate coefficient for momentum transfer.

It should be noted that the diffusion component in current density and electron velocity and neutral velocity are neglected here. In the 0-D model, electron temperature is calculated locally depending only on the local  $E/N$ . The 0-D solver can be verified by solving the system where elastic and inelastic reaction rates are obtained from Bolsig+; it should give nearly the same result as Bolsig+.

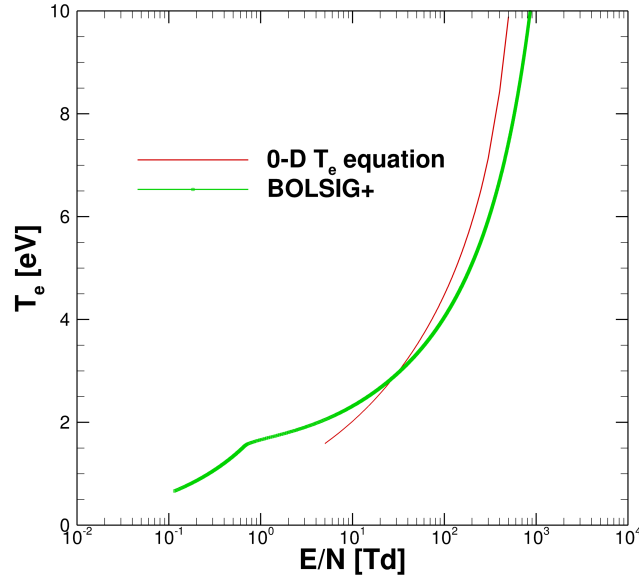
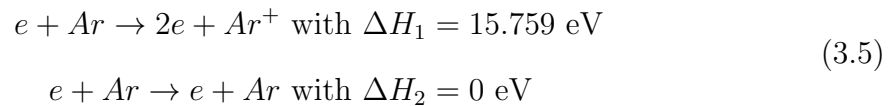


Fig. 3.11. 0-D solver check with BOLSIG+ [40] for E/N vs  $T_e$ .

As a test case, the cross sections of inelastic reaction and elastic reaction are selected from Morgan database [75]:



The 0-D check is calculated for  $5 \leq E/N \leq 500$  as in Fig.3.11. The equation is solved with Newton-Raphson method implicitly and different convergence criteria were investigated. However, it was noticed that there are differences between the solutions, which might be a result of curve-fitting. Data from Bolsig+ are fitted with different functional forms: power, polynomial, exponential, or Gaussian. When the derivatives of terms dependent on  $T_e$  are taken to calculate gradients for Newton-Raphson method, those discrepancies will be amplified. However, it is clear that the order of magnitude and the behaviors are the same.

### 3.4 Summary

By neglecting the spatial inhomogeneities in the boundless plasma, the variables can be defined regarding the local properties. In this chapter, electron temperature, transport and rate coefficients are calculated by using Bolsig+ solver for local E/N values. The Bolsig+ calculations were described, and detailed computations were carried out for different conditions. The comparisons with other computational and experimental studies were carried out; Bolsig+ results have overall good agreement with other studies.

Pure argon chemistry was examined, and Ramsauer effects were observed for low E/N range. The molecular gas, water vapor, was added to the plasma chemistry. The behavior at low E/N range alters with the concentration of the molecular gas; the Ramsauer effects diminishes with the increase in the water vapor.

The effects Maxwellian and non-Maxwellian distribution functions were analyzed on the reaction rates, mean electron energy profile and energy distribution function. The rate coefficients vary significantly for Maxwellian and non-Maxwellian distributions at low E/N or low  $T_e$  range because of the intensified distributions of electrons at high energies for non-Maxwellian distributions.

The Local Field Approximation chapter was designed to present the data that will be used in the following chapters while providing a fundamental discussion of the approach. The result of the Bolsig+ calculations was implemented in the code by curve-fitting the desired value with respect to either local E/N or  $T_e$ .

## 4. SIMULATIONS WITH THE LFA AND IMPROVEMENTS ON THE LFA

**NOTE:** Parts of this chapter are published in the following journal paper:

*Tugba Piskin et al 2019 J. Phys. D: Appl. Phys. 52 304002 [76]*

The transport and rate coefficients, and the correlation between local  $E/N$  and  $T_e$  from Bolsig+ solver were discussed in the previous chapter. In this chapter, the one-moment model is employed with this information. Transport coefficients are used from the Bolsig+ solver for all calculations. Rate coefficients from Bolsig+; however, caused a crash of the code because of the faster ionization. Curve fitted rate coefficients were used instead.

To investigate the usefulness of the LFA, it is used to simulate low-pressure NS pulse discharges while checking requirements of the system carefully. Comparisons with an experimental study are made. The LFA is used in different discharge simulations, and it is compared with non-local simulations, and the results are compared with experimental data. The applicability of Bolsig+ solutions is discussed in the case where gradients and non-local effects are dominant.

### 4.1 Nanosecond Pulsed Discharges

Interest in pulsed discharges has been increasing in aerospace engineering for applications to aerodynamic flow control and combustion enhancement. Nanosecond-pulse discharges have been investigated experimentally to control flow separation [77, 78] because of their fast response and low power requirements. It has also been shown that nanosecond-pulse discharges are efficient in terms of ionization of gases compared to steady discharges [79], and the existence of excited levels, especially metastable

levels, can reduce the delay in the ignition [80] in combustion applications. The stability of NS pulsed discharges are better compared to other discharges because of the elimination of transitions due to on and off voltages. Different pulse lengths and repetition frequencies alter the behavior of discharges.

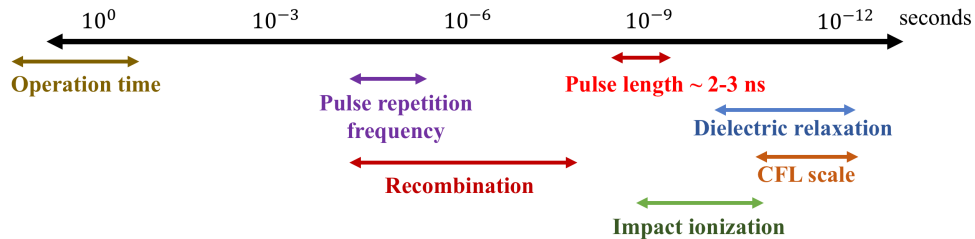


Fig. 4.1. Various time scales for short nanosecond pulse discharges in argon.

The rapid thermalization of nanosecond pulsed plasma narrows the usage of plasma actuator in terms of flow control purposes, on the other hand, thermalization is the main source of the gas heating for plasma actuators. According to application requirements, plasma chemistry should thus be modeled. As mentioned earlier, changing chemistry by adding impurities improves the overall performance of mercury lamps. Accurate modeling of chemistry has gained importance; however, the information on the transport coefficients and chemistry for these highly non-equilibrium systems are deficient.

Successful applications depend on efficient plasma generation; the power budget for plasma generation was evaluated in [81, 82]. In a typical DC or RF discharge where electron temperatures are 1–3 eV, a relatively small fraction of the input energy goes into ionization. Most collisions of electrons with molecules result in inelastic or elastic energy losses. For efficient ionization, a very high mean electron energy of 100–1000 eV is desirable, and such energies can be achieved through injection of high-energy electron beams into a gas. Another approach to the generation of high

electron energies is the use of high-repetition, nanosecond-pulse electrical discharges. In such discharges, the rapid potential change creates sufficiently large electric fields, electron energies, and electron velocities to act effectively as a local electron beam.

Accurate numerical simulation of these discharges remains extremely challenging. The continuing difficulties lie in an enormous separation of space and time scales, a lack of transport and kinetic data, and extreme non-equilibrium physics. The time scales for various processes for short nanosecond pulses are shown in Fig. 4.1. By focusing on a specific experiment carried out under conditions relevant to plasma antenna applications, this study illustrates how numerical calculations can provide useful guidance for ongoing experimental work, despite the difficulty of the simulations.

## 4.2 Simulations of 1-D NS Pulse Discharges

In this section, a specific example of the application of the LFA is presented, along with step by step improvements in the model to advance the agreement between the simulations and the experiment. The experiment was conducted by Prof. Sergey Macheret's group, and the details can be found in the paper [83]. A pulsed discharge with a 3 ns, 850 V pulse and a 30 kHz pulse repetition frequency are was considered. The discharge was created in a plane-to-plane electrode configuration with a 2 cm gap in 3 Torr argon.

The experimental voltage data were applied as an input at one of the electrodes, and another electrode was grounded as shown in the schematic diagram in Fig. 2.1. Since the voltage profile measured experimentally has oscillations and noise (see Fig. 4.4), the powered electrode can switch its polarity between that of cathode and anode during the simulations. Such switching creates stiffness and noise in the calculations, so the experimental data were smoothed to mitigate the noise. Fig. 4.4 shows the voltage profiles obtained in the experiments, along with the smoothed profile employed in the computations. The smoothing coefficient in an iterative Laplace solver was

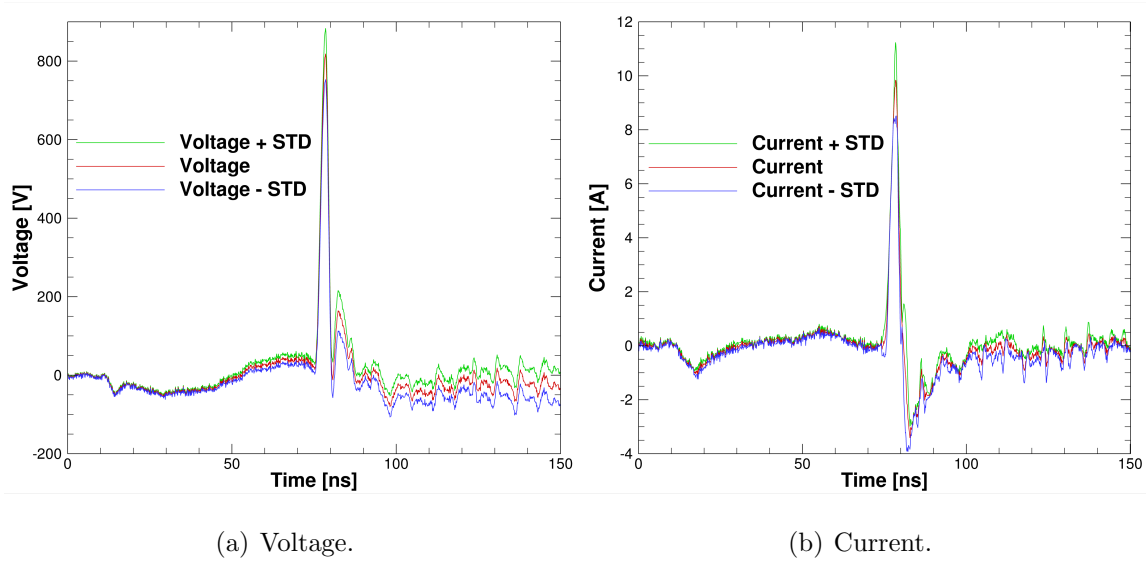


Fig. 4.2. Measured properties of circuit as a function of time. An experimental uncertainty of one standard deviation (STD) is indicated [83].

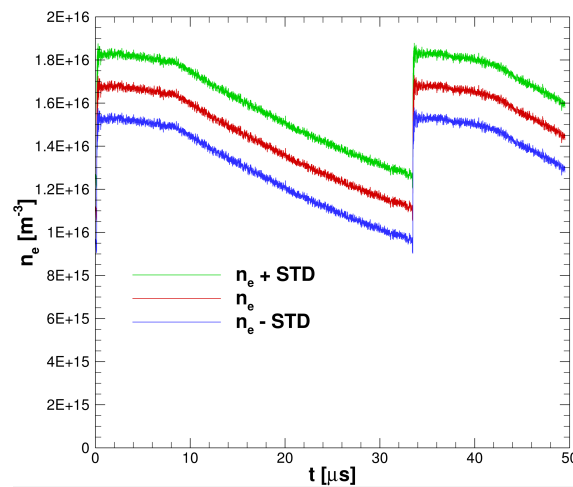


Fig. 4.3. Measurements of spatially-averaged electron number density  $n_e(t)$ . An experimental uncertainty of one standard deviation (STD) is indicated [83].

chosen as 0.005, with 1000 passes, which kept the peak voltage value close to the raw data and removed spikes without altering the basic profile.

Also, in Fig. 4.4, the smoothed data are truncated to decrease numerical stiffness from the boundary conditions. The oscillations after the voltage peak have magnitudes between 60 V and -60 V. These oscillations in the input voltage cause quick shifts on the boundary conditions; this creates numerical challenges. Since they have a large magnitude for pure argon, these oscillations delay the thermalization of argon after the peak voltage is applied. Instead of using the full 150 ns long experimental profile as an input, data corresponding to the restricted range 50 ns - 85 ns are used in the simulations.

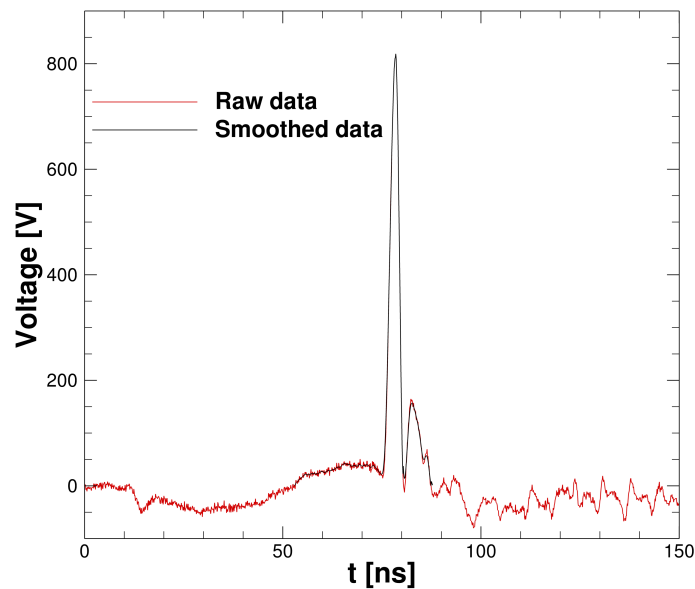


Fig. 4.4. Comparison of raw and smoothed time trace of input voltage.

The last modification of the input voltage is to increase the temporal resolution. The time between the measured data points is 100 ps. Since the required simulation time step during the pulse can be different than that (usually higher resolution is required), intermediate values were obtained using cubic spline interpolation.

Transport coefficients for the species used in the simulations are given in Table 4.1. The electron and ion mobilities are obtained by curve fitting to Fig. 3.2 & 3.9 depending on the simulation conditions. The Ramsauer effect in the lower E/N range

causes an increment of the dielectric relaxation time, Eqn. 2.12, and CFL time scale, Eqn. 2.13. A limit is applied to these coefficients to keep time scales in a reasonable range. Since variations in the mobility were not significant for  $H_2O^+$ ,  $H_3O^+$ , and  $ArH^+$  with respect to  $E/N$  in the referenced studies [84, 85]; these mobilities are considered as constant.

Table 4.1.  
Mobility and Diffusion Coefficients

Species	Mobility [ $m^2/(V.s)$ ]	Diffusion Coef. [ $m^2/s$ ]	Ref.
e	Bolsig+	Bolsig+	[40]
$Ar^+$	$\frac{10^{-1} \times (1 - 2.22 \times 10^{-3} \frac{E}{P})}{P} \quad \frac{E}{P} \leq 60 \left( \frac{V}{cm.Torr} \right)$ $\frac{0.825}{P\sqrt{E/P}} \left( 1 - \frac{86.52}{(E/P)^{3/2}} \right) \quad \frac{E}{P} > 60 \left( \frac{V}{cm.Torr} \right)$	Einstein Relation	[50]
$Ar_2^+$	$1.83 \times 10^{-4} (760/P[Torr])$	Einstein Relation	[86]
$Ar^*$	$\emptyset$	$2.42 \times 10^{19}/N_{Ar} (m^{-3})$	[72, 87]
$H_2O^+$	$2.65 \times 10^{-4}$	Einstein Relation	[84]
$H_3O^+$	$3.00 \times 10^{-4}$	Einstein Relation	[84]
$ArH^+$	$1.70 \times 10^{-4}$	Einstein Relation	[85]

The first set of reactions includes Ar,  $Ar^*$ ,  $Ar^+$ ,  $Ar_2^+$ , and e. The reaction sets are reduced carefully. The excited states of Argon are represented by  $Ar^*$ , where several excited states are collected together to have an effective state. Based on the experimental studies [88, 89] for reaction rates of dissociative recombination of  $Ar_2^+$ , the 4s and 4p levels are lumped in together.

For the simulations of the argon-water mixture, additional reactions are included, as in Table 4.3. The added species are  $H_2O$ ,  $H_2O^+$ ,  $H_3O^+$ , and  $ArH^+$ . The other species in Table 4.3, H,  $H_2$ , and OH are neglected. The different numerical and physical models are summarized in Table 4.4.

The three possible dissociative attachment reactions of electrons with  $H_2O$  have high energy thresholds, 6 eV to 8 eV, and thus low reaction rates when the electron

Table 4.2.  
Reaction Rates for pure Argon

#	Reactions	Rates	Ref.
Electron impact ionization	$e + Ar \rightarrow Ar^+ + 2e$	$k_{b1}, k_1 = 4.0 \times 10^{-18} T_e^{0.5} \exp(-15.8/T_e)$	[40, 90]
Ground state excitation	$e + Ar \rightarrow Ar^* + e$	$k_{b2}, k_2 = 1.0 \times 10^{-17} T_e^{0.75} \exp(-11.6/T_e)$	[40, 91]
Step-wise ionization	$e + Ar^* \rightarrow Ar^+ + 2e$	$k_{b3}, k_3 = 1.0 \times 10^{-16} T_e^3 \exp(-4.16/T_e)$	[40, 91]
Recombination	$e + Ar^* \rightarrow Ar + e$	$k_4 = 1.0 \times 10^{-17} T_e^{0.75}$	[91]
$Ar_2^+$ dissociative recombination	$e + Ar_2^+ \rightarrow Ar^* + Ar$	$k_5 = 5.38 \times 10^{-14} T_e^{-0.66}$	[88, 91]
Recombination	$e + Ar^+ \rightarrow Ar^*$	$k_6 = 4.00 \times 10^{-19} T_e^{-0.5}$	[90, 91]
Three body recombination	$e + e + Ar^+ \rightarrow Ar^* + e$	$k_7 = 5.00 \times 10^{-33} T_e^{-4.5}$	[91]
Atomic to molecular ion conversion	$Ar^+ + 2Ar \rightarrow Ar_2^+ + Ar$	$k_8 = 2.50 \times 10^{-37}$	[90]
Metastable associative ionization	$Ar^* + Ar^* \rightarrow Ar^+ + Ar + e$	$k_9 = 5.0 \times 10^{-16}$	[91]

$T_e$  is in [eV].  $k$  is in [ $m^3/s$ ] except  $k_{7,8}$  which are in [ $m^6/s$ ].

temperature is low [92]. Attachment reactions have only a small influence on the plasma decay between pulses, and therefore the attachment was neglected in the model. The relative importance of quenching of metastables (R8 in Table 4.3) by water molecules was also investigated. This quenching reaction significantly reduced the number density of excited argon atoms, but it has negligible effect on the electron number density and electron temperature decay profiles. Calculations carried out with and without the quenching reaction, Fig. 4.5, show that electron number density remains essentially constant despite a three-order-of-magnitude drop in the number density of excited argon due to quenching.

The reason for adding water vapor into the simulation is that the experimenters suspect that a trace amount of water exists in the discharge chamber. To address the problem clearly, water molecules are also included in the simulations.

In initial simulations, it was observed that pure argon simulations with the LFA do not provide enough thermalization after the pulse, that is, electron temperature remains at high values long after the pulse. Fig. 4.6 shows a test case where uniform

Table 4.3.  
Reaction Rates for Ar- $H_2O$  mixture

#	Reaction	Rates ( $m^{-3}/s$ ) or ( $m^{-6}/s$ )	Ref.
R1	$Ar^+ + H_2O \rightarrow Ar + H_2O^+$	$1.50 \times 10^{-16}$	[93, 94]
R2	$Ar^+ + H_2O \rightarrow ArH^+ + OH$	$1.31 \times 10^{-15}$	[94, 95]
R3	$ArH^+ + H_2O \rightarrow Ar + H_3O^+$	$4.90 \times 10^{-15}$	[92, 94]
R4	$H_2O^+ + H_2O \rightarrow H_3O^+ + OH$	$1.30 \times 10^{-15}$	[94, 95]
R5	$H_3O^+ + e \rightarrow H + H_2O$	$2.50 \times 10^{-14}T_e^{-0.7}$	[92]
R6	$H_3O^+ + e \rightarrow H_2 + OH$	$1.40 \times 10^{-14}T_e^{-0.7}$	[92]
R7	$H_3O^+ + e \rightarrow H + H + OH$	$6.00 \times 10^{-14}T_e^{-0.7}$	[92]
R8	$Ar^* + H_2O \rightarrow Ar + H_2O$	$4.80 \times 10^{-16}$	[96]

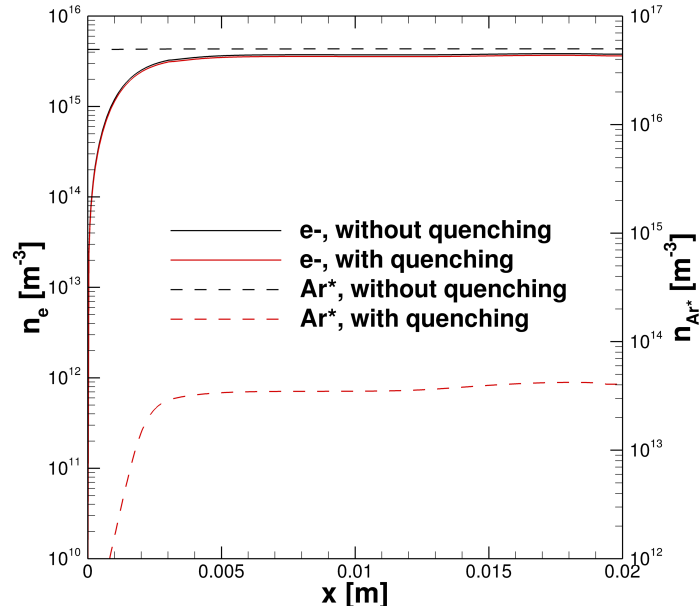


Fig. 4.5. Effects of quenching reaction of  $Ar^*$  with  $H_2O$  ( $\hat{t} = 10 \mu s$ ).

plasma is allowed to decay. In the beginning, there is a short transient of the electron temperature as the uniform initial state accommodates the suddenly applied boundary conditions. The plasma starts to decay around 0.9 ms, and the decay of electron

temperature is very slow. The decay of electron temperature in the pulsed discharge simulations also undergoes this slow relaxation.

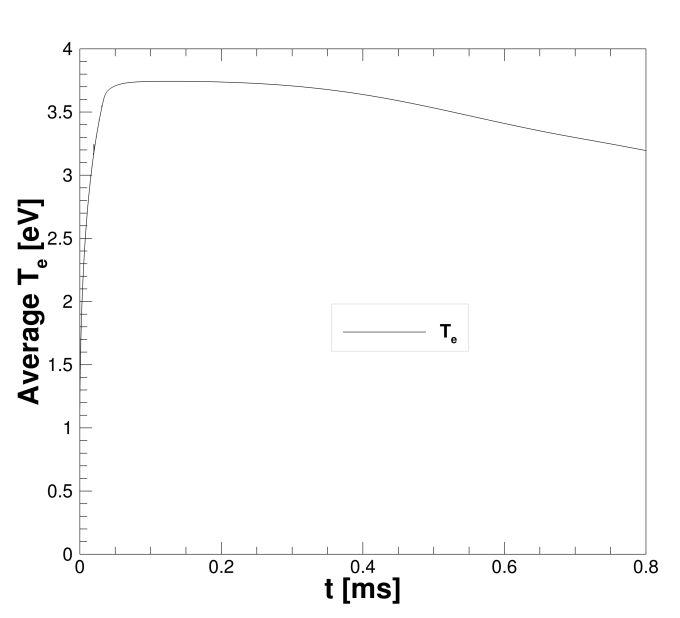


Fig. 4.6. The test case for decay of the pure uniform argon plasma under the LFA.

To investigate the causes of this slow decay, non-local effects were incorporated into the model. Detailed discussion is given in the following chapter. Briefly, LFA is a useful method if the electron energy relaxation length is considerably smaller than the discharge length. Fig. 4.7 shows the relaxation length calculated with the local field approximation for the pulse simulation at the peak voltage. It should be noted that Fig. 4.7 is plotted for a time before the simulation reached a periodic state.

The non-local fields are included by averaging electron temperature over the domain. This change was not sufficient, however, to increase the rate of the thermalization to that observed experimentally. Therefore, an averaged 0-D electron temperature equation is used after the pulse, Eqn. 4.1.

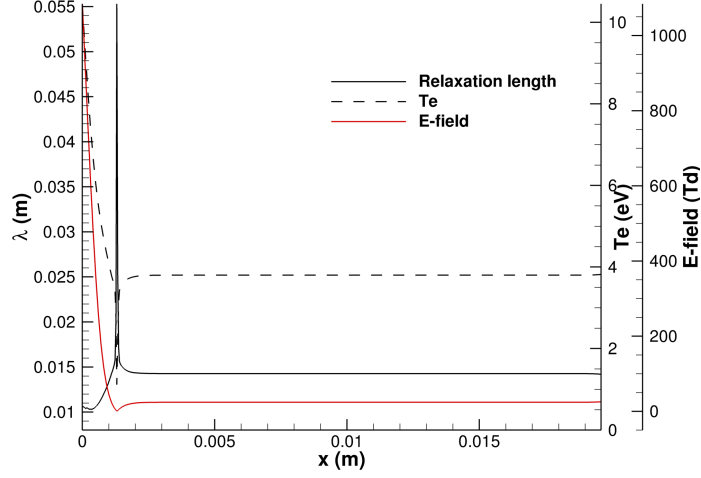


Fig. 4.7. The relaxation length for pure argon simulations at the peak voltage of pulse.

As a simple extension of the baseline model (Cases 1b and 2 in Table 4.4), a zero-dimensional electron energy equation (averaged over the domain) was solved. This model had the following form:

$$\begin{aligned} \frac{\partial}{\partial t} \left[ \frac{3}{2} n_e (T_e - T_n) \right] &= jE - \frac{3}{2} n_e \delta_m (T_e - T_n) \nu \\ - \frac{3}{2} n_e \sum_j \nu_j \Delta \epsilon_j \left\{ 1 - \exp \left[ -\Delta \epsilon_j \left( \frac{1}{T_n} - \frac{1}{T_e} \right) \right] \right\} \end{aligned} \quad (4.1)$$

Here the parameters  $\nu_j$  are the collision frequencies for ionization, excitation in argon, rotational excitation of water molecules, vibrational stretching, and bending frequencies of water molecules, obtained from Bolsig+ and LxCat [40, 65, 74]. The values of  $\Delta \epsilon$  for rotational excitation, vibrational stretching, and bending of water molecules are 0.0046 eV, 0.4595 eV, and 0.1977 eV, respectively [74]. The values of  $\Delta \epsilon$  for excitation, impact ionization, and step-wise ionization of argon are 11.6 eV, 15.8 eV, and 4.16 eV, respectively [65].

To recapitulate, one-dimensional calculations were carried out for a plane-to-plane electrode configuration (Fig. 2.1) with a 2 cm gap in 3 Torr, room-temperature argon gas. The powered electrode lay at the left of the computational domain, and was

Table 4.4.  
Classification of simulation cases.

Case 1	a - complete LFA b - only elastic losses c - elastic & inelastic losses for $T_e$ decay	Pure Argon $i = \text{Ar}^+, e, \text{Ar}^*, \text{Ar}_2^+, \text{Ar}$
Case 2	elastic & inelastic losses for $T_e$ decay	Argon-Water Mixture $i = \text{Ar}^+, e, \text{Ar}^*, \text{Ar}_2^+, \text{Ar}$ $\text{H}_2\text{O}^+, \text{H}_3\text{O}^+, \text{ArH}^+, \text{H}_2\text{O}$

driven by the 3 ns, 850 V pulse shown in Fig. 4.4. The pulse repetition frequency was 30 kHz (33.33  $\mu\text{s}$  between pulses). Both argon and argon-water kinetic mechanisms were considered (Table 4.4), and a systematic exploration of physical and numerical uncertainty of the model was carried out.

#### 4.2.1 Resolution

A numerical resolution study was carried out first to determine the requirements for computational accuracy. Fig. 4.8 shows results for different temporal and spatial resolution. Fig. 4.8(a) shows the conduction current and total current (conduction plus displacement current) for different values of the time step  $\Delta t$ . These results correspond to a single pulse of Case 2, with 300 cells across the domain and time steps varying between  $\Delta t = 1$  ps and  $\Delta t = 100$  ps. Fig. 4.8(b) shows profiles of the electron number density at a time corresponding to the pulse peak for Case 2. Here the time step is fixed at  $\Delta t = 1$  ps, and the number of cells across the domain is varied between 75 and 1200. It can be seen that during the pulse, high resolution in time is necessary. Spatial convergence is achieved with 600 or more points across the domain ( $\Delta x = 33 \mu\text{m}$ ).

An additional study was carried out to show that calculations with fixed and variable time steps produced the same results. The results are shown in Fig.4.9. The

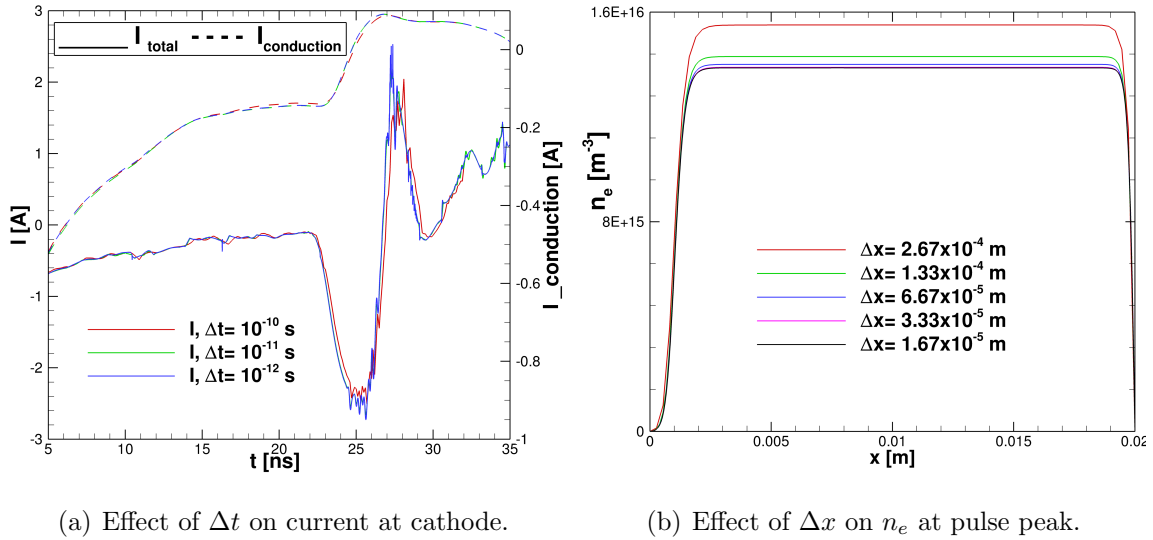
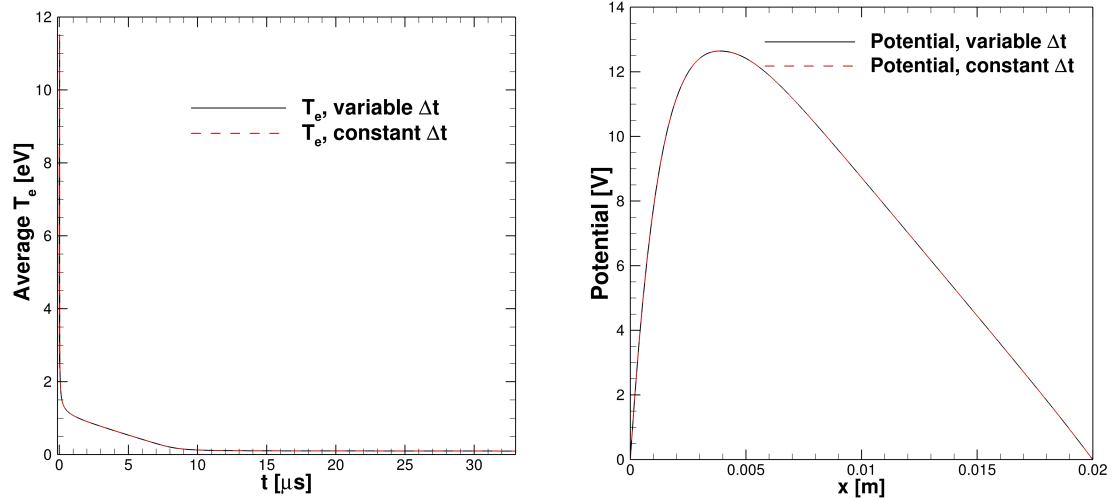


Fig. 4.8. Temporal and spatial resolution study for Case 2 from uniform state through one pulse.

electron temperature averaged over the domain is shown as a function of time in Fig. 4.9(b), and the spatial variation of the potential at  $t = 20 \mu\text{s}$  is shown in Fig.4.9(b). The fixed and variable time step calculations are seen to produce identical results.

The temporal and spatial studies represented in Figs. 4.8 and 4.9 were obtained for a single pulse. The remaining calculations were carried out for many pulses until a periodic condition was obtained. Tests were carried out to determine the required number of pulse repetitions to achieve a state in which the results obtained at corresponding times ( $\hat{t} = t \bmod T$ , where  $T = 33.33 \mu\text{s}$  is the pulse period) were negligible between successive pulses. As shown in Fig.4.10, the differences between number densities at fixed  $\hat{t}$  are imperceptible after about 40 pulses (maximum  $\Delta n_e \leq 10^{12} \text{m}^{-3}$ ).

To investigate the effect of initial conditions, cases with different initial number densities were investigated to show that each would reach the same periodic state. The three different sets of initial conditions considered here are presented in Table 4.5. Fig. 4.11 shows the numerical simulation results for the total current at the cathode for each case. The results for the periodic state are essentially indistinguishable, but changing initial number densities does change the number of pulses required to reach



(a) Effect of variable time step on average  $T_e$ . (b) Effect of variable time step on potential distribution.

Fig. 4.9. Comparison of variable and constant time stepping for Case 2.

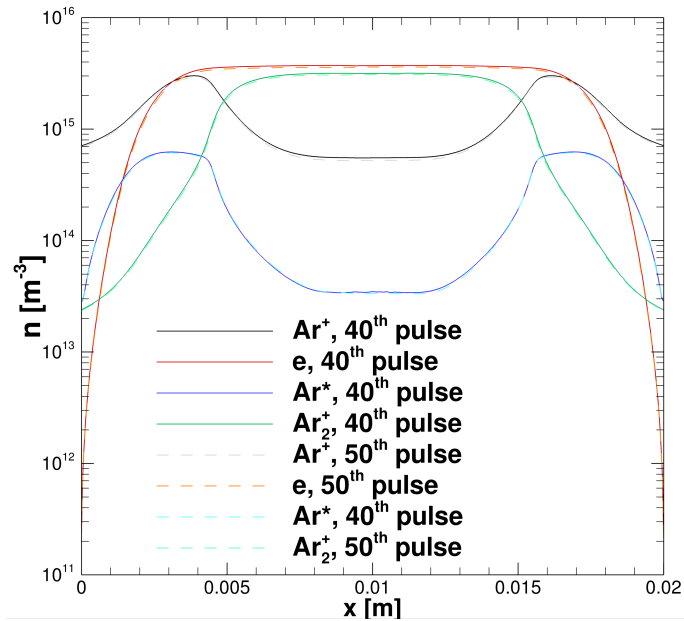


Fig. 4.10. Number density profiles at  $\hat{t} = 20 \mu\text{s}$  for different pulse numbers, Case 1a.

Table 4.5.  
Varying initial conditions, number densities in  $\text{m}^{-3}$ .

Case	$n_{e^-}$	$n_{Ar^+}$	$n_{Ar^*}$	$n_{Ar_2^+}$
IN-1	$1.0 \times 10^{16}$	$5.0 \times 10^{15}$	$1.0 \times 10^{17}$	$5.0 \times 10^{15}$
IN-2	$2.0 \times 10^{16}$	$1.0 \times 10^{16}$	$1.0 \times 10^{17}$	$1.0 \times 10^{16}$
IN-3	$1.0 \times 10^{15}$	$5.0 \times 10^{14}$	$1.0 \times 10^{16}$	$5.0 \times 10^{14}$

the periodic state. The case with the lowest initial number densities, IN-3, took the longest time to reach the periodic state.

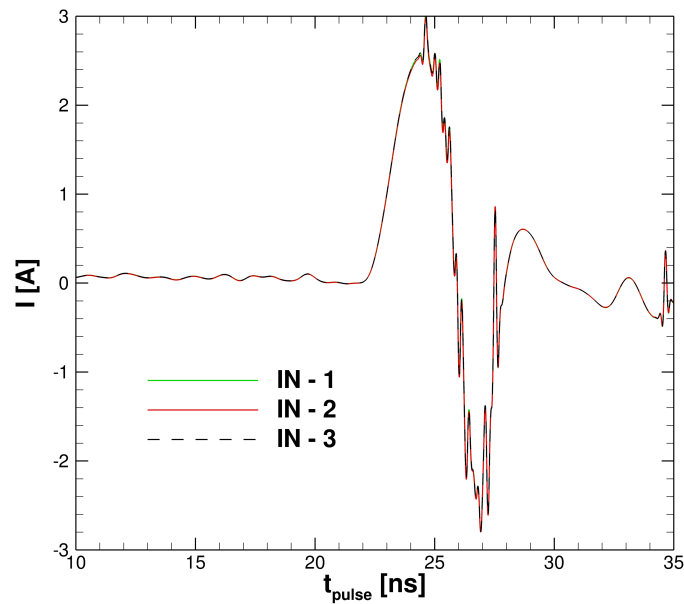


Fig. 4.11. Periodic states of simulations carried out for the initial number densities listed in Table 4.5. Total current  $I(t)$  at cathode, Case 1a.

For periodic state conditions, Fig. 4.12 shows the relaxation of the potential after the pulse for Case 1a. After the applied voltage returns to zero, the magnitude of the maximum potential starts to decrease. This can be seen clearly when  $\hat{t} < 1 \mu\text{s}$ . Around  $1 \mu\text{s}$ , however, the potential distribution begins to reflect a two cathode

discharge [82], and remains in that configuration for a long time. The decay of potential in the middle of the domain takes more than  $33 \mu\text{s}$ , thus the electron temperature in the middle of the domain always remains above ambient temperature for this physical model.

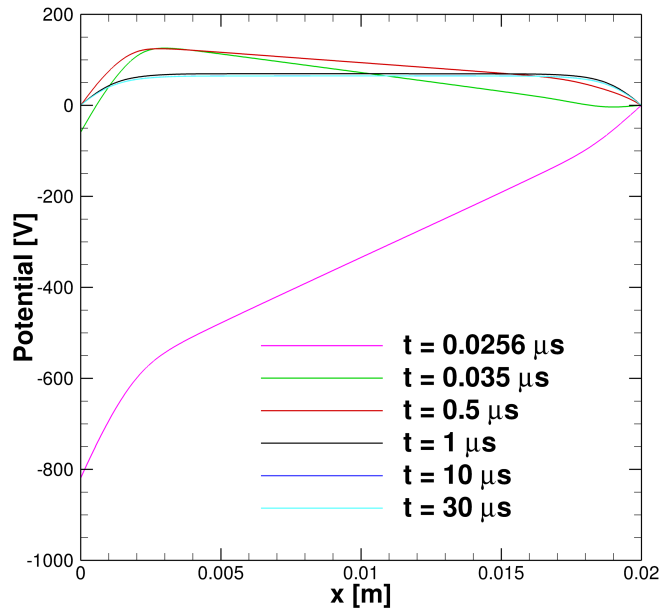


Fig. 4.12. Potential distribution  $\phi(x)$ , Case 1a.

The standard deviation of the experimental voltage is about 8% (Fig. 4.2). To evaluate the effect of uncertainty in the input voltage on the results of the simulations, calculations were carried out for three different voltage profiles: the nominal case, a case 8% low, and a case 8% high. The results of these three simulations are compared in Fig. 4.13. The spatial distribution of the number densities and potential are shown for the peak of a pulse in Fig. 4.13(a). The corresponding time-series data for current are shown in Fig. 4.13(b). The form of the curves is the same in each case, with a slight variation in magnitude. As expected, higher voltages lead to higher number densities and currents, but the variation in the predicted values lies within the experimental uncertainty for these quantities. One of the key experimental measurements that we aim to replicate is the decay of the electron number density

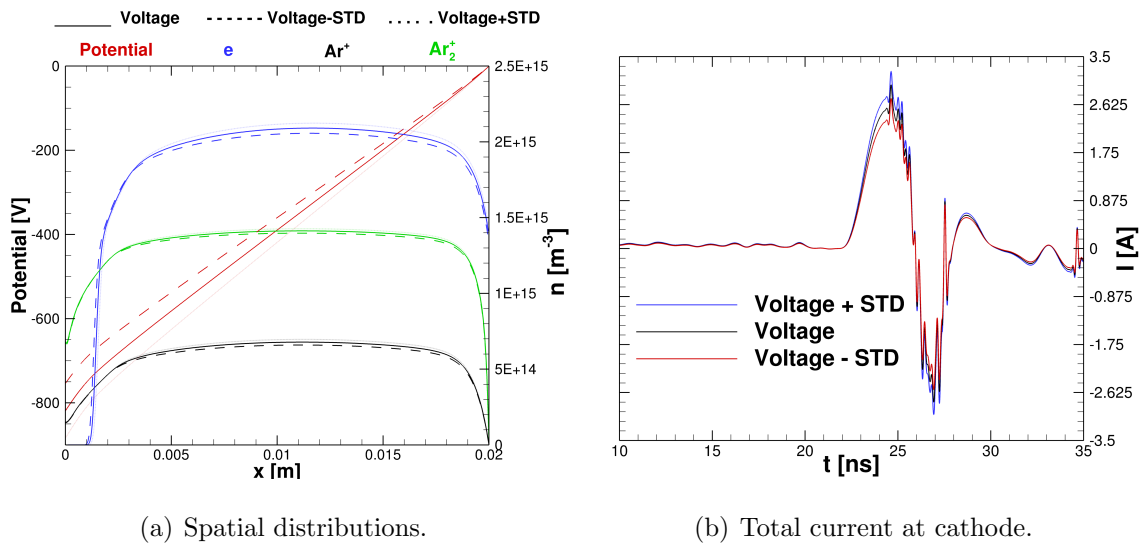
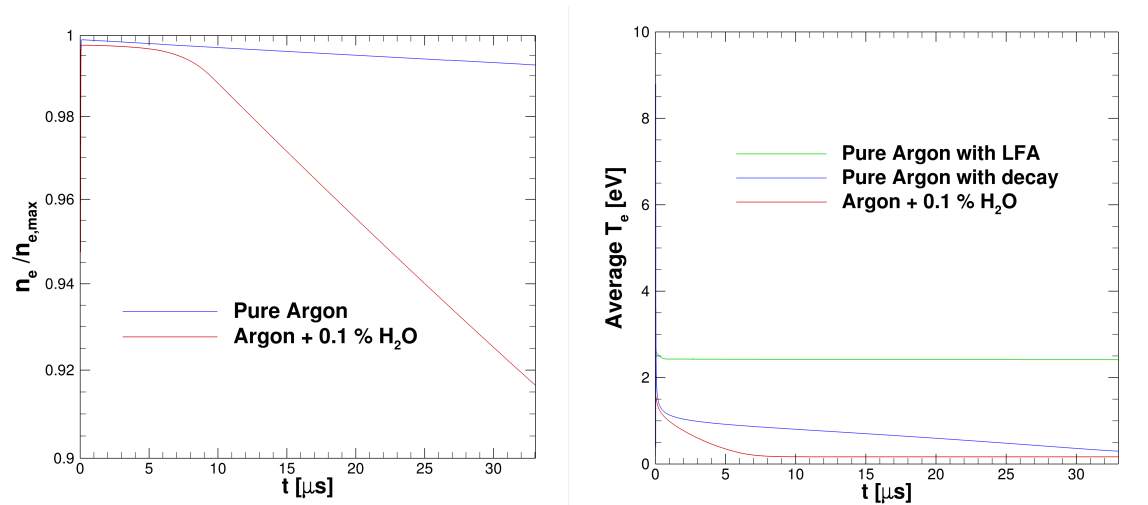


Fig. 4.13. Effect of uncertainty in input voltage profile on solution for Case 1a.

after the pulse. The experimental data shown in Fig. 4.3 display an initially slow decay, followed by a more rapid decay for times greater than  $10 \mu\text{s}$  after the pulse. The corresponding data from the simulations,  $n_e(t)$  in the center of the domain, are shown in Fig. 4.14(a). The data are non-dimensionalized with  $n_{e,max}$  for comparison on the same scale; the maximum values are  $4.05 \times 10^{15} \text{ m}^{-3}$  and  $3.25 \times 10^{15} \text{ m}^{-3}$  for the pure argon and argon-water chemistry, respectively. For pure argon chemistry, the decay profile is too slow and does not resemble the experimental data. The main reason for this effect in the simulations is the very slow decay of the electric field, Fig.4.12, and thus the electron temperature in the local field approximation. This result is illustrated in Fig.4.14(b).

#### 4.2.2 Physical Models

More complex physical models were explored in an attempt to more accurately capture the decay of the electron temperature. First, the zero-dimensional electron equation of Eqn. 4.1 was solved for pure argon chemistry. This model performs



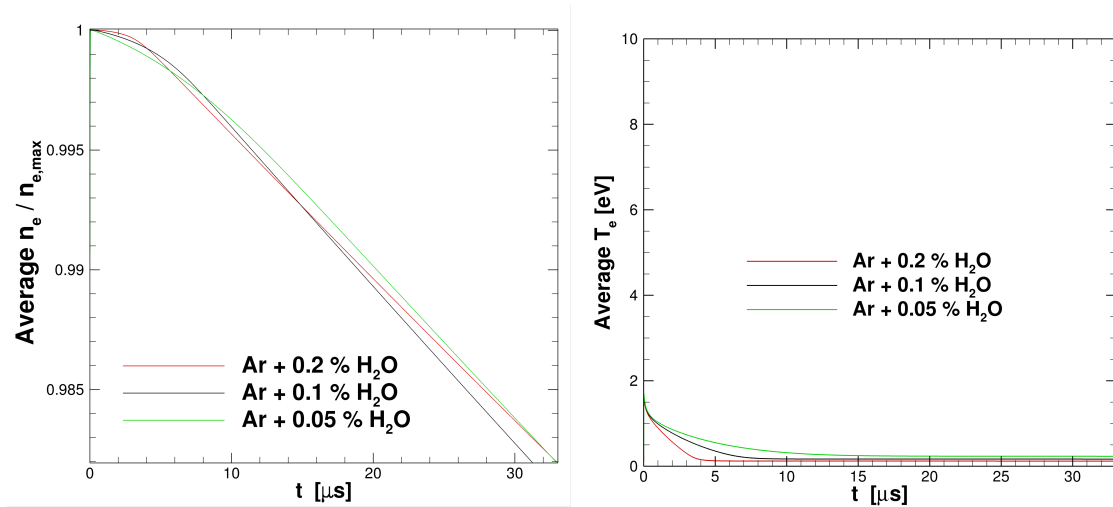
(a) Electron number density at center of domain.

(b) Average electron temperature.

Fig. 4.14. Decay profiles for pure argon with LFA (Case 1a), pure argon with energy equation (Case 1b), and argon-water mixture with energy equation (Case 2).

better than the local field approximation, but the decay rate still does not match the experimental results. Argon-water chemistry was considered next, with the addition of 0.1% water to the system. For this case, the decay profile becomes similar to the experimental results. The argon-water mixture model predicts that the electron temperature reaches ambient at about 12  $\mu\text{s}$ , and the electron number density decay accelerates around 10  $\mu\text{s}$  as observed in the experiment.

In an attempt to bound the water contamination that might have occurred in the experiments, simulations were carried out for a range of values, and the results compared to the experimental decay profiles. The results are shown in Fig. 4.15, with the average electron temperature in Fig. 4.15(b) and the corresponding electron number density in Fig. 4.15(a). As expected, the decay rate increases with the presence of increasing percentages of water. Comparing with the experimental decay rates, the experimental water percentage is estimated to lie between 0.1% and 0.2%. The number densities are non-dimensionalized ( $n_e/n_{e,max}$ ) to present the decay characteristics

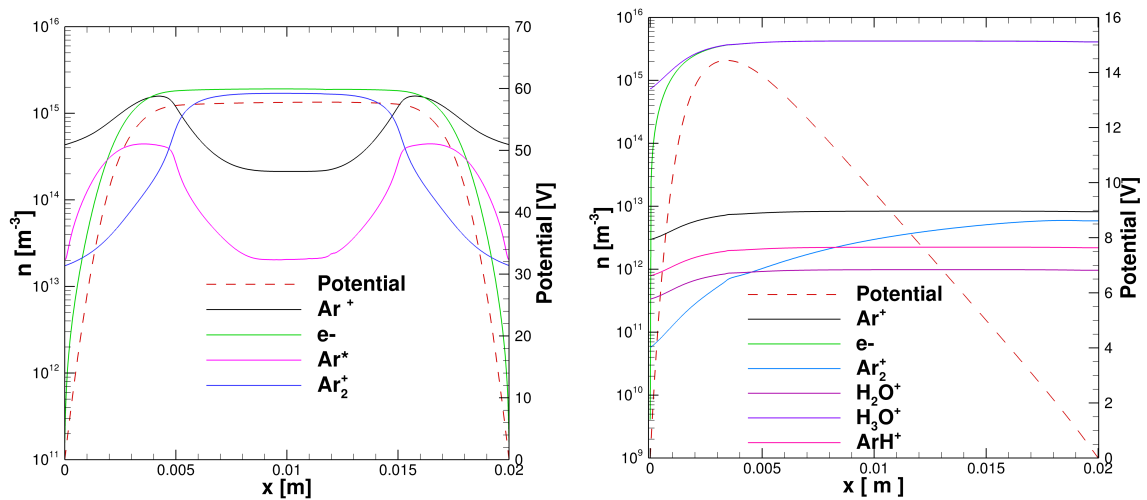


(a) Average electron number density.

(b) Average electron temperature.

Fig. 4.15. Decay profiles for argon-water simulations with different water percentages (variations of Case 2 model).

on the same scale. The average  $n_{e,max}$  values are  $3.2 \times 10^{-15} \text{ m}^{-3}$ ,  $3.8 \times 10^{-15} \text{ m}^{-3}$ , and  $4.2 \times 10^{-15} \text{ m}^{-3}$  for 0.2%, 0.1%, and 0.05% of water, respectively.



(a) Pure argon with LFA, Case 1a.

(b) Argon-water mixture, Case 2

Fig. 4.16. Number densities for two different chemistry models at the end of the decay period ( $\hat{t} = 33 \mu\text{s}$ ).

The predicted solution profiles are shown for both chemistry models in Fig. 4.16 for a time corresponding to the end of the decay period ( $\hat{t} = 33 \mu\text{s}$ ). Again, the potential for the Case 1a simulations relaxes slowly; here the potential in the middle of the domain is still 60 V, Fig. 4.16(a). Significantly lower potentials are predicted by the Case 2 model, Fig. 4.16(b). The dominant ion for the Case 1a simulations is  $\text{Ar}^+$  during the pulse, whereas  $\text{Ar}_2^+$  becomes dominant toward the end of the decay period. For the Case 2 simulations, the dominant ion is  $\text{H}_3\text{O}^+$ .

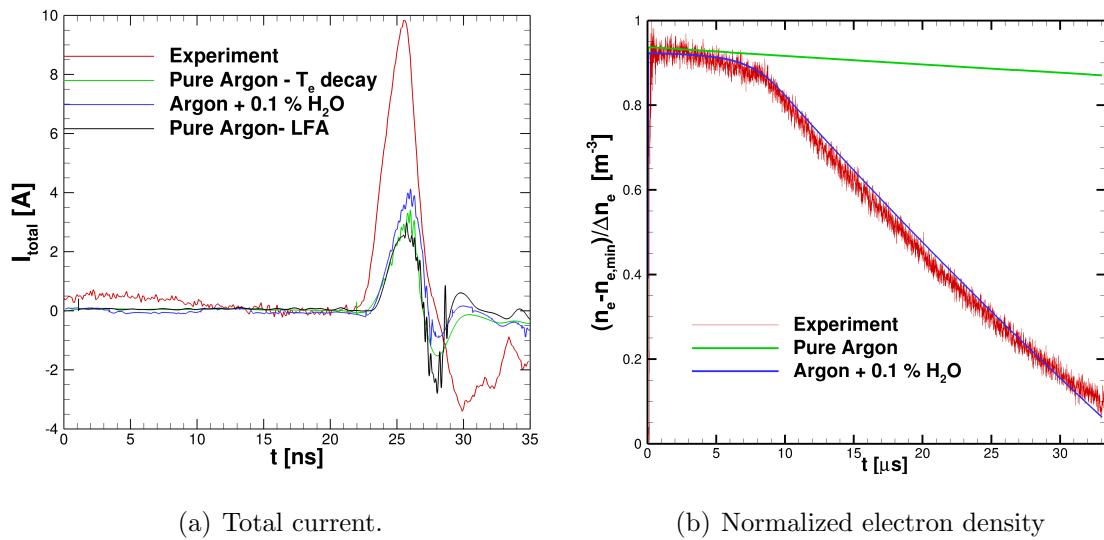


Fig. 4.17. Comparison of the total current and the normalized  $n_e$  profiles for different models. Results shown for one repetition period ( $33 \mu\text{s}$ ) in the periodic state.

Finally, Fig. 4.17(a) compares the total current at the cathode predicted by the simulations to the experimental data. The experimental values are 2-4 times larger than the simulation results. A possible reason for this mismatch is that the periodic state reached with simulations has a lower number density profile compared to the experiment. The computed current profiles qualitatively match the experimental data, except for lagging at the end of the pulse. Fig. 4.17(b) shows the comparison of the normalized number density decay profiles. The reason for normalization is to show that the form of the decay profiles matches the experiment; the absolute

number density, however, does not match. For the normalization, the maximum and minimum values of number densities, and the difference of those,  $\Delta n_e = n_{e,max} - n_{e,min}$ , are obtained from Fig. 4.3 for the experimental data. The values are listed above—see the discussion of Fig. 4.14(a).

### 4.2.3 Summary

One-dimensional simulations of a pulsed discharge with a 3 ns, 850 V pulse and a 30 kHz pulse repetition frequency were carried out and compared with experimental data. The discharge was created in a plane-to-plane electrode configuration with a 2 cm gap in 3 Torr argon. The model employed the drift-diffusion approximation for species motion, and the self-consistent electric field was obtained through the solution of the Poisson equation. The numerical approach employed Scharfetter-Gummel spatial discretization, a variable time stepping procedure and implicit solution of the Poisson equation.

The baseline physical model utilized the local field approximation to determine transport and rate coefficients. Since the local field approximation predicted an inaccurate relaxation of the electron temperatures, profiles of the electron temperature decay in time were explored with a simple elastic collision model. In an extended model, non-local-field effects were investigated by a solving simplified electron energy equation averaged over the domain. To explore the effects of leakage of a small amount of water vapor into the experimental chamber, calculations were carried for both a pure argon kinetic model and an argon-water model.

The model generally underestimated the measured electron number densities, but the inclusion of additional physical effects due to trace amounts of water vapor, i.e. faster relaxation of the electron temperature and formation of  $\text{H}_3\text{O}^+$  ions, helped to reduce the discrepancy with experiment.

## 5. SIMULATIONS WITH NON- LOCAL EFFECTS

The description and discussion of the local field approximation were given in the previous chapters. In this section, the reasons why LFA is not sufficient and when it needs to be replaced with the non-LFA will be discussed. Simulations with the electron thermal energy equation are used to explore non-local effects. The results from the two physical approaches are compared.

The local field approximation assumes that spatial inhomogeneities are small, and that collision frequencies are high. For low pressures, these assumptions start to fail [97]. Since we consider low-pressure discharges here, non-local effects should be checked carefully.

The electron temperature conservation equation is solved to capture the electron temperature profiles, and transport coefficients and reactions rates are obtained by assuming the local mean energy approximation. Grubert and et al. [98] recommend LMEA for RF discharges, whereas LFA is recommended for DC glow discharges. The information provided in Chapter 3 are used in this chapter; the independent variable in the fitting function is shifted to  $T_e$  from  $E/N$ .

In this chapter, an investigation of non-local effects by checking the electron energy relaxation length is described. After the description of the governing equations and boundary conditions, the numerical results are presented for the pulse discharge problem which has been discussed previously.

### 5.0.1 Electron Energy Relaxation Length

The range of applicability of the local field approximation can be checked via electron energy relaxation length,  $\lambda_e$ . The electron energy relaxation length can be obtained as follows by assuming that inelastic reactions are most frequent.

$$\lambda_\epsilon \cong \sqrt{D_e \tau_e} \quad \tau_e^{-1} = \delta\nu + \nu^* \quad (5.1)$$

where  $\delta = 2m_e/M_{Ar}$  is the mass ratio,  $\nu$  is the elastic collision frequency, and  $\nu^*$  is the inelastic collision frequency.

If the relaxation length is much smaller than the characteristic plasma length ( $\lambda_\epsilon \ll L$ ), the LFA can be used safely. The electron kinetics are confined to the local region; electron transport coefficient and reaction rates can be obtained from the local electric field.

If the characteristic length of the plasma is close to the relaxation length,  $\lambda_\epsilon \approx L$ , diffusion of electrons is as fast as the relaxation of the electron energy, indicating that there will be non-local regions in the domain [99].

When the relaxation length is much greater than the characteristic plasma length,  $\lambda_\epsilon \gg L$ , the whole domain will be fully non-local: kinetic equations should be solved to calculate the electron energy distribution function [97].

For relatively high pressures ( $P > 10 - 10^2$  Torr, [100]),  $\lambda_\epsilon$  is usually shorter than the discharge length by a couple of orders of magnitude. For lower pressures,  $\lambda_\epsilon$  is usually larger than the discharge domain, and the potential distribution characterizes the EDF through the whole domain. Fig. 5.1 shows the variation of the relaxation length with respect to pressure using Eqn. 5.1. Each term is obtained by using LxCAT and Bolsig+, as mentioned in the previous chapter. The Rammsour effect causes a relentless increment of the relaxation length for lower E/N and  $T_e$  range.

## 5.1 Thermal Electron Energy Equation

In the drift-diffusion approximation, it is appropriate to solve the thermal energy equation instead of total energy equation, Eqn. (2.4). The system of equations for the two-moment model is as follows:

$$\begin{aligned} \frac{\partial n_j}{\partial t} + \frac{\partial \Gamma_j}{\partial x} &= S_j \\ \frac{\partial}{\partial t} \left( \frac{3}{2} k_b T_e \epsilon_e \right) + \nabla \cdot \left( \frac{3}{2} n_e k_b T_e \mathbf{v}_e \right) &= -\nabla \cdot \mathbf{Q}_e - p_e \nabla \cdot \mathbf{v}_e + M_e \end{aligned} \quad (5.2)$$

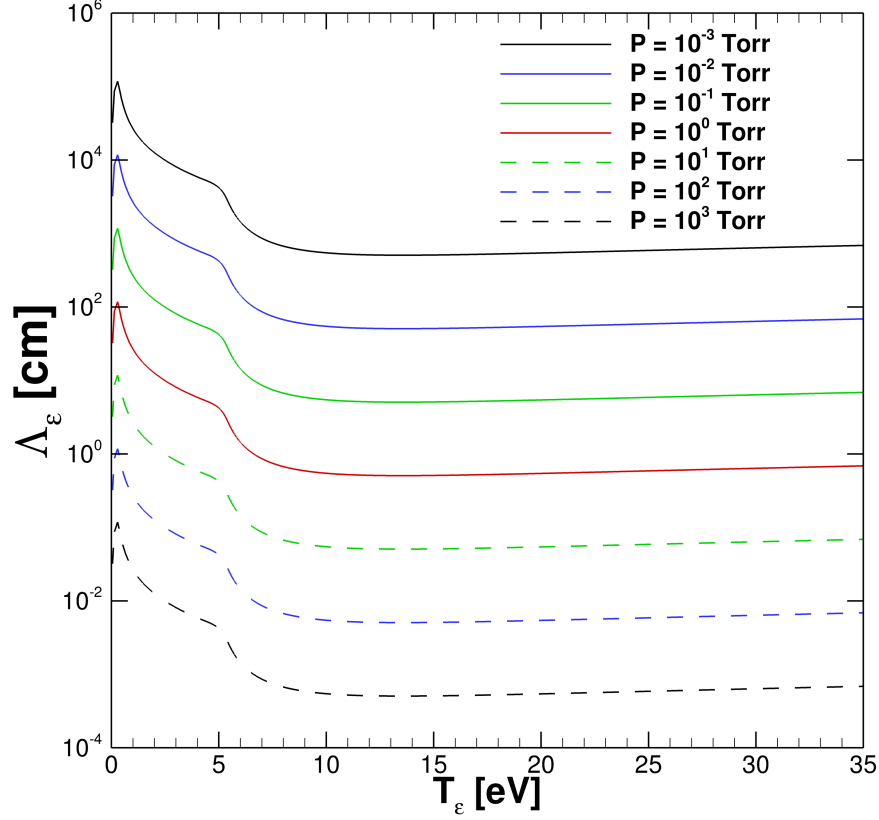


Fig. 5.1. The electron energy relaxation length calculated by using elastic and excitation collision frequencies of argon from Bolsig+ and LxCAT [40, 101] with respect to mean electron energy for various pressures.

where  $Q_e$  is the heat flux term, with the following form:

$$Q_e = -\kappa_e \nabla T_e = -\frac{5}{2} n_e D_e \nabla (k_b T_e) \quad \text{and} \quad \kappa_e = \frac{5 n_e D_e k_b}{2} \quad (5.3)$$

$\kappa_e$  is the thermal conductivity for electrons. The electron pressure can be written as:

$$P_e = n_e k_b T_e \quad (5.4)$$

Finally, the source term for electron is the combination of three collision source terms.

$$M_e = S_e \epsilon_e + \sum_r R_{re} \Delta H_{re} + \frac{n_e q}{(m_e + m_n) \mu_e} \times [-3k_b(T_e - T_n) + m_n |\mathbf{v}_e - \mathbf{v}_n|^2] \quad (5.5)$$

where  $R_{re}$  is the rate of production or loss of electrons from corresponding reactions and  $\varepsilon_e$  is the energy gain or loss from the corresponding reactions. The relation between the R and S is as follows:

$$\begin{aligned}
 S_e &= m_e \sum_r R_{re} = \frac{\partial}{\partial t} (m_e n_e) \\
 \sum_{s=1}^N \nu'_{rs} M_s &\rightarrow \sum_{s=1}^N \nu''_{rs} M_s \\
 R_r &= k_r \prod n_s^{\nu'_{rs}}
 \end{aligned} \tag{5.6}$$

In order to calculate the heat of reaction,  $\Delta H_{re}$ , the heat of formation of species should be known. Table 5.1 lists the species heat of formation at the room temperature from various references. Since the dimmer argon ion can be the combination of  $Ar - Ar^+$  or  $Ar^* - Ar^+$ , there are various heat of formation quoted in the literature for this species. The chosen value is calculated from the ionization of dimmer argon molecule ( $Ar_2$ ).

Knowing the heat of formation of species, the heat of each reaction can be calculated by using:

$$\Delta \mathcal{H}_r^0 = \sum_{s=1}^N (\nu''_{rs} - \nu'_{rs}) \mathcal{H}_{r,s}^0 \tag{5.7}$$

The calculated heat of reactions are listed in Table 5.2. The heat of formation for water vapor excitation reactions are also provided. The discretization of the governing equations and the boundary conditions for drift-diffusion equations are provided in Chapter 2.

### 5.1.1 Boundary Conditions

For the anode boundary, the gradient of the electron temperature was taken to be zero. For the cathode boundary, two different boundary conditions were investigated. The first one is the constant electron temperature on the cathode boundary. The second one is the average of the absorption temperature and the secondary emis-

Table 5.1.  
Species in the simulations and their heat of formation referenced to the room temperature.

#	Species	$\mathcal{H}_s^0$ [eV/particle]	References
1	Ar	0	
2	Ar <sup>+</sup>	15.76	[65]
3	Ar <sub>2</sub> <sup>+</sup>	14.45	[102, 103]
4	Ar*	11.55	[65, 104]
5	e <sup>-</sup>	0	
6	H <sub>2</sub> O	-2.52	[105]
7	H <sub>2</sub> O <sup>+</sup>	10.21	[105]
8	H <sub>3</sub> O <sup>+</sup>	6.28	[105]
9	ArH <sup>+</sup>	12.11	[105]
10	OH	0.39	[105]
11	H <sub>2</sub>	0	
12	H	2.27	[105]
13	H <sub>2</sub> O*	0.0046	[65]
14	H <sub>2</sub> O*	0.19	[65]
15	H <sub>2</sub> O*	0.459	[65]

sion temperature of electrons [30]. The electron temperature at the cathode has the following form under this model:

$$T_{e,cathode} = \frac{n_e k_r T_{e,abs} + \gamma \Gamma_i T_{e,sec}}{n_e k_r + \gamma \Gamma_i} \quad (5.8)$$

where  $T_{e,sec}$  is the secondary emission temperature, which is set to 1 eV for the simulations. The parameter  $k_r = \sqrt{k_B T_{e,abs} / 2\pi m_e}$  is the recombination rate.  $T_{e,abs}$  is the absorption temperature quantifying the cooling of electrons due to diffusing in the opposite direction of the field. It can be obtained from the field in the vicinity of the cathode:

Table 5.2.  
Heat of reaction for each reactions.

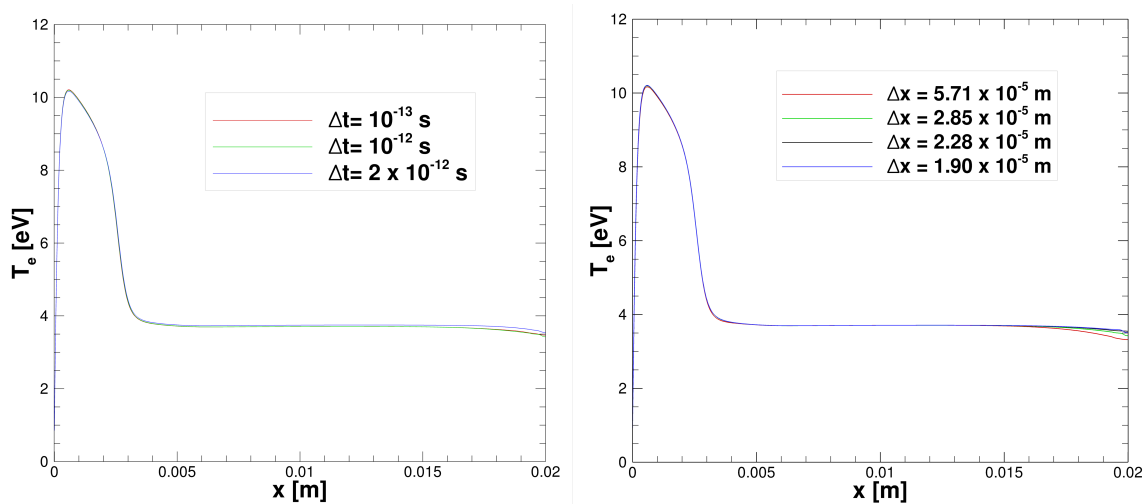
#	Processes	$\Delta\mathcal{H}_{r,s}^0$ [eV/particle]
k <sub>1</sub>	$e + \text{Ar} \rightarrow \text{Ar}^+ + 2e$	15.76
k <sub>2</sub>	$e + \text{Ar} \rightarrow \text{Ar}^* + e$	11.55
k <sub>3</sub>	$e + \text{Ar}^* \rightarrow \text{Ar}^+ + 2e$	4.21
k <sub>4</sub>	$e + \text{Ar}^* \rightarrow \text{Ar} + e$	-11.55
k <sub>5</sub>	$e + \text{Ar}_2^+ \rightarrow \text{Ar}^* + \text{Ar}$	-2.9
k <sub>6</sub>	$e + \text{Ar}^+ \rightarrow \text{Ar}^*$	-4.21
k <sub>7</sub>	$e + e + \text{Ar}^+ \rightarrow \text{Ar}^* + e$	-4.21
k <sub>8</sub>	$\text{Ar}^+ + 2\text{Ar} \rightarrow \text{Ar}_2^+ + \text{Ar}$	-1.31
k <sub>9</sub>	$\text{Ar}^* + \text{Ar}^* \rightarrow \text{Ar}^+ + \text{Ar} + e$	-7.34
k <sub>10</sub>	$\text{Ar}^* + \text{H}_2\text{O} \rightarrow \text{Ar} + \text{H}_2\text{O}$	-11.55
k <sub>11</sub>	$\text{Ar}^+ + \text{H}_2\text{O} \rightarrow \text{Ar} + \text{H}_2\text{O}^+$	-3.03
k <sub>12</sub>	$\text{Ar}^+ + \text{H}_2\text{O} \rightarrow \text{ArH}^+ + \text{OH}$	-0.74
k <sub>13</sub>	$\text{ArH}^+ + \text{H}_2\text{O} \rightarrow \text{Ar} + \text{H}_3\text{O}^+$	-3.31
k <sub>14</sub>	$\text{H}_2\text{O}^+ + \text{H}_2\text{O} \rightarrow \text{H}_3\text{O}^+ + \text{OH}$	-1.02
k <sub>15</sub>	$e + \text{H}_3\text{O}^+ \rightarrow \text{H} + \text{H}_2\text{O}$	-6.23
k <sub>16</sub>	$e + \text{H}_3\text{O}^+ \rightarrow \text{H}_2 + \text{OH}$	-5.89
k <sub>17</sub>	$e + \text{H}_3\text{O}^+ \rightarrow \text{H} + \text{H} + \text{OH}$	-1.35
k <sub>18</sub>	$e + \text{H}_2\text{O} \rightarrow \text{H}_2\text{O}_{\text{rot}}^* + e$	-0.0046
k <sub>19</sub>	$e + \text{H}_2\text{O} \rightarrow \text{H}_2\text{O}_{\text{vib}}^* + e$	-0.1977
k <sub>20</sub>	$e + \text{H}_2\text{O} \rightarrow \text{H}_2\text{O}_{\text{vib}}^* + e$	-0.4595

$$\frac{\partial T_{e,abs}}{\partial x} = \left( \frac{2q}{5k_B} \right) \frac{\partial V}{\partial x} \quad (5.9)$$

The role of the boundary as cathode or anode is determined by checking the directions of the electron and ion flux.

## 5.2 Results with Electron Thermal Energy Equation Solver

The resolution study for the simulations with electron temperature equation solutions is presented in Fig. 5.2. The resolution study was conducted with a constant external voltage at the cathode,  $V_{ext} = -300$  V, and all the other parameters were kept the same as those used for the LFA case simulations. Temporal resolution is achieved for time steps lower than 1 ps, Fig. 5.2(a). The solver crashes for time steps larger than 2 ps. Calculations are computationally demanding for the maximum time step is 1 ps. Similarly, to achieve spatial convergence, there should be at least 900 points across the domain, Fig. 5.2(b).



(a) Effect of  $\Delta t$  on spatial  $T_e$  variation. The number of points across the domain is 700. (b) Effect of  $\Delta x$  on  $T_e$ . The time step,  $\Delta t$  is chosen as  $10^{-12}$ s.

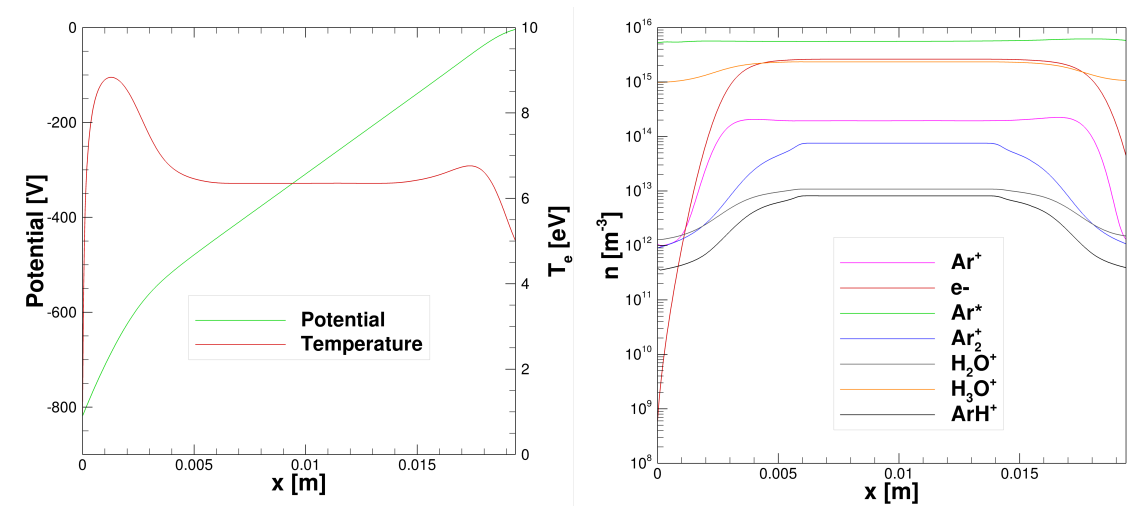
Fig. 5.2. Temporal and spatial resolution study for the simulations with  $T_e$  equations.

To accelerate the computations, variable time steps are used in the time between two pulses by checking the maximum requirements from the dielectric and CFL time

scales. It was observed that the simulations with the two-moment model were more sensitive to the changes in  $\Delta t$ . To eliminate crashes, constant time stepping is used in the simulations presented in this chapter.

To speed convergence to a periodic state, the following results were obtained by restarting the converged calculations from the LFA simulations. These results are included as an initial distribution.

[Since the computational requirements are demanding, the simulations are still running. The presented result is for the simulating of 5 consecutive pulses and time between two pulses.]



(a) Potential and the electron temperature profile.

(b) Number density profiles.

Fig. 5.3. Variables' spatial variation at the pulse peak.

Even for the earlier time in the simulations, it can be observed that  $H_3O^+$  is already dominant ion as in the LFA calculations, Fig.5.3. The peak electron temperature at the cathode sheath is around 9 eV with the overall temperature distribution in the range of 7 eV.

The decay of the electron temperature profile is presented in Fig. 5.4. It can be seen that the electron temperature in the positive column relaxes quickly; the relaxation time to room temperature is consistent with the previous calculations.

The double cathode formation can be observed through the increment of the electron temperature at the anode sheath.

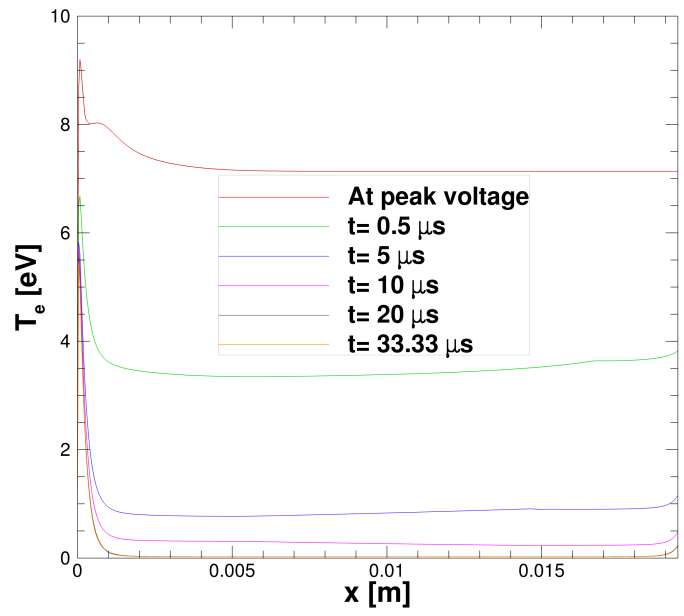


Fig. 5.4. The variation of the electron temperature spatially for various times at the 5th pulse.

The last image from preliminary calculations shows the temporal variation of the electron temperature and the number densities of species, Fig. 5.5. Again, the temporal behavior matches with the previous calculations. The averaged electron temperature reaches room temperature around  $10 \mu s$ . The slope of electron number density decay rate changes around  $12 \mu s$ . Although these results are not converged yet, the computations indicate that it will require convergence by checking the rate of the growth of the number densities. Electron number densities have grown through the executed five pulses with the decrease in the growth rate.

The simulations with thermal electron energy equation show good agreement with the experimental data even for the small number of pulse runs. The simulations with the local field approximations require tens or hundreds of pulse calculations to reach the periodic state. By starting with the same initial number densities, the simulations with non-local effects show convergence behavior for 5th and 8th pulse simulations,

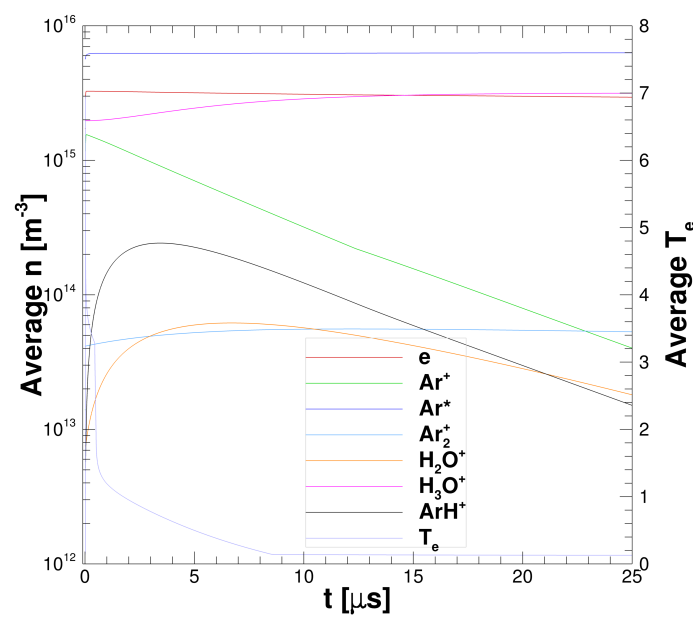
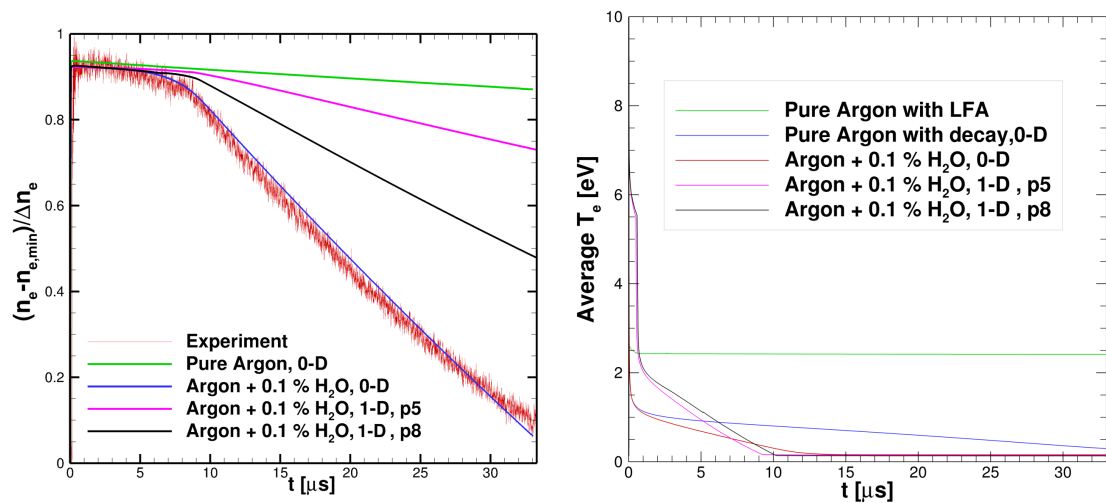


Fig. 5.5. Temporal variation of variables during the 5th pulse computations.



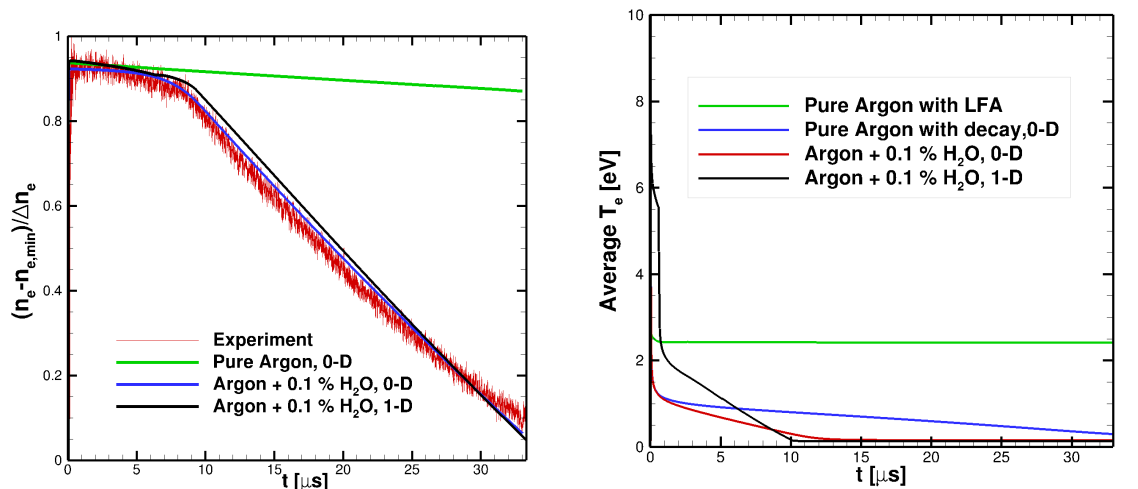
(a) Normalized number densities.

(b) Average electron temperature across the domain.

Fig. 5.6. Normalized electron number densities and average electron temperature for local and non-local approximations.

Fig. 5.6(a). Similarly, the decay profiles for the electron temperatures show good agreement with the previous calculations, Fig. 5.6(b).

The variable time stepping was helpful to accelerate the simulations with the local field approximations and the averaged electron temperature decay profile. The simulations with the thermal electron energy equation are; however, sensitive to changes and the solver crashes when the changes are enforced on the iterations. Thus, these simulations require enormous computational time to run the code for tens of pulses. Since the proposed timeline to get periodic state solutions exceeds the timeline of this study, the following figures show the solutions for only one pulse and after -pulse. In these calculations, the initial number density is chosen as the experimental data.



(a) Normalized number densities.

(b) Average electron temperature across the domain.

Fig. 5.7. Decay profile comparisons with the experimental data [83] for pure argon with LFA, pure argon with energy equation (0-D), and argon-water mixture with energy equation (0-D), and argon-water mixture with energy equation(1-D).

Fig. 5.7(a) shows the normalized electron number density profiles for the experimental data, pure argon with the decay equation (0-D- averaged), Eqn. 4.1, and argon- water mixture with 0-D and 1-D thermal electron energy equations. It seems

that argon + 0.1 % $H_2O$  with 0-D and 1-D electron energy equation; however, the maximum  $n_e$  values are different.

The non-dimensionalization data with  $n_{e,max}$  for comparison on the same scale are that the maximum values are  $4.05 \times 10^{15} \text{ m}^{-3}$  and  $3.25 \times 10^{15} \text{ m}^{-3}$  for the pure argon (0-D) and argon-water chemistry(0-D), respectively. The experimental  $n_{e,max}$  is  $1.75 \times 10^{16} \text{ m}^{-3}$ . The results with 1-D solutions have almost the same maximum electron number density,  $1.70 \times 10^{16} \text{ m}^{-3}$  with the experiment. The inclusions of the non-local effects improve the agreement with the experimental data.

Fig. 5.7(b) shows the average  $T_e$  for the various results: the converged (periodic state) results for LFA simulations and one pulse simulations for the non- LFA simulations. It can be seen that if the electron temperature is obtained directly from the cell, there is almost no decay of the electron temperature. Pure argon with 0-D equation shows the decay behavior, and it is, however, still slow compared to the experiment. The thermalization behavior is observed for argon-water mixtures with each model.

The last image shows the comparisons of the total current on the cathode surface. It can be seen that the agreement with the experimental data is improved with the improvement of the physical model. Although the simulations and experiment agree well in terms of the profile, the peak value of the current could not be achieved with the numerical simulations.

### 5.3 Summary

For low-pressure ranges, the electron energy relaxation length becomes comparable with the plasma domain. The non-local effects; thus, should be included in the solver. This was the outcome of the previous chapter. By doing further analysis and computations, it is stated that non-local effects are essential for the discharge chosen for the simulations.

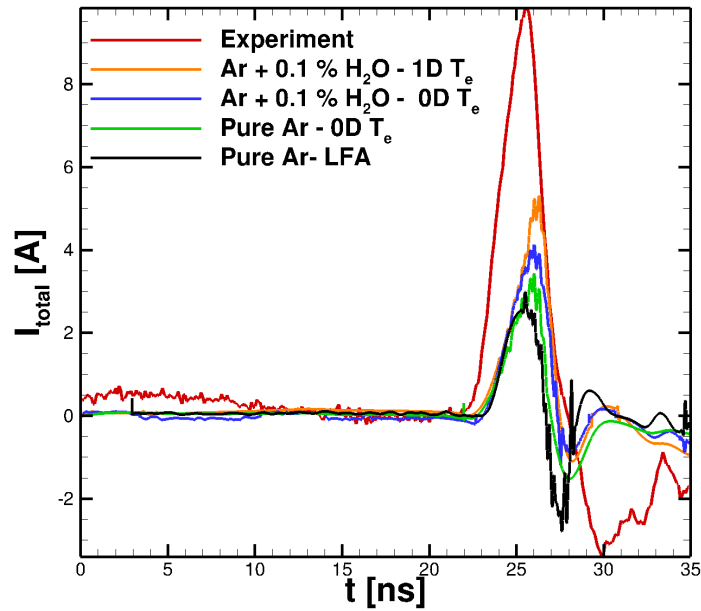


Fig. 5.8. Comparison of the total current with the experimental data [83] at the cathode for pure argon with LFA, pure argon with energy equation (0-D), and argon-water mixture with energy equation (0-D), and argon-water mixture with energy equation (1-D).

The thermal electron energy equation is implemented into the solver to capture the non-local effects. Solving the electron energy equation helps to improve the agreement with the experimental data. Also, the reaction rates are fitted from Bolsig+ for these calculations. It should be noted that the rates from Bolsig+ cause a crash of the code for the LFA simulations because of the enormous production of electrons.

To show quick results, one pulse simulations in which initial conditions are picked from the experimental data are presented. The agreement is overall better than the converged LFA and averaged electron temperature equation solutions.

## 6. CONCLUSIONS

In this section, conclusions are drawn about the robustness and the cost of the gas discharge simulations. Recommendations for future work are provided with the aim of increasing the range of applicability of the solver and minimizing computational requirements.

### 6.1 Summary and Conclusions

In the first chapter, a general overview of plasma and gas discharges was provided in the content of applications in the aerospace industry. The fundamental physics of DC discharge and glow discharges were then presented. The stiffness of plasma solvers was discussed. High temporal and spatial resolution are required to capture processes such as ionization, relaxation, and so on. High spatial resolution is required to capture sharp gradients at the edge of the sheaths.

Time scales of plasma and flow were compared, and it can be stated clearly that the optimum numerical and physical model should be employed for the given problem. The semi-empirical plasma models can be integrated into the flow solver without increasing the computational and physical modeling cost in addition. The studies in which full-coupled plasma and flow solver were achieved discuss the extreme computational cost.

The range of physical models varies between kinetic and continuum approaches. Since a continuum approach is employed in this study, further simplifications are achieved through moments of the Boltzmann equations. One dimensional DC glow discharge computations were carried out for various conditions. Scharfetter-Gummel discretization is used for the fluxes because of its ability to optimize the order of

accuracy for drift- and diffusion-dominated regions. The simplest and the cheapest model that captured the important physics was investigated.

Validation of the model was achieved by comparing with the experimental data. The comparison of the numerical solution with the experimental data is important to analyze the fundamental requirements of the solver. With the light of the numerical data, experimenters might want to check parameters such as the amount of the impurities. The simplest model is used first to model low-pressure nanosecond-pulse discharges. The improvements in the physical models are achieved step-by-step by comparing with the experimental data. It is found that non-local effects should be included for low-pressure argon discharges. Non-local effects were initially investigated through a 0-D electron temperature equation solver.

The local field approximation causes a stagnant decay of electron temperatures and number densities. Since the electron temperatures remain at high values ( $> 1$  eV) for a long time, the production of electron increases with the time. This causes a crash of the solver because of the enormous number density of electrons. To overcome this problem, the curve-fitted reactions rates were used from literature.

Domain-averaged 0-D electron temperature equation was employed, and it was observed that the thermalization time, the profile of electron decay rates were matching with the experiments. The number densities were however 3 - 5 times lower than the experiment. Similarly, the calculated current values are also lower.

It should be clarified again both the local field and non-local field approximations are great simplifications for plasma modeling with respect to a kinetic approach. Further investigations might help to close the gap between kinetic and continuum approaches. It is; however, important to keep computational requirements on the bearable level for the available computer technology.

The thermal electron energy equation was solved with the drift-diffusion equation (two-moment model) to capture the non-local effects more accurately. Although the simulations are still running, the results are promising. Simulations with the local field approximations could not be run with Bolsig+ fitted reaction rates; however,

the electron energy equation is capable of handling to the growth of electron number density during the pulse.

With the thermal electron energy equations, the decay profiles were matching with the experiment. The averaged electron number density is increasing through each pulse while the increment rate is decreasing. This is usually one of the indications of the convergence. The detailed conclusion will be provided upon the studies when they will be completed.

With 1D simulations, it is observed that general discharge behavior can be captured in good agreement with data. It is important to find the optimum model, having acceptable computational and modeling cost while capturing enough information about the discharge.

## 6.2 Recommendations for Future Work

In this section, recommendations for future work are made to improve the computational efficiency and the robustness of the gas discharge solvers. In this study, different discharge conditions were investigated with the 1-D solver. By carefully checking the requirements of the discharges, the numerical and physical approaches are altered to reach the goals.

Firstly, 1-D simulations might not be an effective tool for modeling spatially non-uniform discharges. If the discharge is mostly uniform, 1-D approaches might be a great simplification. Although it is mentioned that the discharge problems investigated in this study are computationally demanding, 2-D computations; however, should be carried out for the flow control purposes.

Secondly, the solver can be examined at higher pressure; the largest pressure investigated in this study is 10 Torr. Atmospheric pressure gas discharges are the most common discharges for flow control purposes. Although the drift-diffusion equation was investigated at the proximity of the application range in this study, drift-diffusion

equations will be more applicable to higher pressure. Different discharge phenomena can be investigated at higher pressures.

Thirdly, the detailed analysis and tabulations can be done for the plasma chemistry. There might be species and reaction rates might not effective as much as other reactions can be examined for different pressures, pulse frequencies, and background gases. This kind of tabulation would be enormously helpful to understand the plasma chemistry.

Fourthly, the verification of the experiment and the numerical model can be assessed more. Experiments with controlled inclusion of impurities might help to validate the numerical model. Moreover, analysis of plasma chemistry for air might be more appropriate for flow control applications. Adding impurities to air discharges can be checked to analyze the effects.

## REFERENCES

## REFERENCES

- [1] P. Carlqvist, “Cosmic electric currents and the generalized bennett relation,” *Astrophysics and Space Science*, vol. 144, no. 1, pp. 73–84, 1988. [Online]. Available: <https://doi.org/10.1007/BF00793173>
- [2] H. Alfven, *Cosmic plasma*. Dordrecht, Holland Boston, Massachusetts Lancaster, England : D. Reidel Publishing Company, 1981.
- [3] F. F. Chen, *Introduction to plasma physics and controlled fusion*, 2nd ed. New York: New York : Plenum Press, 1984.
- [4] A. L. Peratt, “Advances in numerical modeling of astrophysical and space plasmas,” *Astrophysics and Space Science*, vol. 242, no. 1, pp. 93–163, 1996. [Online]. Available: <https://doi.org/10.1007/BF00645112>
- [5] A. A. Fridman and L. A. Kennedy, *Plasma Physics and Engineering*, 2nd ed. Boca Raton, FL: Boca Raton, FL : CRC Press, 2011.
- [6] Y. P. Raizer, *Gas Discharge Physics*. Moscow: Springer- Verlag, 1987.
- [7] J. S. E. S. Townsend, *Electrons in gases*. London : Hutchinson’s scientific and technical publications, 1947. [Online]. Available: <http://lib.ugent.be/catalog/rug01:000701075>
- [8] F. Paschen, “Eine metallcontactpotentialdifferenz,” *Annalen der Physik*, vol. 277, no. 10, pp. 186–209, 1890.
- [9] R. G. Jahn, *Physics of electric propulsion*. Mineola, N.Y.: Mineola, N.Y. : Dover Publications, Inc., 2006.
- [10] E. Fernandez, M. Cappelli, and K. Mahesh, “2 Dsimulations of hall thrusters annual report,” *STAR*, vol. 37, 1999.
- [11] I. D. Boyd, “Numerical simulation of hall thruster plasma plumes in space,” *IEEE Transactions on Plasma Science*, vol. 34, no. 5, pp. 2140–2147, 2006.
- [12] J. Poggie, T. McLaughlin, and S. Leonov, “Plasma aerodynamics: Current status and future directions,” *ONERA Aerospace Lab Journal*, vol. 10, 2015. [Online]. Available: <https://doi.org/10.12762/2015.AL10-01>
- [13] T. Piskin, “Analysis of weakly ionized flows,” Master’s thesis, Middle East Technical University, 2015.
- [14] M. Kim, I. D. Boyd, and M. Keidar, “Modeling of electromagnetic manipulation of plasmas for communication during reentry flight,” *Journal of Spacecraft and Rockets*, vol. 47, no. 1, 2010. [Online]. Available: <http://search.proquest.com/docview/2161746576/>

- [15] L. Duan, X. Wang, and X. Zhong, "Stabilization of a mach 5.92 boundary layer by two-dimensional finite-height roughness," *AIAA Journal*, vol. 51, no. 1, pp. 266–270, 2013. [Online]. Available: <http://dx.doi.org/10.2514/1.J051643>
- [16] R. H. Liebeck, "Design of subsonic airfoils for high lift," *Journal of Aircraft*, vol. 15, no. 9, pp. 547–561, 1978.
- [17] H. Shan, L. Jiang, C. Liu, M. Love, and B. Maines, "Numerical study of passive and active flow separation control over a naca0012 airfoil," *Computers and Fluids*, vol. 37, no. 8, pp. 975–992, 2008. [Online]. Available: <http://dx.doi.org/10.1016/j.compfluid.2007.10.010>
- [18] C. E. Dole and J. E. Lewis, *Flight Theory and Aerodynamics*. New York: John Wiley and Sons., 2nd ed., 2000.
- [19] L. Pack, "Active flow separation control on a naca 0015 wing using fluidic actuators," in *7th AIAA Flow Control Conference, 16-20 June 2014*, ser. 7th AIAA Flow Control Conference. American Institute of Aeronautics and Astronautics, 2014, Conference Proceedings, p. 16 pp.
- [20] A. Starikovskiy and N. Aleksandrov, "Nonequilibrium plasma aerodynamics," in *Aeronautics and Astronautics*, M. Mulder, Ed. Rijeka: IntechOpen, 2011, ch. 3. [Online]. Available: <https://doi.org/10.5772/22396>
- [21] P. Palm, R. Meyer, E. Pl-ogrove, njes, J. W. Rich, and I. V. Adamovich, "Nonequilibrium radio frequency discharge plasma effect on conical shock wave:  $M = 2.5$  flow," *AIAA Journal*, vol. 41, no. 3, pp. 465–469, 2003. [Online]. Available: <https://doi.org/10.2514/2.1968>
- [22] E. Anokhin, S. Starikovskaia, and A. Starikovskii, *Energy Transfer in Hypersonic Plasma Flow and Flow Structure Control by Low Temperature Nonequilibrium Plasma*, ser. Aerospace Sciences Meetings. American Institute of Aeronautics and Astronautics, 2004. [Online]. Available: <https://doi.org/10.2514/6.2004-674>
- [23] V. M. Fomin, P. K. Tretyakov, and J. P. Taran, "Flow control using various plasma and aerodynamic approaches (short review)," *Aerospace Science and Technology*, vol. 8, no. 5, pp. 411–421, 2004. [Online]. Available: <http://www.sciencedirect.com/science/article/pii/S1270963804000367>
- [24] J. P. Boeuf, Y. Lagmich, T. Unfer, T. Callegari, and L. C. Pitchford, "Electrohydrodynamic force in dielectric barrier discharge plasma actuators," *Journal of Physics D (Applied Physics)*, vol. 40, no. 3, pp. 652–662, 2007. [Online]. Available: <http://dx.doi.org/10.1088/0022-3727/40/3/S03>
- [25] B. Jayaraman, C. Young-Chang, and S. Wei, "Modeling of dielectric barrier discharge plasma actuator," *Journal of Applied Physics*, vol. 103, no. 5, pp. 053304–1, 2008. [Online]. Available: <http://dx.doi.org/10.1063/1.2841450>
- [26] M. Robinson, "Movement of air in the electric wind of the corona discharge," *Transactions of the American Institute of Electrical Engineers, Part I: Communication and Electronics*, vol. 80, no. 2, pp. 143–150, 1961.

- [27] C. S. Kalra, S. H. Zaidi, R. B. Miles, and S. O. Macheret, “Shockwaveturbulent boundary layer interaction control using magnetically driven surface discharges,” *Experiments in Fluids*, vol. 50, no. 3, pp. 547–559, 2011. [Online]. Available: <https://doi.org/10.1007/s00348-010-0898-9>
- [28] S. J. Johnson, C. Case, and D. E. Berg, *Active load control techniques for wind turbines*. Washington, D.C : Oak Ridge, Tenn.: Washington, D.C : United States. Dept. of Energy: distributed by the Office of Scientific and Technical Information, U.S. Dept. of Energy, 2008.
- [29] F. O. Thomas, A. Kozlov, and T. C. Corke, “Plasma actuators for cylinder flow control and noise reduction,” *AIAA Journal*, vol. 46, no. 8, pp. 1921–1931, 2008. [Online]. Available: <https://doi.org/10.2514/1.27821>
- [30] J. Poggie, “Multi-fluid modelling of pulsed discharges for flow control applications,” *International Journal of Computational Fluid Dynamics*, vol. 29, no. 2, pp. 180–191, 2015. [Online]. Available: <https://doi.org/10.1080/10618562.2015.1021694>
- [31] C.-C. Wang and S. Roy, *Numerical Simulation of a Gas Turbine Combustor Using Nanosecond Pulsed Actuators*, ser. Aerospace Sciences Meetings. American Institute of Aeronautics and Astronautics, 2013. [Online]. Available: <https://doi.org/10.2514/6.2013-894>
- [32] S. B. Leonov and D. A. Yarantsev, “Plasma-induced ignition and plasma-assisted combustion in high-speed flow,” *Plasma Sources Science and Technology*, vol. 16, no. 1, pp. 132–138, 2006. [Online]. Available: <http://dx.doi.org/10.1088/0963-0252/16/1/018>
- [33] S. Leonov, V. Bitururin, K. Savelkin, and D. Yarantsev, *Progress in Investigation for Plasma Control of Duct-Driven Flows*, ser. Reno, NV. American Institute of Aeronautics and Astronautics, 6-10 January 2003. [Online]. Available: <https://doi.org/10.2514/6.2003-699>
- [34] N. J. Bisek, I. D. Boyd, and J. Poggie, “Numerical study of plasma-assisted aerodynamic control for hypersonic vehicles,” *Journal of Spacecraft and Rockets*, vol. 46, no. 3, pp. 568–576, 2009. [Online]. Available: <https://doi.org/10.2514/1.39032>
- [35] R. L. Kimmel, J. Poggie, and S. N. Schwoerke, “Laminar-turbulent transition in a mach 8 elliptic cone flow,” *AIAA Journal*, vol. 37, no. 9, pp. 1080–1087, 1999. [Online]. Available: <https://doi.org/10.2514/2.836>
- [36] B. Parent, M. N. Shneider, and S. O. Macheret, “Sheath governing equations in computational weakly-ionized plasmadynamics,” *Journal of Computational Physics*, vol. 232, no. 1, pp. 234–51, 2013. [Online]. Available: <http://dx.doi.org/10.1016/j.jcp.2012.08.011>
- [37] I. Adamovich and et al, “The 2017 plasma roadmap: Low temperature plasma science and technology,” *Journal of Physics D: Applied Physics*, vol. 50, no. 32, p. 323001, 2017.
- [38] H. Taghipour, Z. Amjad, M. A. Jafarabadi, A. Gholampour, and P. Nowrouz, “Determining heavy metals in spent compact fluorescent lamps (cfls) and their

- waste management challenges: Some strategies for improving current conditions,” *Waste Management*, vol. 34, no. 7, pp. 1251–1256, 2014. [Online]. Available: <http://www.sciencedirect.com/science/article/pii/S0956053X14001019>
- [39] N. Timofeev, G. Zissis, and D. Mikhaylov, “Glow discharge in the mixture of a rare gas and water vapour: Properties and application to light sources,” *Journal of Science and Technology in Lighting*, vol. 41, pp. 108–117, 2018.
- [40] G. J. M. Hagelaar and L.C.Pitchford, “Solving the boltzmann equation to obtain electron transport coefficients and rate coefficients for fluid models,” *Plasma Sources Science and Technology*, vol. 14, no. 4, p. 722, 2005.
- [41] J. van Dijk, G. M. W. Kroesen, and A. Bogaerts, “Plasma modelling and numerical simulation,” *Journal of Physics D: Applied Physics*, vol. 42, no. 19, p. 190301, 2009. [Online]. Available: <http://dx.doi.org/10.1088/0022-3727/42/19/190301>
- [42] J. P. Verboncoeur, “Particle simulation of plasmas: review and advances,” *Plasma Physics and Controlled Fusion*, vol. 47, no. 5A, pp. A231–A260, 2005. [Online]. Available: <http://dx.doi.org/10.1088/0741-3335/47/5A/017>
- [43] M. Surendra, D. B. Graves, and I. J. Morey, “Electron heating in lowpressure rf glow discharges,” *Applied Physics Letters*, vol. 56, no. 11, pp. 1022–1024, 1990. [Online]. Available: <https://doi.org/10.1063/1.102604>
- [44] W. N. G. Hitchon, T. J. Sommerer, and J. E. Lawler, “A self-consistent kinetic plasma model with rapid convergence,” *IEEE Transactions on Plasma Science*, vol. 19, no. 2, pp. 113–121, 1991.
- [45] T. E. Nitschke and D. B. Graves, “A comparison of particle in cell and fluid model simulations of lowpressure radio frequency discharges,” *Journal of Applied Physics*, vol. 76, no. 10, pp. 5646–5660, 1994. [Online]. Available: <https://doi.org/10.1063/1.358435>
- [46] P. Colella, M. R. Dorr, and D. D. Wake, “A conservative finite difference method for the numerical solution of plasma fluid equations,” *Journal of Computational Physics*, vol. 149, no. 1, pp. 168–193, 1999.
- [47] J. Poggie, I. Adamovich, N. Bisek, and M. Nishihara, “Numerical simulation of nanosecond-pulse electrical discharges,” *Plasma Sources Science and Technology*, vol. 22, no. 1, p. 015001, 2012. [Online]. Available: <http://dx.doi.org/10.1088/0963-0252/22/1/015001>
- [48] H. H. Choe and N. S. Yoon, “The effect of inertia terms in the momentum equation in fluid simulation of high density plasma discharge,” *Journal of the Korean Physical Society*, vol. 42, pp. S859–S866, 2003.
- [49] B. Scheiner, S. D. Baalrud, M. M. Hopkins, B. T. Yee, and E. V. Barnat, “Particle-in-cell study of the ion-to-electron sheath transition,” *Physics of Plasmas*, vol. 23, no. 8, p. 083510, 2016. [Online]. Available: <https://doi.org/10.1063/1.4960382>
- [50] A. Fiala, L. Pitchford, and J. Boeuf, “Two-dimensional, hybrid model of low-pressure glow discharges,” *Physical Review E*, vol. 49, no. 6, p. 5607, 1994.

- [51] M. J. Kushner, “Hybrid modelling of low temperature plasmas for fundamental investigations and equipment design,” *Journal of Physics D: Applied Physics*, vol. 42, no. 19, p. 194013, 2009. [Online]. Available: <http://dx.doi.org/10.1088/0022-3727/42/19/194013>
- [52] P. L. G. Ventzek, R. J. Hoekstra, and M. J. Kushner, “Two-dimensional modeling of high plasma density inductively coupled sources for materials processing,” in *Second High Density Plasma Workshop*, ser. J. Vac. Sci. Technol. B, Microelectron. Nanometer Struct. (USA), vol. 12, 3-4 Aug. 1993, Conference Proceedings, pp. 461–77. [Online]. Available: <http://dx.doi.org/10.1116/1.587101>
- [53] J. Poggie, “Dc glow discharges: A computational study for flow control applications,” in *36th AIAA Plasmadynamics and Lasers Conference, June 6, 2005 - June 9, 2005*, ser. 36th AIAA Plasmadynamics and Lasers Conference. American Institute of Aeronautics and Astronautics Inc., 2005, Conference Proceedings.
- [54] S. T. Surzhikov, *Computational Physics of Electric Discharges in Gas Flows*, ser. Physical Mechanics of Gas Discharges. Berlin: Berlin : De Gruyter, 2012.
- [55] E. E. Kunhardt and C. Wu, “Towards a more accurate flux corrected transport algorithm,” *Journal of Computational Physics*, vol. 68, no. 1, pp. 127–150, 1987.
- [56] D. L. Scharfetter and H. K. Gummel, “Large-signal analysis of a silicon read diode oscillator,” *IEEE Transactions on Electron Devices*, vol. ED-, no. 1, pp. 64–77, 1969. [Online]. Available: <http://dx.doi.org/10.1109/T-ED.1969.16566>
- [57] J. P. Boeuf, “A two-dimensional model of dc glow discharges,” *Journal of Applied Physics*, vol. 63, no. 5, pp. 1342–9, 1988. [Online]. Available: <http://dx.doi.org/10.1063/1.339961>
- [58] G. J. M. Hagelaar, F. J. de Hoog, and G. M. W. Kroesen, “Boundary conditions in fluid models of gas discharges,” *Phys. Rev. E*, vol. 62, pp. 1452–1454, Jul 2000. [Online]. Available: <https://link.aps.org/doi/10.1103/PhysRevE.62.1452>
- [59] S. T. Surzhikov and J. S. Shang, “Normal glow discharge with axial magnetic field in molecular hydrogen,” in *45th AIAA Plasmadynamics and Lasers Conference*, ser. 45th AIAA Plasmadynamics and Lasers Conference. American Institute of Aeronautics and Astronautics, Inc., 16-20 June 2014, Conference Proceedings, p. 18 pp.
- [60] A. V. Eletsii, *Transport Phenomena in Weakly Ionized Plasma: Handbook of Physical Quantities*, I. S. Grigoriev, E. Z. Meilikhov, and A. A. Radzig, Eds. Boca Raton: CRC Press, 1997.
- [61] D. A. Storozhev and S. T. Surzhikov, “Numerical simulation of glow discharge in a magnetic field through the solution of the boltzmann equation,” *Journal of Basic and Applied Physics*, vol. 2, no. 3, pp. 141–147, 2003. [Online]. Available: <https://academicpub.org/jbap/paperInfo.aspx?PaperID=5430>
- [62] E. Carbone, N. Sadeghi, E. Vos, S. Hubner, E. Veldhuizen, J. Dijk, S. Nijdam, and G. Kroesen, “Spatio temporal dynamics of a pulsed microwave argon plasma: ignition and afterglow,” *Plasma Sources Science and Technology*, vol. 24, no. 1, p. 015015, 2015. [Online]. Available: <http://stacks.iop.org/0963-0252/24/i=1/a=015015>

- [63] H. C. Kim, F. Iza, S. Yang, M. Radjenovic, and J. Lee, "Particle and fluid simulations of low-temperature plasma discharges: benchmarks and kinetic effects," *Journal of Physics D: Applied Physics*, vol. 38, no. 19, p. R283, 2005. [Online]. Available: <http://stacks.iop.org/0022-3727/38/i=19/a=R01>
- [64] G. G. Lister, "Low-pressure gas discharge modelling," *Journal of Physics D: Applied Physics*, vol. 25, no. 12, p. 1649, 1992. [Online]. Available: <http://stacks.iop.org/0022-3727/25/i=12/a=001>
- [65] "Trinitite database," [www.lxcat.net](http://www.lxcat.net), retrieved on August 10, 2018.
- [66] A. V. Eletskii, "Transport phenomena in weakly ionized plasma," in *Handbook of Physical Quantities*, I. S. Grigoriev, E. Z. Meilikhov, and A. A. Radzig, Eds. Boca Raton: CRC Press, 1997, ch. 20, pp. 539–548.
- [67] H. N. Kucukarpaci and J. Lucas, "Electron swarm parameters in argon and krypton," *Journal of Physics D: Applied Physics*, vol. 14, no. 11, p. 2001, 1981.
- [68] E. Wagner, F. Davis, and G. Hurst, "Time of flight investigations of electron transport in some atomic and molecular gases," *The Journal of Chemical Physics*, vol. 47, no. 9, pp. 3138–3147, 1967.
- [69] G. L. Braglia, "Motion of electrons and ions in a weakly ionized gas in a field. 1. foundations of the integral theory," *Beitrge aus der Plasmaphysik*, vol. 20, no. 3, pp. 147–194, 1980. [Online]. Available: <https://doi.org/10.1002/ctpp.19800200302>
- [70] M. M. Becker, D. Loffhagen, and W. Schmidt, "A stabilized finite element method for modeling of gas discharges," *Computer Physics Communications*, vol. 180, no. 8, pp. 1230–1241, 2009. [Online]. Available: <http://www.sciencedirect.com/science/article/pii/S0010465509000447>
- [71] M. Hayashi, *Electron collision cross sections Plasma Material Science Handbook*. Ohmsha Ltd.: Tokyo, 1992.
- [72] D. P. Lymberopoulos and D. J. Economou, "Fluid simulations of glow discharges: Effect of metastable atoms in argon," *Journal of Applied Physics*, vol. 73, no. 8, pp. 3668–3679, 1993.
- [73] "Hayashi database," [www.lxcat.net](http://www.lxcat.net), retrieved on August 10, 2018.
- [74] "Itikawa database," [www.lxcat.net](http://www.lxcat.net), retrieved on August 10, 2018.
- [75] "Morgan database," [www.lxcat.net](http://www.lxcat.net), retrieved on August 10, 2018.
- [76] T. Piskin, V. A. Podolsky, S. O. Macheret, and J. Poggie, "Challenges in numerical simulation of nanosecond-pulse discharges," *Journal of Physics D: Applied Physics*, vol. 52, no. 30, p. 304002, may 2019. [Online]. Available: <https://doi.org/10.1088%2F1361-6463%2F5230304002>
- [77] D. V. Roupasov, A. A. Nikipelov, M. M. Nudnova, and A. Y. Starikovskii, "Flow separation control by plasma actuator with nanosecond pulsed-periodic discharge," *AIAA Journal*, vol. 47, no. 1, pp. 168–185, 2009. [Online]. Available: <https://doi.org/10.2514/1.38113>

- [78] D. F. Opaitis, A. V. Likhanskii, G. Neretti, S. Zaidi, M. N. Shneider, R. B. Miles, and S. O. Macheret, "Experimental investigation of dielectric barrier discharge plasma actuators driven by repetitive high-voltage nanosecond pulses with dc or low frequency sinusoidal bias," *Journal of Applied Physics*, vol. 104, no. 4, p. 043304, 2008. [Online]. Available: <https://doi.org/10.1063/1.2968251>
- [79] D. Breden and L. Raja, "Simulations of nanosecond pulsed plasmas in supersonic flows for combustion applications," *AIAA Journal*, vol. 50, no. 3, pp. 647–658, 2012. [Online]. Available: <https://doi.org/10.2514/1.J051238>
- [80] A. M. Starik, N. Titova, L. Bezgin, and V. Kopchenov, "Initiation of diffusion combustion in a supersonic flow of h<sub>2</sub>-air mixture by electrical discharge excited oxygen molecules," *Journal of Physics D: Applied Physics*, vol. 41, no. 12, pp. 125–210, 2008. [Online]. Available: <http://stacks.iop.org/0022-3727/41/i=12/a=125210>
- [81] S. O. Macheret, M. N. Shneider, and R. B. Miles, "Modeling of air plasma generation by repetitive high-voltage nanosecond pulses," *IEEE Transactions on Plasma Science*, vol. 30, no. 3, pp. 1301–1314, 2002.
- [82] S. O. Macheret, M. N. Shneider, and R. C. Murray, "Ionization in strong electric fields and dynamics of nanosecond-pulse plasmas," *Physics of Plasmas*, vol. 13, no. 023502, 2006.
- [83] V. Podolsky, A. Khomenko, and S. Macheret, "Time-resolved measurements of electron number density in argon and nitrogen plasmas sustained by high-voltage, high repetition rate, nanosecond pulses," *Plasma Sources Science and Technology*, vol. 27, no. 10, 2018. [Online]. Available: <https://doi.org/10.1088/1361-6595/aae35e>
- [84] H. Bhringer, M. DurupFerguson, and D. W. Fahey, "Mobilities of various mass-identified positive ions in helium, neon, and argon," *The Journal of Chemical Physics*, vol. 79, no. 4, pp. 1974–1976, 1983.
- [85] K. B. McAfee, D. Sipler, and D. Edelson, "Mobilities and reactions of ions in argon," *Physical Review*, vol. 160, no. 1, pp. 130–135, 1967.
- [86] H. W. Ellis, R. Pai, E. W. McDaniel, E. A. Mason, and L. A. Viehland, "Transport properties of gaseous ions over a wide energy range," *Atomic Data and Nuclear Data Tables*, vol. 17, pp. 177–210, 1976.
- [87] R. W. Engstrom and W. S. Huxford, "Time-lag analysis of the townsend discharge in argon with activated caesium electrodes," *Physical Review*, vol. 58, no. 1, pp. 67–77, 1940.
- [88] Y. J. Shiu and M. A. Biondi, "Dissociative recombination in argon: Dependence of the total rate coefficient and excited-state production on electron temperature," *Phys. Rev. A*, vol. 17, pp. 868–872, 1978.
- [89] F. J. Mehr and M. A. Biondi, "Electron-temperature dependence of electron-ion recombination in argon," *Phys. Rev.*, vol. 176, pp. 322–326, 1968.
- [90] D. J. Emmons and D. E. Weeks, "Kinetics of high pressure argon-helium pulsed gas discharge," *Journal of Applied Physics*, vol. 121, no. 20, p. 203301, 2017.

- [91] B. Lay, R. Moss, S. Rauf, and M. Kushner, "Breakdown processes in metal halide lamps," *Plasma Sources Science and Technology*, vol. 12, no. 1, p. 8, 2003.
- [92] A. Tavant and M. A. Lieberman, "Hybrid global model of water cluster ions in atmospheric pressure ar/h<sub>2</sub>o rf capacitive discharges," *Journal of Physics D: Applied Physics*, vol. 49, no. 46, p. 465201, 2016.
- [93] H. Yuchen, S. Uehara, H. Takana, and N. Hideya, "Numerical modelling and simulation of chemical reactions in a nano-pulse discharged bubble for water treatment," *Plasma Science and Technology*, vol. 18, no. 9, p. 924, 2016.
- [94] S. Tatsuru and M. Tomoyuki, "Contribution of electrons, ar(3p<sub>0,2</sub>), h<sub>2</sub>o+, and h<sub>3</sub>o+ to production of oh(a<sub>2</sub>Σ<sup>+</sup>) in a micro-dielectric barrier discharge of ar/h<sub>2</sub>o," *Japanese Journal of Applied Physics*, vol. 54, no. 1S, p. 01AC03, 2015.
- [95] W. Lindinger, "Reaction-rate constants in steady-state hollow-cathode discharges: Ar+ h<sub>2</sub>o reactions," *Physical Review A*, vol. 7, no. 1, pp. 328–333, 1973.
- [96] T. Shirafuji and T. Murakami, "Contribution of electrons, Ar(<sup>3</sup>P<sub>0,2</sub>), H<sub>2</sub>O<sup>+</sup>, and H<sub>3</sub>O<sup>+</sup> to production of OH(A<sup>2</sup>Σ<sup>+</sup>) in a micro-dielectric barrier discharge of Ar/H<sub>2</sub>O," *Japanese Journal of Applied Physics*, vol. 54, no. 1S, 2015.
- [97] U. Kortshagen, C. Busch, and L. Tsendin, "On simplifying approaches to the solution of the boltzmann equation in spatially inhomogeneous plasmas," *Plasma Sources Science and Technology*, vol. 5, no. 1, p. 1, 1996. [Online]. Available: <http://stacks.iop.org/0963-0252/5/i=1/a=001>
- [98] G. K. Grubert, M. M. Becker, and D. Loffhagen, "Why the local-mean-energy approximation should be used in hydrodynamic plasma descriptions instead of the local-field approximation," *Phys. Rev. E*, vol. 80, p. 036405, Sep 2009. [Online]. Available: <https://link.aps.org/doi/10.1103/PhysRevE.80.036405>
- [99] M. A. Lieberman and L. A. J., *Principles of plasma discharges and materials processing*, 2nd ed. Hoboken, N.J.: Hoboken, N.J. : Wiley-Interscience, 2005.
- [100] J. Behnke, Y. B. Golubovsky, S. U. Nisimov, and I. A. Porokhova, "Selfconsistent model of a positive column in an inert gas discharge at low pressures and small currents," *Contributions to Plasma Physics*, vol. 36, no. 1, pp. 75–91, 1996. [Online]. Available: <https://doi.org/10.1002/ctpp.2150360105>
- [101] "Bsr database," [www.lxcat.net](http://www.lxcat.net), retrieved on August 10, 2018.
- [102] "Reference Database Number 69, Eds. P.J. Linstrom and W.G. Mallard, National Institute of Standards and Technology, Gaithersburg MD, 20899," <https://doi.org/10.18434/T4D30>, retrieved February 19, 2019.
- [103] G. Bouchoux, A. M. Rashad, and A. I. Helal, "Theoretical investigation of selenium interferences in inductively coupled plasma mass spectrometry," *The Journal of Physical Chemistry A*, vol. 116, no. 36, pp. 9058–9070, 2012. [Online]. Available: <https://doi.org/10.1021/jp304644u>
- [104] G. M. Petrov and C. M. Ferreira, "Numerical modelling of ar glow discharge at intermediate and high pressures," *Int. Rep. CFP*, vol. 10-97, 2013.

- [105] E. Goos, A. Burcat, and B. Ruscic, “Extended third millenium ideal gas and condensed phase thermochemical database for combustion (with update from active thermochemical tables).” *Report ANL 05/20 and TAE 960 Technion-IIT, Aerospace Engineering, and Argonne National Laboratory, Chemistry Division*, 7 2005.
- [106] C. Yuan, E. A. Bogdanov, S. I. Eliseev, and A. A. Kudryavtsev, “1d kinetic simulations of a short glow discharge in helium,” *Physics of Plasmas*, vol. 24, no. 7, p. 073507, 2017. [Online]. Available: <https://doi.org/10.1063/1.4990030>
- [107] J. T. Gudmundsson and E. G. Thorsteinsson, “Oxygen discharges diluted with argon: dissociation processes,” *Plasma Sources Science and Technology*, vol. 16, no. 2, p. 399, 2007.
- [108] R. Liu, Y. Liu, W. Jia, and Y. Zhou, “A comparative study on continuous and pulsed rf argon capacitive glow discharges at low pressure by fluid modeling,” *Physics of Plasmas*, vol. 24, no. 1, p. 013517, 2017.
- [109] F. Kannari, M. Obara, and T. Fujioka, “An advanced kinetic model of electronbeamexcited krf lasers including the vibrational relaxation in  $\text{krf}^*(b)$  and collisional mixing of  $\text{krf}^*(b,c)$ ,” *Journal of Applied Physics*, vol. 57, no. 9, pp. 4309–4322, 1985.
- [110] M. J. McCaughey and M. J. Kushner, “A model for particulate contaminated glow discharges,” *Journal of Applied Physics*, vol. 69, no. 10, pp. 6952–6961, 1991.
- [111] S. Ashida, C. Lee, and M. A. Lieberman, “Spatially averaged (global) model of time modulated high density argon plasmas,” *Journal of Vacuum Science & Technology A*, vol. 13, no. 5, pp. 2498–2507, 1995.
- [112] J. W. Shon, “Modeling high pressure rare gas lasers: Kinetics and plasma chemistry,” Ph.D. dissertation, University of Illinois at Urbana Champaign, 1994.

## APPENDICES

## A. COEFFICIENTS AND CONSTANTS FOR THE SIMULATIONS

The constants for the transport coefficients are given here for various gases. It should be noted that the secondary ionization coefficients are sometimes chosen as  $\gamma = 0.33$  to speed convergence. [59].

Table A.1.

Townsend, recombination rate, and the secondary emission coefficient for different simulations with specified case numbers.

#	Gas	$\alpha$ [ $m^{-1}$ ]		$\beta$ [ $m^3/s$ ]	$\gamma$	Ref.
		A [ $m^{-1}Torr^{-1}$ ]	B [ $V/(m.Torr)$ ]			
C1	$N_2$	1200	34200	$2.0 \times 10^{-13}$	0.33	[6]
C2	$H_2$	500	13000	$2.0 \times 10^{-13}$	0.33-0.01	[6]
C3	$He$	300	34000	$2.0 \times 10^{-13}$	0.33	[6]

Table A.2.

Transport —mobility,  $\mu$  and diffusion,  $D$ — coefficients for ions and electrons in different gases for various simulations. ER means Einstein Relation.

#	Gas	$\mu_s/P$ ( $Torr$ ) [ $m^2/V.s$ ]		$D_s$ [ $m^2/s$ ]		Ref.
		$\mu_{ion}/P$	$\mu_e/P$	$D_{ion}$	$D_e$	
C1	$N_2$	$0.145/P$	$44/P$	ER	ER	[6]
C2	$H_2$	$0.655/P$	$37/P$	ER	ER	[6]
C3	$He$	$0.83/P$	$86/P$	ER	ER	[6, 106]

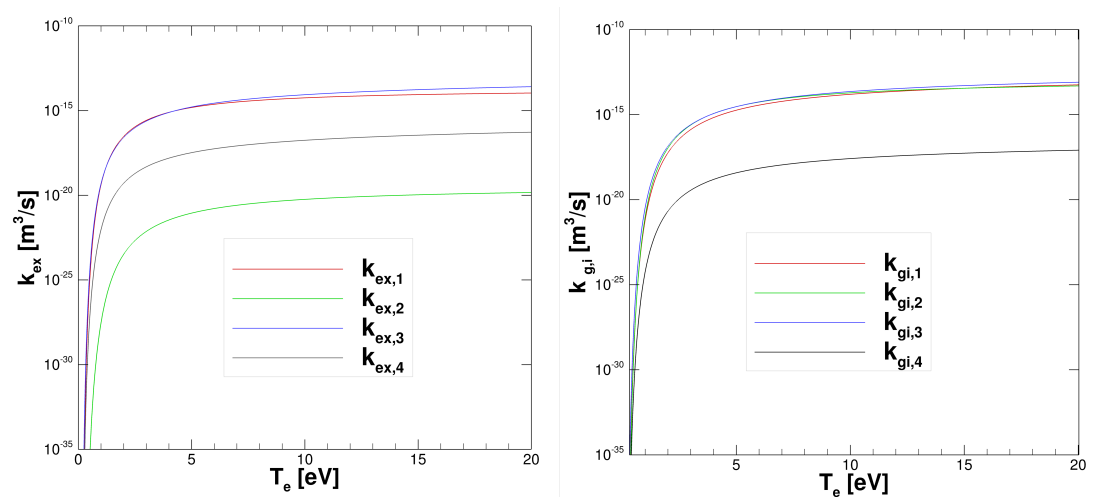
## B. DISCUSSION ABOUT REACTION RATES

Here, the discussion about the reaction rates is expanded. A set of different reaction rates [ $m^3/s$ ] for the same reactions from different sources is listed below:

Table B.1.  
Examples of Different Reaction Rates for the Same Processes.

Reaction	Label	Rates	Reference
$e + Ar \rightarrow Ar^* + e$	$k_{ex,1}$	$2.1 \times 10^{-14} e^{(-13.13/T_e)}$	[92, 107]
	$k_{ex,2}$	$3.712 \times 10^{-14} e^{(-18.687/T_e)}$	[108]
	$k_{ex,3}$	$5.0 \times 10^{-15} T_e^{0.74} e^{(-11.56/T_e)}$	[109–111]
	$k_{ex,4}$	$1.0 \times 10^{-17} T_e^{0.75} e^{(-11.6/T_e)}$	[112]
$e + Ar \rightarrow Ar^+ + 2e$	$k_{gi,1}$	$2.3 \times 10^{-14} T_e^{0.59} e^{(-17.44/T_e)}$	[92, 107]
	$k_{gi,2}$	$1.235 \times 10^{-13} e^{(-18.687/T_e)}$	[108]
	$k_{gi,3}$	$2.3 \times 10^{-14} T_e^{0.68} e^{(-15.76/T_e)}$	[109–111]
	$k_{gi,4}$	$4.0 \times 10^{-18} T_e^{0.5} e^{(-15.8/T_e)}$	[112]
$e + Ar^* \rightarrow Ar^+ + 2e$	$k_{si,1}$	$1.8 \times 10^{-13} T_e^{0.61} e^{-2.61/T_e}$	[92, 107]
	$k_{si,2}$	$2.05 \times 10^{-13} e^{(-4.95/T_e)}$	[108]
	$k_{si,3}$	$6.80 \times 10^{-15} T_e^{0.67} e^{(-4.20/T_e)}$	[109, 111]
	$k_{si,4}$	$1.0 \times 10^{-16} T_e^3 e^{(-4.16/T_e)}$	[112]
$e + Ar^* \rightarrow Ar + e$	$k_{dx,1}$	$5.83 \times 10^{-16}$	[92]
	$k_{dx,2}$	$3.90 \times 10^{-16} T_e^{0.71}$	[107]
	$k_{dx,3}$	$1.818 \times 10^{-15} e^{(-2.14/T_e)}$	[108]
	$k_{dx,4}$	$4.3 \times 10^{-16} T_e^{0.74}$	[111]
	$k_{dx,5}$	$1.0 \times 10^{-17} T_e^{0.75}$	[112]

The species,  $\text{Ar}^*$  is chosen to represent excited levels of argon lumped together in one level. A representative value for  $\text{Ar}^*$  is chosen as  $4s$  metastable state with the energy of  $\varepsilon = 11.56$  eV. The data gathered from other studies in Table B.1 is based on the same metastable level. The comparisons of the reaction rates listed in Table B.1 are given in Figs. B.1 & B.2.

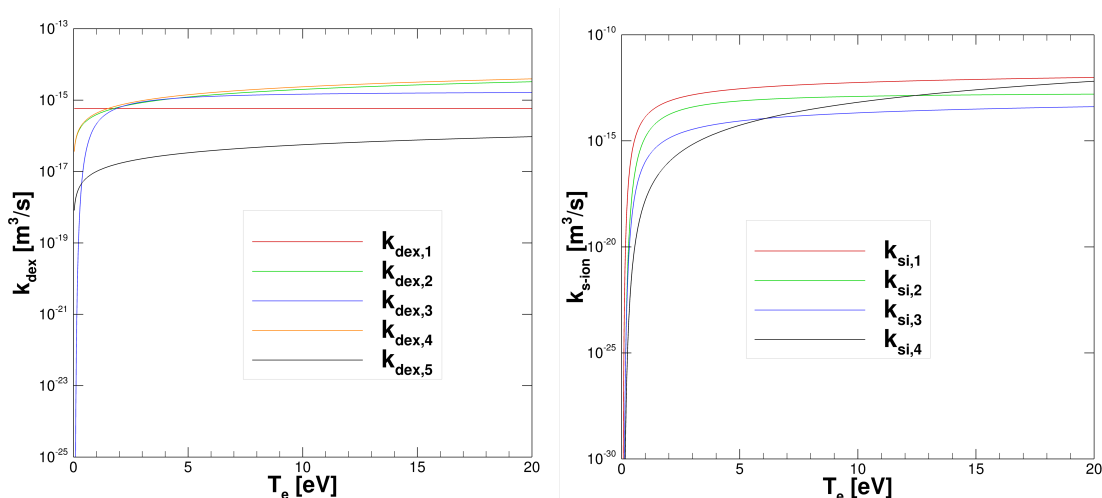


(a) Excitation reaction.

(b) Ground ionization reaction.

Fig. B.1. Comparisons of the different reaction rates from various studies for the excitation and ionization of argon from the ground level.

The black line represents the rates which used in this study. The discrepancies in the reaction rates are a couple of orders of magnitude. The most severe differences are in the excitation reactions, Fig. B.1. Since the reaction rates are a function of the collision cross section, it is expected that these rates are based on different cross sections. Also, a common practice is to tune reactions rates for the purposes of discharge simulations in a particular regimes. Such kinetic mechanisms have limited validity outside of the tuned regime. Figs. B.1 & B.2 show the rates with respect to electron temperature, and the distributions are assumed Maxwellian for the calculation of each of these rates.



(a) De-excitation reaction.

(b) Step-wise ionization reaction.

Fig. B.2. Comparisons of the different reaction rates from various studies for the de-excitation and step wise ionization of argon from the excited level.

As mentioned earlier, to obtain the swarm parameters for electrons from Bol-sig+, cross sections for different processes are gathered from the LxCat website ([www.lxcatt.net](http://www.lxcatt.net)). The discussion on the usage of different databases for argon-water mixture is resented here. For an argon-water mixture, there are additional reactions to excitation, ionization and recombination reactions of Argon, such as attachment reactions, rotational and vibrational reactions, and dissociative reactions. It can be seen from Fig. B.3 that the mean electron energy profiles change a little bit, especially in the lower E/N range. The reason of those small alterations is the inclusion of different kinds of reactions. Although the Morgan and Hayashi databases [65, 73] do not include any rotational level excitations, Itikawa and Trinita [65, 74] include different numbers of rotational and vibrational level excitations.

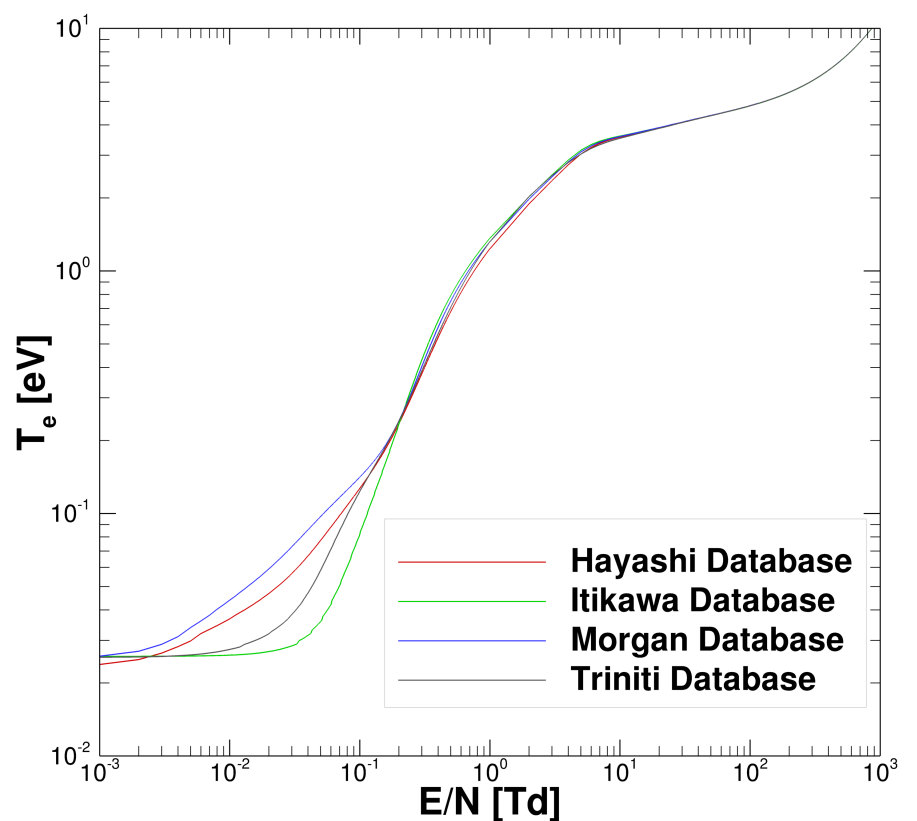


Fig. B.3. Mean electron temperature variation with respect to reduced electric fields from different databases: Trinitite [65], Hayashi [73], Itikawa [74], Morgan [75] for *Argon + 0.1% H<sub>2</sub>O* mixture

VITA

## VITA

**EDUCATION**

---

- Purdue University** Aug. 2015 - December 2019  
 School of Aeronautics and Astronautics  
 PhD in Aerodynamics  
 Dissertation: Numerical Simulations of Gas Discharges for  
 Flow Control Applications
- Middle East Technical University** Sep. 2012 - July 2015  
 Aerospace Engineering  
 MS in Aerodynamics  
 Thesis: Analysis of Weakly Ionized Hypersonic Flows
- Middle East Technical University** Sep. 2008 - Dec. 2011  
 Faculty of Art and Science  
 BS in Physics  
 Major in Solid State Physics and Test & Measurements

**RESEARCH INTERESTS**

---

Plasma Physics, Computational Fluid Dynamics, Aerodynamics, Plasma Chemistry, Hypersonic Flow, Parallel Computing, Aerothermodynamics, Solid State Physics, Test and Measurement, Semiconductors

**COMPUTER SKILLS**

- **Operating Systems:** UNIX/ LINUX, WINDOWS
- **Programming:** FORTRAN, C/C++, MPI, CATIA, LABVIEW, ORIGIN, MICROSOFT OFFICE, POINTWISE, TECPLOT, MATHCAD, COMSOL, LATEX, PIC, MATLAB, HTML